Waveguide-Integrated Light-Emitting Carbon Nanotubes as Classical and Non-Classical Light Source

Zur Erlangung des akademischen Grades eines

DOKTORS DER NATURWISSENSCHAFTEN

durch die Fakultät für Physik

des Karlsruher Instituts für Technologie (KIT)

genehmigte

DISSERTATION

von

M.-Phys. Svetlana Khasminskaya

aus Kazan, Russland

Tag der mündlichen Prüfung: 08.07.2016
Referent: Prof. Dr. Martin Wegener
Korreferent: Prof. Dr. Wolfram Pernice

List of publications

1. S. Khasminskaya*, F. Pyatkov*, B. S. Flavel, W. H. P. Pernice and R. Krupke. Waveguide-Integrated Light-Emitting Carbon Nanotubes. *Adv. Mater.* **26**, 3465-3472 (2014).

2. F. Pyatkov*, S. Khasminskaya*, V. Kovalyuk, F. Hennrich, M. M. Kappes, G. Gol'tsman, W. H. P. Pernice and R. Krupke. Sub-nanosecond light pulse generation with waveguide-coupled carbon nanotube transducers. (2016). *Beilstein J. Nanotechnol.* **8**, 38-44 (2017).

3. S. Khasminskaya*, F. Pyatkov*, K. Słowik, S. Ferrari, O. Kahl, V. Kovalyuk, P. Rath, A. Vetter, F. Hennrich, M. M. Kappes, G. Gol'tsman, A. Korneev, C. Rockstuhl, R. Krupke, and W. H. Pernice. Fully integrated quantum photonic circuit with an electrically driven light source. *Nat. Photon.* **10**, 727–732 (2016).

4. F. Pyatkov*, V. Fütterling*, S. Khasminskaya, B. S. Flavel, F. Hennrich, M. M. Kappes, R. Krupke, and W. H. P. Pernice. Cavity-enhanced light emission from electrically driven carbon nanotubes. *Nat. Photon.* **10**, 420-427 (2016).

5. R. Fechner*, F. Pyatkov*, S. Khasminskaya, B. S. Flavel, R. Krupke, and W. H. P. Pernice. Directional coupler with integrated carbon nanotube incandescent light emitters. *Opt. Express* **24,** 966-974 (2016).

*These authors contributed equally to the work.

Contents

Nomenclature

Abbreviations

AC   Alternating current

Au   Gold

C   Carbon

Cr   Chromium

CMC   CoMoCat

CVD   Chemical vapor deposition

DOS   Density of states

DC   Direct current

EBL   Electron beam lithography

EL   Electroluminescence

EEA   Exciton-exciton annihilation

FFT   Fast Fourier transform

FET   Field-effect transistor

HiPco High-pressure carbon dioxide

HSQ   Hydrogen silsesquioxane

IPA   Isopropanol

LNA   Low noise amplifier

MIBK Methyl-isobutyl keton

NPIC   Nanophotonic integrated circuit

NIR   Near-infrared

NbN   Niobium nitride

NV   Nitrogen vacancies

PL   Photoluminescence

PCNBC Photonic crystal nanobeam cavity

PVD   Physical vapor deposition

PMMA   Polymethylmethacrylat

QC   Quantum computer

QED   Quantum electrodynamics

RF   Radio frequency

RIE   Reative ion etching

SEM   Scanning electron microscope

Sc-SWCNT Semiconducting single-walled carbon nanotube

Si_3N_4 Silicon nitride

SiV   Silicon vacancies

SiO_2 Silicon dioxide

Si   Silicon

SPAD   Single-photon avalanche diode

SPS   Single-photon source

SWCNT Single-walled carbon nanotube

SNSPD Superconducting nanowire single-photon detector

SPD   Single-photon detector

1 Introduction

For the last four decades, the development of computing hardware precisely followed Moore's law, which predicts a doubling of the components in integrated circuits every two years. However, the end of this tendency due to physical restraints is foreseeable. The transistor density in integrated circuits will soon reach its limits, accompanied with excessively increasing energy consumption. At the same time, the demand for high-bandwidth data transfer (for example high-resolution video streaming) is growing continuously. Therefore, new technologies for fast and efficient information processing have to be developed and practically realized. Quantum computing, based on the laws of quantum mechanics, promises to extend computational capability far beyond that of classical computers and to significantly reduce the energy consumption and shortage of resources [1]. It allows for parallel computation of some task due to superposition of quantum mechanical states, which have to be precisely controlled and manipulated. The field of photonic quantum technologies opens up opportunities for many emerging applications, such as quantum computation, quantum cryptography and in particular quantum key distribution (QKD), and quantum metrology. Although so far a *universal* quantum computer (QC) remained unreachable, there are many successful demonstrations of reduced quantum computers, which perform certain computational tasks with unprecedented high efficiency. One recent representative example of quantum simulators is the determination of binding energies of molecular compounds and a ground-state energy with a precision unreachable for classical computers [2,3]. A quantum bit of information is called qubit. The most attractive platform for the realization of a quantum computer is optics with a single photon as a qubit. The advantages of a photon as information carrier are that it can travel at the speed of light over long distances, weakly interacting with its environment and decohering slowly [4]. In case of *optical* QC, the information can be encoded, for example, with the photon's polarization. However, the main challenge in this approach is to realize an entangling logic gate as the basic element for quantum computing. [1]

A breakthrough was made in 2001 by demonstrating that a quantum computer can be build only with *linear* optical elements (such as beam splitters and phase shifters) along with single-photon light emitters and detectors. [5] The latter have to be scalable and compatible with linear optics. Therefore, to realize such a linear optical quantum computer (LOQC), systems containing non-classical sources which produce single photons *on demand*, low-loss optical components, and efficient detectors are highly searched for. After two decades of intensive theoretical and experimental efforts, numerous practical applications were realized. A prominent example of a linear optical quantum system is boson sampling, which exploits a quantum superposition [6,7]. At the beginning of practical realization of quantum computation, experiments were carried out with single-photon sources based on atoms and ions in a trap, cooled almost to the ground state. However, solid emitters are a more preferable choice than gas-phase sources. One of the most widely used technique is the generation of "heralded"

photon pairs, i.e. by spontaneous parametric down-conversion in a non-linear medium [8]. However, these are examples of macroscopic, external sources, which need alignment and coupling to the other optical elements in the system.

A key requirement for "real" applications is the scalable realization of quantum photonic systems, which contain single-photon sources, detectors, and linear optical elements. Due to growing complexity of the quantum experiments, systems built on an optical bench and containing large numbers of elements experience challenges with alignment and stability. To solve this problem reliable nanoscale sources and detectors have to be scalably integrated on a common platform.

1.1 Integrated circuits and single-photon sources

Technological applications require scalable low-cost realization of each single component. One possibility for such system are nanophotonic integrated circuits (NPICs), which provide a rich toolbox for the investigation of on-chip optical phenomena [9]. Ideally, single-photon sources, detectors, and optical elements have to be realized monolithically from the same material and on the single chip. This is important to reduce the fabrication costs and to avoid optical losses. Tremendous breakthrough has been made in the development of scalable fabrication of each component individually. Prominent example is diamond photonic circuits with optically-excited single-color center in diamond. However, integration of all three components in one-material circuit had not been achieved so far. The solution to this problem was found in *hybrid* integrated photonic circuits. This field gained great interest, and much effort was put into improving both *hybrid* single-photon sources and detectors. The scalable integration of hybrid detectors for non-classical light has already been solved, for example through traveling-wave superconducting nanowire single-photon detectors (SNSPD) [10]. However, scalable and reproducible on-chip quantum sources are highly searched after. Hence, the combination of these components into common fully-integrated quantum circuits remains challenging [11].

Besides of having nanoscale foot-prints, an ideal integrated single-photon source has to be bright, fast, and subsequently produce *indistinguishable* single photons on demand. Such an ideal source exhibits perfect *antibunching*, respectively a low probability of multi-photon emission compared to single-photon emission. Hence, simultaneous emission of more than one photon is strongly suppressed. For demands of practical realization, a scalable and dense integration on chip, as well as room temperature operation has to be possible. A real single-photon emitter, however, typically demonstrates only a few of the aforementioned characteristics. Usually, sources with only two parameters, most important for the particular application, are developed. For example, high brightness and negligible probability of multi-photon emission, or room-temperature operation and a high degree of indistinguishability.

Among condensed matter single emitters, organic molecules [12,13,14], single-color centers in diamond [15,16,17,18] (nitrogen and silicon vacancies), as well as semiconductor nanocrystals and heterostructures (for example, InGaAs) [19,20,21,22] have been studied intensively for single-photon generation. Nitrogen vacancies (NV) and silicon vacancies (SiV) in diamond are promising long-lived room temperature single-photon emitters. Antibunching was demon-

strated to be close to 0 for NV, and smaller than 0.5 for SiV. Owing to the excellent spectral stability and ultra-narrow line width of SiV, this source is suitable for generation of indistinguishable coherent photons [23]. On the other hand, the NV emitters at room temperature are inhomogeneous due to variations in the local strain, affecting the energy levels. Therefore, they does not generate coherent photons. Further promising single emitters are organic molecules. They show prominent antibunching especially at cryogenic temperatures, and therefore were the first investigated single-photon source [24]. The radiation decay time is almost lifetime-limited, which manifests them as a perfect emitter of indistinguishable photons (if measured only at the spectrally-filtered zero-phonon line). However, single molecules experience photobleaching, especially at ambient conditions, which reduces their operating time. To avoid this, the single molecules have to be included in an environment protecting them from reactive oxygen. Quantum dots are easily scalable, bright, narrow-band, and stable emitters which demonstrate negligible multi-photon probability. Owing to a small band gap, this emitter need to be operated at cryogenic temperatures. Most recently however, efficient single-photon emission from an antenna-enhanced quantum dot was demonstrated also at room-temperature [25] Although these three classes gained most of the attraction, other materials, such as semiconducting nanowires or monolayers, can be implemented as well. For example, an alternative single-photon emitter made from a 2D monolayer of transition metal dichalcogenides (in particular WSe_2) was demonstrated, exhibiting excellent spectral stability [26].

Although optical pumping was mostly used for excitation of the sources, electrical excitation was also demonstrated in some cases. Electrically-driven non-classical emission arises as result of radiative recombination of electrons and holes in deep localization traps. For example, a NV-based source was realized by scalable fabrication of p-i-n diamond diodes with bottom-top geometry. [18] An electroluminescence antibunching degree of 0.45 was measured at room temperature with neutral NV centers. Organic molecules embedded in a solid-state matrix were implemented into an OLED architecture and excited electrically. [14] Upon electrical excitation, non-classical lightwith a lifetime of about $1\,\mu m$, which is close to the intrinsic one, was shown at room temperature. The authors suggested an integration into photonic circuits, which has not been realized yet. Also, some improvements have to be made considering the relatively low count rates (in the kHz range), blinking, and high emission background, elevating the antibunching level. Recently, quantum dots [27] and single-defect center in silicon carbide [11] (SiC) were used as electrically-driven quantum source. The latter shows a prominent antibunching degree of 0.2 (without background correction) and relatively high and stable count rates. The emission count rate of all electrically-driven sources can be easily increased by increasing the injected current. Also, at higher excitation power saturation of emission is observed.

A combination of an on-chip single-photon source and optical waveguide was also realized by coupling the single-photon emitter to a photonic crystal waveguide [21,22]. Emission enhancement and optical filtering was achieved by this implementation.

Various different approaches for single-photon emitters that can be hybridly realized on a chip were discussed above. Some of the presented sources are triggered electrically, others have been integrated into photonic circuits. However, *electrically-driven and at the same time waveguide-integrated single-photon sources* have not been realized yet. Therefore, the large-

scale implementation of reproducible, bright, waveguide-compatible single-photon emitter remains illusive.

A major challenge is that most common single-photon sources are not identical and require preselection and characterization. This is performed according to their spectral characteristic and photon statistics, i.e. their degree of antibunching. They either have to be transferred onto the chip after preparation and selection [28] or the photonic circuits have to be realized in a precise alignment to the chosen sources with appropriate characteristics [29]. The first hybrid approach, combining a nanowire light source and a photonic-crystal waveguide was demonstrated by Park et al. [29]. Optical and electrical excitation of classical light were shown. Another reason is that the majority of single-photon sources are excited optically. For single-photon detection, optical filtering of the remaining pump light with much higher intensity than the emission itself is necessary [30]. This filtering is often sophisticated, because the filters with high fidelity and spectrally-aligned profile has to be provided. In order to realize a fully-integrated photonic circuit, such filers have to be co-integrated on-chip (for example, a photonic crystal cavity). Also, filtering leads to additional losses in the single-photon emission and to degradation of the photon statistics. Therefore, identical sources, whose emission is controlled purely electrically, are required for practical applications of integrated photonic circuits [29]. The great advantage of electrically-driven sources is that they can be easily scaled-up and allow for unlimited on-chip design. Another necessary term is the efficient coupling to integrated optical waveguides. While optically-driven sources are widely used, there is a lack of electrically-driven sources with small footprints, potentially compatible with integrated photonic circuits framework. A non-classical source with above mentioned characteristics is a crucial element for on-chip quantum optical applications. Remarkable progress has been made in both directions (electrical excitation and waveguide integration) separately. However such single-photon sources have not been presented so far. Therefore, our work contains the first demonstration of such system.

1.2 Semiconducting carbon nanotubes as photon source

To overcome the challenges outlined above, we employed carbon nanotubes, which have emerged as a promising nanoscale active element for the realization of a broad spectrum of optoelectronic devices [31]. Prominent examples are carbon-based light-emitting diodes [32], ultra narrow-band emitters coupled to a photonic crystal nanobeam cavity [33], ultra-fast thermal emitters [34] or cavity-controlled detectors. These devices can be employed for on-chip information processing and high bandwidth on-chip communication. [35] A single-walled carbon nanotube (SWCNT) is an excellent material regarding its properties. It possess high thermal and electrical conductivity, its density of states redistributed into distinct bands as result of reduced dimensionality. Semiconducting SWCNTs are efficient and bright light emitters with a direct optical band gap of about $1\,\mathrm{eV}$. This allows single semiconducting SWCNTs to exhibit a narrow-band luminescence upon optical or electrical excitation [36,37,38]. The central wavelength of the emission line is in the near-infrared (NIR) or visible spectral range [39]. Its exact position depends on the chirality and diameter of the single nanotube as well as on the surrounding environment [40]. The latter along with the temperature affects

also the emission bandwidth. For a suspended nanotube at cryogenic conditions, the emission bandwitdth is ultra-narrow (resolution-limited). Due to the continuous progress in sorting of carbon nanotubes [41,42], suspensions containing purely semiconducting species of only one or few chiralities can be prepared. Therefore, the spectral properties of the emitter can be tuned by implementing single semiconducting SWCNTs with a particular structure. Due to the aforementioned properties, single semiconducting SWCNTs are an excellent choice as telecom-band emitters at room-temperature. Moreover, SWCNTs are only one nanometer in diameter, while typical lengths of around one micrometer can be prepared. Carbon nanotubes can be deposited site-selectively [43] on a chip by dielectrophoretic forces out of pre-sorted suspensions. This approach allows for the scalable fabrication of the SWCNT-based sources. High coupling efficiency to the waveguided mode can be established, owing to the perpendicular orientation of the SWCNT to the waveguide, and because emission from the one-dimensional SWCNT-source is polarized along the nanotube's axis. Therefore, SWCNTs are promising candidates for nanoscale photon emitters embedded into integrated photonic circuits.

Recently, generation of non-classical light upon *optical* excitation of a single semiconducting carbon nanotube was demonstrated at cryogenic condition [44,45] and later at room temperature [46,47]. The antibunching depth of < 0.3 reveals a reduced probability for multi-photon emission. Ultra-narrow, bright, and long-time stable emission was shown for a semiconducting SWCNT suspended over a trench. [45] The non-classical light originates from exciton recombination in naturally-induced local trap sites. However, the energy potential of these traps is not sufficiently deep to localize excitons at room temperature due to high thermal energy. To solve this problem, artificially-induced deep traps were suggested [46], which efficiently localize the excitons and support single-photon emission at ambient conditions. In this thesis we demonstrate for the first time *electrically-generated* non-classical light from SWCNTs, evanescently coupled to an underlying waveguide. Furthermore, we intended to realize the integration of the source in a series of common optical elements on-chip. Therefore, the scope of this work is important from the side of fundamental science, since the non-classical light from electrically-triggered SWCNT has not been demonstrated before. From the technological side, the realization of an electrically-driven single-photon source integrated in a waveguide along with single-photon detectors constitutes a crucial step towards on-chip quantum information processing.

Additional to electroluminescence, electrically-driven carbon nanotube emit thermal light owing to Joule heating of the nanowire. Waveguide-integrated SWCNT-based thermal light sources show potential as nanoscale broadband opto-electronic devices.

1.3 Structure of this work

The scope of this work was to analyze carbon nanotube-based devices as nanoscale classical sources for on-chip classical communication, as well as single-photon sources for quantum photonics applications.

In the second chapter the fundamentals, such as photon statistics and second-order correlation, are briefly discussed. Then, various on-chip single-photon sources, realized in the past

decades, and their characteristics are compared. In the second part, a semiconducting carbon nanotube as an alternative single-photon emitter is presented. Its electronic structure and optical properties are introduced. The mechanism of photoluminescence, as well as exciton localization in a 1D nanowire are described in detail, and electroluminescence is shortly touched.

The third chapter introduces the device layout and fabrication steps, based on silicon-based techniques. The sorting of carbon nanotubes, which is of great importance for the preparation of suspensions with purely semiconducting species and only few chiralities, is described. Lastly, a scalable deposition method of SWCNTs (AC-dielectrophoresis from suspensions) is shortly introduced.

In the fourth chapter the coupling of light generated by SWCNT-based sources into the waveguide is shown. The realization of several hybrid photonic devices is proposed, such as prolongated waveguides, interferometers, directional couplers and photonic beam cavities. These devices are the basis for linear optical quantum computers. Emission from waveguide-coupled devices is analyzed in fiber-coupled as well as optical microscope-based free-space setups, and the results of the measurements are compared. Broadband operation of the light-emitting SWCNTs is proposed for ultra-fast nanoscale electro-optical transducers. High thermal conductance along the nanotube's axis allows for fast modulation of the emission, which can be applied for high-speed on-chip data transfer.

In the fifth chapter non-classical light generation from electrically-driven waveguide-coupled SWCNTs is demonstrated for the first time. The co-integration of the SWCNT-source and superconducting nanowire single-photon detectors in one device paves the way for scalable fully-integrated quantum photonic circuits.
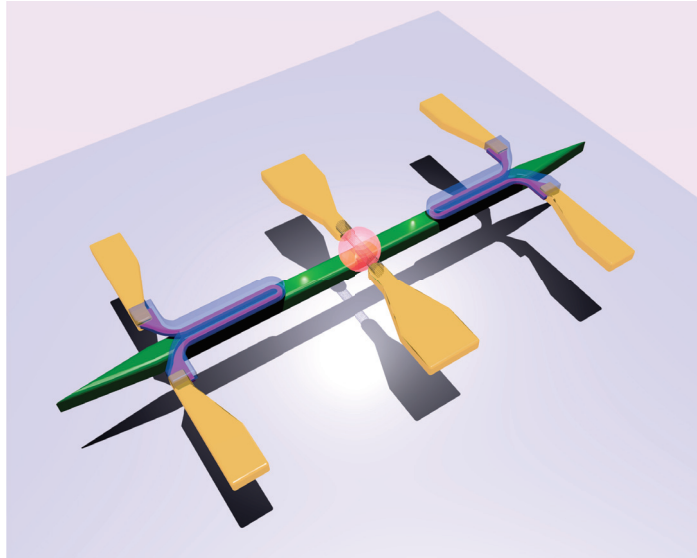
Figure 1.1: Artistic representation of a typical device, containing a single-photon source (center) and two single-photon detectors (left and right), both integrated on the same waveguide.

2 Fundamentals

At the begin of this chapter, different kinds of photon statistics are introduced to distinguish non-classical sources from classical ones. Further, a variety of single-photon sources implemented so far in applications for quantum information processing on-chip is presented. As an example, employment of fluorescing organic molecules, self-assembled quantum dots, and single-color centers in diamond for single-photon generation is reviewed. Subsequently, the single-walled carbon nanotube as a non-classical and classical photon source is introduced. A short description of chirality-depended electronic structures and optical properties of carbon nanotubes is provided. Two mechanisms of light generation in carbon nanotubes, photo- and electroluminescence, are described. The role of exciton generation and recombination in the emission spectra, as well as the impact of exciton localization on the emission efficiency is briefly discussed. Last chapter is dedicated to passive and active elements employed in photonic circuits. Light propagation in planar waveguides and coupling of the propagated light into the far-field or vice versa at the grating structure is shortly sketched. At the end of this chapter single photon detection is briefly discussed.

2.1 Single-photon sources

Deterministic single-photon sources (SPS) that produce individual photons on demand [48] are the key element in many quantum optical applications, such as cryptography, communication, and computing [5,49]. These application are based on generation, manipulation and detection of single photons. [50] There are two classes of SPSs, which can be practically realized: deterministic single emitters and probabilistic sources. The first one contains intensively investigated sources such as single atoms or ions, organic molecules [12,13,14], semiconductor nanocrystalls and quantum dots [19,20,21,22], as well as color centers in diamond [15,16,17,18]. The probabilistic approach is to generate a correlated pair of photons, typically in a non-linear medium (for example, spontaneous parametric down-conversion). [50] The detection of the first photon of this pair reveals the existence of the second one. These sources found a wide application for quantum information. [50] An ideal SPS would have a 100% probability of emitting a single photon, and 0% for multiple photon emission. It would exhibit a highly efficient emission with almost unlimited count rates. Suppression of non-radiative relaxation channels would lead to lifetime-limited decay and narrow spectral lines. [4] Another important property is that the emitted photons should be identical to allow the complexity of quantum optical applications. A perfect SPS would have a negligible timing jitter (dephasing) to satisfy the requirement of being deterministic. However, in the real world the properties of a SPS differ from an ideal one's. For development of a real SPS, typically only few of above mentioned characteristics can be improved simultaneously. Then, parameters, which are important for a particular application are chosen. A variety of single-photon sources with

remarkable improvements in each individual characteristic have been shown in the last decade. In many fundamental quantum optical experiments, single-photon sources in the gas phase, such as ions or atoms, as well as superconducting sources were successfully employed [4,48]. For example, quantum teleportation and entanglement were shown with atoms cooled in a trap, or ions trapped in an optical cavity close to resonance were used for the demonstration of an elementary quantum network. [50] However, only SPSs in the solid state are suitable for integrated quantum optics.
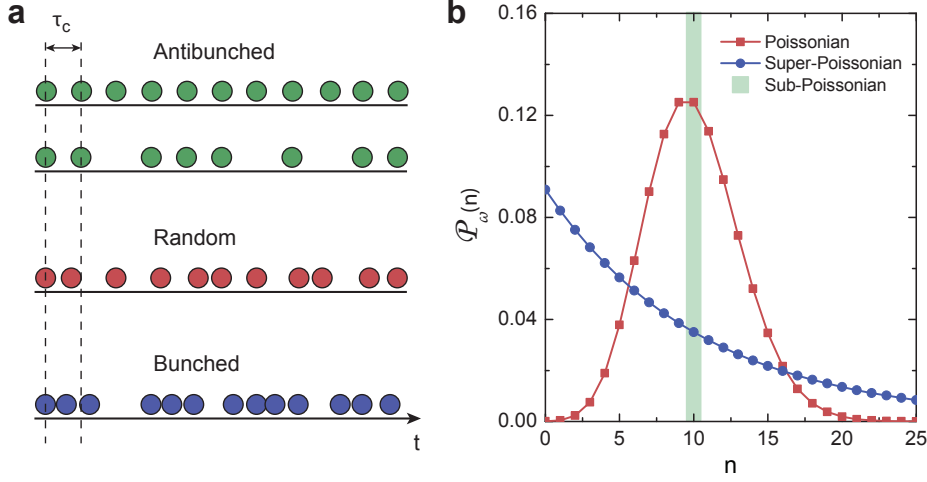
2.1.1 Photon statistics

Before we continue the discussion about single-photon sources, the temporal distribution of single photons (called photon statistics) emitted by light sources is reviewed, and three classes of light are introduced: random, bunched or antibunched.

Concerning this temporal distribution, three different kinds of statistics can be distinguished: super-Poissonian, Poissonian and sub-Poissonian [51]. On the other hand, if we consider emission from some source on a microscopic scale, three classes of light can be defined. They distinguish if photons are emitted chaotic (a period with several photons emitted shortly after each other followed by a time span with no photons), randomly, or with constant time periods between each other. A prominent example of random light is a coherent laser beam, while chaotic (bunched) light is observed from a thermal source (hot filament or discharge lamp) [48,50]. Both are classical sources, and it is straightforward to obtain light from such sources in the laboratory and in nature. The third class in this picture is purely quantum and has no analogues in the classical world, therefore such sources have been realized only recently along with a tremendous progress in high efficient single-photon detection. Due to a variety of losses on the path between the source and detector (i.e. absorption or scattering), and also because of limited detection efficiency, which represent the temporal distribution of detection events, a counting statistics can significantly differ from the initial photon statistics of a source.

Fig. 2.1a illustrates the above mentioned three classes of light: random, bunched, and antibunched. The latter examplesalso the case, if some photons were lost. The coherence (characteristic) time τ_c is denoted for comparison. On the time scale of τ_c, classical thermal and random sources emit several photons or none, while a non-classical source emits exactly one photon during each time span τ_c. However, loss significantly alters the statistics for perfectly antibunched light. If it is degraded too much, it appears as a random sampling, which obeys the Poissonian statistics. Therefore, only after single-photon detectors with a high efficiency were developed, the measurement of this statistics became possible [51]. While for a detection efficiency of 100 % detection events are separated by regular gaps, for a detection quantum efficiency of 20 %, on average only one out of five photons can be detected. Therefore, detectors with high efficiency are indispensable, and minimizing the loss prior to detection is required. The Poisson statistics describes coherent light with a constant intensity by the equation

$$\mathcal{P}(n) = \frac{\overline{n}^n}{n!} \exp\left(-\overline{n}\right)$$

Figure 2.1: Photon statistics. (a) Photon counting times for antibunched (top), coherent or random (middle), and bunched (bottom) light. The ideal antibunched light shows a constant time interval between the photons, τ_c, if all photons are detected. If several photons are missing, this statistics degrades, and turns into random light in the worst case. τ_c is the time scale of the photon number fluctuations (for example, the lifetime of an excited state). (b) Comparison of three photon statistics with Poissonian (red), super-Poissonian (blue) and perfect sub-Poissonian (green) distribution. The average number of photons in all cases is 10.

with $n = 0,1,2..$, where $\mathcal{P}(n)$ is the probability to detect n photons, and $\overline{n}$ is an average number of photons, emitted by the source at a time (Fig. 2.1b). The actual value of a photon (for Poisson statistics) is always an integer random number n, which fluctuates around the average value $\overline{n}$ with a standard deviation $\sigma = \sqrt{\overline{n}}$ of this value [51]. Super-Poissonian light is described by a Bose-Einstein distribution

$$\mathcal{P}(n) = \frac{1}{\overline{n}+1}\left(\frac{\overline{n}}{\overline{n}+1}\right)^n$$

with a standard deviation of $\sigma = \sqrt{\overline{n}+\overline{n}^2}$, which is much larger than in the Poissonian case, due to thermal fluctuations of the photon number [51]. The average intensity of the thermal light is expressed by Planck's law $\overline{n} = 1/(\exp(\hbar\omega/kT) - 1)$. Considering ideal sub-Poissonian light with a constant time period between all photons, the probability $\mathcal{P}(n) = 1$ for $n = \overline{n}$ and $\mathcal{P}(n) = 0$ for all other $n \neq \overline{n}$. This ideal light has a constant non-fluctuating intensity.

To observe the photon statistics of a single-photon source, the incoming photon stream is divided by a 50:50 beam splitter. However, the splitting is a rather random process (although with a constant probability ratio 1:1) [51]. Moreover, the splitting medium introduces an additional random loss into both photon fluxes. Hence, the time gap τ_c is not regular anymore. Therefore, for a real non-classical source, the statistics degrades due to loss, but remains narrower than a Poissonian one (or follows it for high loss). The standard deviation, which can be measured in the laboratory, is then $\sigma \leq \sqrt{\overline{n}}$. Therefore, the intensity of real non-classical sources fluctuates on a microscopic scale, like for random light, however more regularly.

2.1.2 Second-order correlation function

The vanishing probability of emitting two photons simultaneously in one excitation cycle is known as photon antibunching [46]. Antibunching assures that during a distinct time period, the emission of the second photon is prohibited or remains negligible. To examine a potential single-photon source, a photon correlation experiment has to be performed. From this experiment, the second order correlation function $g^{(2)}(\tau)$ is extracted, which describes the statistical character of the intensity fluctuations. Only the correlation between fields intensities ($|\overrightarrow{E}|^2$) is considered, and hence, no phase information is needed. Typically, the experiment is performed in a Hanbury Brown and Twiss (HBT) configuration [52]. The emission from a light source is split equally into two arms and detected by two detectors. In modern systems, these are single-photon detectors, connected to a correlator, which records all arrival times of the incoming single photons with high timing accuracy. Then the raw data can be processed by the correlator, either in real time or later. The splitting is realized by a 50:50 beam splitter, which can be a Y-shaped planar beam splitter or a directional coupler in case of an integrated waveguide-coupled source, or a dichroic prism as well as a half-silvered mirror for a free-space optical beam. The second order correlation function is expressed by the following equation

$$g^{(2)}(\tau) = \frac{\langle I(t) \cdot I(t+\tau) \rangle}{\langle I(t) \rangle \langle I(t+\tau) \rangle} = \frac{\langle n_1(t) \cdot n_2(t+\tau) \rangle}{\langle n_1(t) \rangle \langle n_2(t+\tau) \rangle},$$

where $n_1(t)$ and $n_2(t+\tau)$ are the photon count numbers, recorded with first and second detectors at the times t and $t+\tau$, respectively. The minimal timing bin (τ) of the correlator used in our experiment is $\tau = 4\,\text{ps}$. The correlator has a dead time of $90\,\text{ns}$ - the time before next photon in one channel can be detected. $\langle n_i(t) \rangle$ is the value of the count number, averaged over time t. The second-order correlation function is normalized with $g^{(2)}(\tau) = 1$ for large $|\tau|$. The light from some source is classified according to the value of the second-order correlation function at zero delay time ($\tau = 0$): bunched light with $g^{(2)}(0) > 1$, random light with $g^{(2)}(0) = 1$ and non-classical antibunched light with $g^{(2)}(0) < 1$ (Fig. 2.2). Therefore, when measuring $g^{(2)}(0)$ of a source, its nature (thermal, coherent or non-classical) can be defined in a second-order correlation experiment. The "nature" of a single-photon source means here the relative probability of multi-photon emission to the probability of single-photon emission [4]. Considering thermal light emitted by a macroscopic object such as a hot filament, many independent emitters contribute to the signal, which are spatially incoherent. Therefore, the field intensity is not correlated, but rather chaotic. Hence, many photons can be emitted simultaneously. For sources which reveal bunching with a Gaussian line shape, the second-order correlation function can be calculated as

$$g^{(2)}(\tau) = 1 + \exp\left(-2 \cdot \left| \frac{\tau - \tau_0}{\tau_C} \right| \right),$$

whereas bunching with Lorentzian line shape can be expressed as

$$g^{(2)}(\tau) = 1 + \exp\left(-\pi \cdot \left(\frac{\tau - \tau_0}{\tau_C} \right)^2 \right).$$
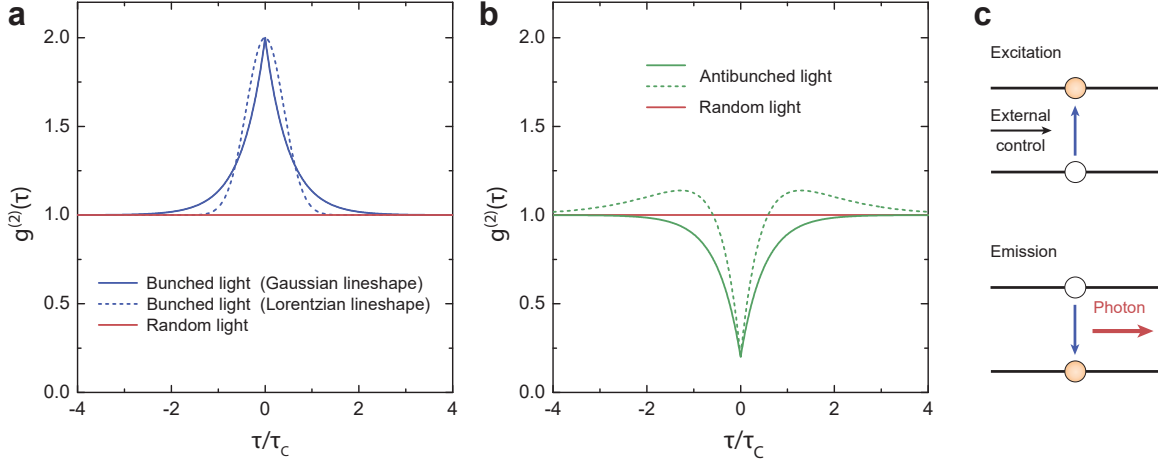
Figure 2.2: Second-order correlation function. (a) Bunched light with $g^{(2)}(\tau) \geq 1$ for Gaussian (solid) and Lorentzian (dashed) line shape of the source. Here, the coherence time $\tau_C = 1$. (b) Antibunched light with $g^{(2)}(0) < 1$ (solid) and $g^{(2)}(\tau) \leq g^{(2)}(\tau)$ (dashed). The correlation function of random light (straight red line) with $g^{(2)}(\tau) = 1$ is shown for comparison. (c) Excitation of a two-level system and emission of a photon due to transition into the ground-state (*adapted from* [4]).

In Fig. 2.2a exemplary curves with $\tau_C = 1$ are shown. In case of antibunched light the second-order correlation function is

$$g^{(2)}(\tau) = 1 - \text{const} \cdot \exp\left(-2 \cdot \left|\frac{\tau - \tau_0}{\tau_C}\right|\right)$$

(Fig. 2.2b). The central dip, whose value $(1-\text{const})$ reflects an upper bound of the multiphoton emission probability, is in the range of $0 \leq g^{(2)}(0) < 1$. An ideal single-photon source is perfectly antibunched: $g^{(2)}(0) = 0$, thus the probability of a multiphoton emission is zero. For comparison, an attenuated laser source shows $g^{(2)}(\tau) = 1$. Another characteristic of a single-photon source is indistinguishably, which can be characterized by the ratio $2 \cdot \tau_S/\tau_C$, where τ_S is the source lifetime and τ_C is the coherence time. This value has to be equal to 1 for an ideal source. Although the phenomena of sub-Poissonian statistics and antibunching are signatures of non-classical light, they are not identical. Nevertheless, non-classical light frequently shows both effects at the same time [51].

The mechanism of antibunching differs for different single-photon sources. In the case of a two-level system (Fig. 2.2c), the antibunching arises because the transition of the system to the ground state leads to photon emission, and only after some time the system is excited and a photon can be emitted again [48]. The first observation of antibunching, proving the non-classical nature of light from a single-photon source, dates back to 1977. [53] At the time, Kimble et al., verified antibunching on a very diluted atomic beam, where only a single atom was in the laser focus at a given time [48,53]. In condensed matter, where single objects are much easier to manipulate, photon antibunching was detected in the fluorescence of single molecules (approximated as a three-level system) [24]. Single quantum dots, triggered optically [19] and electrically [54], also have shown a strong suppression of multiphoton emission

under pulsed and CW excitation. In both cases, a certain wavelength spectrally selected between several lines was used for the correlation measurements.

2.1.3 On-chip single-photon sources

Now, we concentrate on condensed matter single-photon sources which can be integrated on-chip, and compare the advantages and disadvantages, their delivery rates and spectral properties with detailed descriptions of several of the most promising examples. Important characteristics of these sources are presented in a Table. 2.1 for visual clarity. Of great interest are electrically-excited single-photon sources, because of their scalable integration and no necessity for additional light sources and spectral filtering of its radiation.

Organic molecules generate single photons at cryogenic and room temperature. The radiation decay time is almost lifetime-limited, this means emission of indistinguishable photons. However, the molecules are not photostable and undergo irreversible changes due to high-power or longtime optical excitation. Therefore they have to be embedded in a protective hosting environment (polymers or crystals) to suppress the destructive chemical reactions. Additionally, the organic molecules exhibit blinking (intensity fluctuations), as semiconductor nanocrystals also do. The latter are significantly more photostable than the molecules, but not lifetime-limited due to spectral diffusion, and therefore are not indistinguishable. Also the lifetime is very long compared to other single-photon sources, which limits the brightness of the nanocrystal based source. [48] Nevertheless, strong antibunching is observed due to the efficient mechanism of exciton-exciton annihilation, which suppress multiphoton emission in a single nanocrystal. [48] Single-color centers in diamond are very promising as single-photon sources operating at ambient conditions. Among ~ 500 structural defects in diamond, the most intensively studied are nitrogen vacancies (NV) [16]. Silicon vacancies (SiV) in diamond are also promising [55]. Concerning indistinguishability of the sources, which is required for scalable complex systems, the NV centers in diamond are not ideal, due to spectral instability among an ensemble of NVs and small probability of coherent photon emission. Hence, characterization and preselection have to be performed, similarly for (III-V) semiconductor quantum dots. The emission of SiV centers, on the contrary, show the capability of generation of coherent photons and excellent spectral stability. Therefore, SiV centers are suitable for generation of indistinguishable photons and hence for scalable integration. The only disadvantage is their sophisticated integration into nanophotonic circuits. Alternative SPS, based on nanoscale semiconductors (for examples, 2D monolyer of transition metal dichalcogenides [26] or 1D semiconducting carbon nanotubes [44]) with a direct optical bandgap in the visible and near-infrared range, were demonstrated. Bright, stable, and reliable single-photon emission in the visible and near-infrared spectral ranges can be realized from localized excitons. In case of semiconductor monolayers, the localization traps were found to be placed on one-dimensional sites or scratches. The origin of single-photon emission will be discussed later (sub-chapter 2.2.4) based on semiconducting carbon nanotubes. Now we consider the single-photon generation in some representative solid-state single emitters in more detail.

SPS	Wavelength range	Wavelengths	Bandwidth	Count rate	Quantum yield
Single molecule (cryo) [4]	vis-NIR	500 − 750 nm (ZPL + broad)	broad, ZPL < 0.1 nm	100 MHz	0.04
Single molecule (room T) [4]	vis-NIR		< 20 nm	100 MHz	
Single molecule (cavity coupled) [13,48]	vis	∼ 600 nm (ZPL)	0.4 nm	100 MHz	0.1
Color center (NV) [56]	vis-NIR	640 − 800 nm (ZPL + broad)	broad (a.c.) < 50 nm / ZPL < 3 nm (cryo)	10 MHz (a.c.)	0.022 - close to 1
Color center (SiV) [17,23]	vis-NIR	phonon-side-band (760 − 860 nm) / 737 nm (ZPL)	broad, ZPL < 0.1 nm	100 MHz	∼ 0.7
Quantum dot [4,48]	vis-NIR	850 − 1000 nm InAs in GaAs / 1300 − 1700 nm InAs in InP	< 0.1 nm (cryo)	1 GHz	close to 1 (cavity or weak excitation)
Semiconductor nanocrystal [48]	vis-NIR	460 − 660 nm (broad)	∼ 20 nm (a.c.) / < 1 nm (cryo)	10 MHz	close to 1 (at bright period of the blinking)
SWCNT (PL) [45,46]	vis-NIR	900 − 1600 nm, diameter-dependent	∼ 0.03 nm susp.	100 MHz	∼ 0.01 − 0.3
SWCNT (EL) [57]	vis-NIR	900 − 1600 nm, diameter-dependent	< 50 nm supp.	100 MHz	$10^{-4} − 10^{-3}$

SPS	Multiple excitons	$g^{(2)}(0)$	Emission lifetime	Stability	Dark state/bunching	Operation condition
Single molecule (cryo) [4]	no	0.09	< 5 ns	yes	yes	1 − 10 K
Single molecule (room T) [4]	no		< 5 ns	no	yes	a.c.
Single molecule (cavity coupled) [13,48]	no	∼ 0.5	∼ 2 ns	yes	yes	1.8 K
Color center (NV) [56]	no	0.07	∼ 1 − 10 ns	yes	yes	a.c./cryo
Color center (SiV) [17,23]	no	0.26	∼ 2 ns	yes	yes	a.c./5 K
Quantum dot [4,48]	yes	close to 0	few ns, < 300 ps for cavity coupled	yes, sometimes blinking	no	1 − 30 K
Semiconductor nanocrystal [48]	no (reduced by EEA)	close to 0	20 − 30 ns	no, blinking	yes (no if neutral)	a.c.
SWCNT (PL) [45,46]	yes, reduced by EEA	≤ 0.3	< 5 ns susp./ < 100 ps supp.	yes, blinking if supp.	yes	a.c./4.2 K
SWCNT (EL) [57]	yes, reduced by EEA	∼ 0.5	< 100 ps supp.	yes	yes	cryo

Table 2.1: Comparison of single-photon sources. a.c.: ambient conditions, susp.: suspended SWCNT, supp.: supported SWCNT.

Organic molecules

Fluorescence of single molecules (some organic dyes and aromatic molecules) shows photon antibunching, which was intensively investigated at cryogenic and ambient conditions [4,24] and was a first precedent of an antibunching observation in a condensed-matter system [48]. A single molecule can be approximated by a 3-level system - a singlet ground state, singlet excited state and triplet intermediate state. Each of them consists of several vibrational energy levels, since compared to electronic states of ions and atoms, electronic states of molecules in condensed-matter are manifold as result of additional vibrations and phonons. The photon emission occurs due to a transition between one of the vibrational levels of the excited state $|S_1\rangle$ and one of the ground states $|S_0\rangle$. [4] Owing to these additional vibrational levels, which split the ground state and first excited states also at zero temperature, the emission spectrum of the molecules is broadened over many frequencies. Typically, a fs-pulsed laser is used to generate the photons on demand. Alternatively, a CW laser can be used. Single-photon emission is modulated then with an external electrical field, which can shift the absorption line of the molecule out of resonance with the laser frequency [4]. A significant disadvantage of single molecules is photo-bleaching, the irreversible changes in the molecule's structure. Photobleaching leads to a significant reduction in the emission intensity, its fluctuation, and to changes in the emission wavelength. Usually, it occurs after 0.5 up to several hours of continuous illumination at large optical power, up to complete break of fluorescence. Photo-bleaching is especially strong under high power excitation and at ambient conditions (owing to many photon absorption and excitation in the higher states, which activates various photochemical processes). [48]. To avoid this effect, the single molecules can be embedded in a crystalline matrix and measured at cryogenic temperatures. To obtain indistinguishable long-lived and narrow emission, the zero-phonon line can be chosen, enhancing the emission by coupling to a cavity [13]. At room temperature, the absorption and emission spectra are significantly broadened (typically $300\,\text{cm}^{-1} \sim 10\,\text{THz}$). Moreover, at higher temperatures the stimulated emission decay time is much shorter than the lifetime of the excited vibrational state due to thermal fluctuations. [48] At room temperature an additional metastable intermediate state is allowed (transition to this state occurs much more often, than at low temperatures). This intermediate state is called a "dark" state, because the single-photon emission stops, while the molecule is in this dark state and it translates into the ground state non-radiatively. This process is called intensity blinking. Therefore, the overall emission intensity decreases and the long-time scale bunching appears [48]. Also, the transition to this intermediate state $|D_1\rangle$ occurs with much smaller probability than to the normal excited state $|S_1\rangle$. [4] Molecules with high photo-stability isolated from the environment have been operated as single-photon emitters also upon electrical excitation at room temperature. [14] The exciton binding energy for organic molecules are around $1\,\text{eV}$, which allows for single-photon generation also at room temperature.

Self-assembled quantum dots

Self-assembled quantum dots are typically grown in a high-band-gap semiconductor by chemical vapor deposition or with molecular beam epitaxy, creating embedded islands of

low-band-gap semiconductor (for example, III-V InAs in GaAs or GaAs in AlGaAs and InP in GaInP). Owing to the tiny sizes of quantum dots, electrons and holes occupy discrete energy levels. The radiative transition of the system into the ground state results in a single-photon emission. In a weak-excitation regime a photon can be produced on-demand [4]. In a high-excitation regime the non-radiative exciton-exciton annihilation in a quasi-zero-dimensional system saturates the photoluminescence, which suppresses the multi-photon generation. The clean surface of the dots results in very high radiative recombination rates and photostability. [48] Owing to high purity of the quantum dots there are not enough defect sites, which localize the excitons and leads to non-radiative exciton-exciton annihilation. Hence, in self-assembled quantum dots multiple excitons can coexist. Therefore, the single-excitonic line has to be spectrally separated and selected to cut-off the multiple-excitonic emission. The emission of the single quantum dot, extracted with a monochromator, is bright, stable and narrow at low temperatures. This results in approximately zero antibunching dip. The typical lifetime is several nanoseconds or less. The quantum yield at cryogenic temperatures is close to 1, if the spontaneous emission rate is enhanced due to coupling to a cavity. Also the lifetime is reduces in this case ($< 300\,\mathrm{ps}$). An integration of an optically pumped InAs quantum dot into a photonic crystal slab waveguide has already been demonstrated [21]. Optical power-dependent count rates in the kHz range and second-order correlation $g^{(2)}(0)$ ranges from 0.25 to 0.45 were shown. Cryogenic temperature is necessary for exciton localization because of a small exciton binding energy (tenth of meV). Otherwise, the thermal energy surpasses the binding energy. Electrically pumped InGaN semiconductor quantum dots have been demonstrated with a relatively small probability of multiphoton emission of ~ 0.2 at $10\,\mathrm{K}$ (after background correction). [27]

Color centers in diamond

Single-photon sources, based on the luminescence of defects in a diamond structure, are widely used. This luminescence can be excited optically and electrically, what makes them suitable for the scalable application of a source. The first detected single color center in diamond was a nitrogen vacancy [16] (Fig. 2.3a) - a defect in the atomic structure due to a substitutional nitrogen atom along with an adjacent vacancy. This is probably the most investigated system and most promising candidate as a room-temperature single-photon source for numerous of applications, such as quantum computation and cryptography [56]. There are negatively charged NV^{-1} and neutral NV^{0} centers. The NV center forms a discrete level system, which is very sensitive to external electric fields and to strain at cryogenic temperature, but it is almost unaffected at room temperature [56]. For example, the hyperfine structure of the NV^{-1} center consists of the spin triplet ground state ($m = 0, \pm 1$) and the first excited state, which is also the spin triplet. There are additional intermediate states, which leads to non-radiative channels for transitions from the excited to the ground state. The transitions between the sub-levels depend on the spin state, what makes the NV^{-1} center attractive for quantum information processing as a solid-state spin qubit [56]. This NV^{-1} center electronic spin was also manifested for quantum memory, which is an important building block of quantum information processing [58]. Therefore, the number of applications of single NV^{-1} centers, which have been already demonstrated is impressive [56], compared to

neutral vacancies, which show a different level system. Both, negatively charged and neutral centers show strong fluorescence from the single-centers, which can be regularly detected using scanning confocal microscopy (Fig 2.3b). NV^{-1} and NV^0 centers can be used for single-photon generation. A pronounced antibunching dip has been demonstrated for a single NV^{-1} center with continuous wave optical excitation [56]. The amplitude of the second-order correlation function at zero delay $g^{(2)}(0)$ was presented to be significantly smaller than 0.5 (Fig 2.3c), thus the probability of a multiphoton emission is negligible. Also, pulsed optical and electrical excitation of the emission from a single defect was demonstrated with a very small $g^{(2)}(0)$ value. This is because multiple excitation is excluded in small-size (actually, 0D) systems. The strong fluorescence of single NV centers implies high quantum yields, efficient shelving in a long-lived dark state, and relatively short excited-state lifetimes, which leads to a bright emission. [56] One general advantage of diamond is its mechanical stability compared to organic molecules. Owing to the rigidity of the diamond lattice, a defect located deep inside is chemically stable against oxygen or other reactive molecules. [48] Typically, noncrystalline diamond is used, which simplifies the sample preparation and enhances the light extraction. [48] Contrary to single organic molecules, single NV centers are photostable under off-resonance optical excitation [56], which makes them suitable for room temperature applications and for continuous high excitation power. The important properties of a single NV center, which separates it from other single-photon sources, are its charged state (negative or neutral), the spin triplet/doublet of the ground electronic state as well as presence of the intermediate state. Similarly to the molecular dark state, this intermediate state can lead to bunching (Fig 2.3c). The negatively charged and neutral NV centers can be identified by the sharp zero-phonon line (ZPL), that is located at 637 nm for NV^{-1} and at 575 nm for the NV^0 center. [56] Additionally to charge, at low temperatures individual centers have different hyperfine structures due to individual strain field, and therefore are not identical.
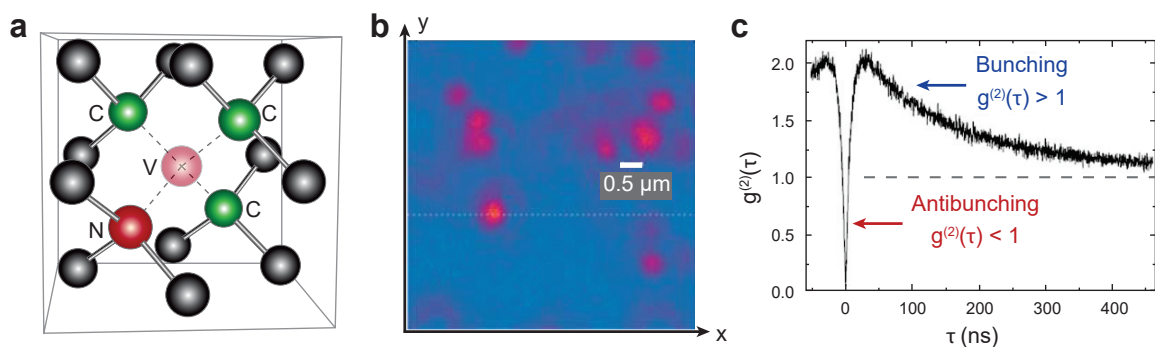
Figure 2.3: NV center in diamond. (a) Schematic of the atomic structure of a single NV center in the diamond lattice. Substitutional nitrogen atom (red), vacancy (transparent) and neighboring carbon atoms (green) (b) Typical image of spatial-resolved emission of a sample, which consists of several NV^{-1} centers, recorded with a confocal microscope setup at room temperature. (c) The correlation measurements reveal an antibunching dip at zero delay well below a value of 0.5 for a single NV^{-1} center upon excitation with a CW laser at room temperature. *Source: (a-c)* [15,56] *copyright: 2006, John Wiley and Sons.*

Photons with energy outside of the narrow-band ZPL are not lifetime-limited and, hence, are not indistinguishable. [48] NVs also can be driven electrically. Single-photon generation from single centers upon electrical biasing was shown by Mizuochi et al. [18]. Second-order correlation with $g^{(2)}(0) \sim 0.4$ at zero delay (without background correction) was measured at room temperature. Another alternative to NV are silicon vacancies [17] (SiV) in diamond, which demonstrates more spectral stability than NVs.

It is surprising, however, that although all of these sources can be excited electrically, so far no electrically-driven SPS was presented to be integrated into photonic circuits. For emerging quantum optical applications it is important to demonstrate both, scalability owing to electrical excitaion and coupling to basic nanophotonic structures.

2.2 Semiconducting carbon nanotubes as single-photon source

In the past few years, optically-excited semiconducting single-walled carbon nanotubes (SWC-NTs) have been established as a source of non-classical light with a prominent antibunching dip at cryogenic temperatures [44,45], and more recently at ambient conditions [46]. This has attracted great interest in the application of carbon nanotubes as single-photon source. An advantage of single-walled carbon nanotube over all other solid single-photon sources is the simplicity of tailoring the spectral range by choosing a suspension with presorted species that fluoresce in the near-infrared spectral range and give a relatively narrow emission line centered at the designed wavelength. At the same time, the count rate can be independently tuned by controlling the excitation power. However, these experiments were carried out with optically excited non-integrated SWCNTs.

A SWCNT is a hollow one-dimensional structure, discovered by Iijima in 1991 [59]. SWCNTs have been extensively studied in the last several decades due to their extraordinary mechanical, electronic and optical properties [37]. A single-walled carbon nanotube can be imagined as graphene (a monolayer of graphite) rolled up into a perfect tube [38] (Fig. 2.4a). Its diameter is about one nanometer, while the length can reach 0.5 meters, exhibiting a huge aspect ratio of up to 10^8, which makes this material unique in its nature [38]. In our devices, carbon nanotubes with a typical length of around one micrometer were used. Semiconducting single-walled carbon nanotubes (sc-SWCNTs) emit light in the visible or near infrared (NIR) wavelength range [40,61] upon optical [62,63,64] or electrical [36,37,65,66] stimulation. Moreover, the structure-dependent sorting methods have undergone a great development in the past decade [41] and allow for realization of bright light sources with well defined electrical and optical properties. An integration of SWCNTs in photonic [33,67?] and electronic [68] circuits enables the accomplishment of passive optical devices with an active nanotube-based component, exhibiting small footprints. SWCNTs are seamlessly integrable into nanophotonic structures. The emitted mode is coupled to the underlying waveguides with a high coupling efficiency, which can be further increased for particular modes using a specially designed cavity.

However, in contrast to optical excitation, single-photon emission from an electrically-driven SWCNT has not been reported so far. Development of an electrically-triggered single-photon source based on carbon nanotubes is essential for the realization of a carbon-based integrated quantum photonic system. Now, we briefly introduce the electronic structure of SWCNTs
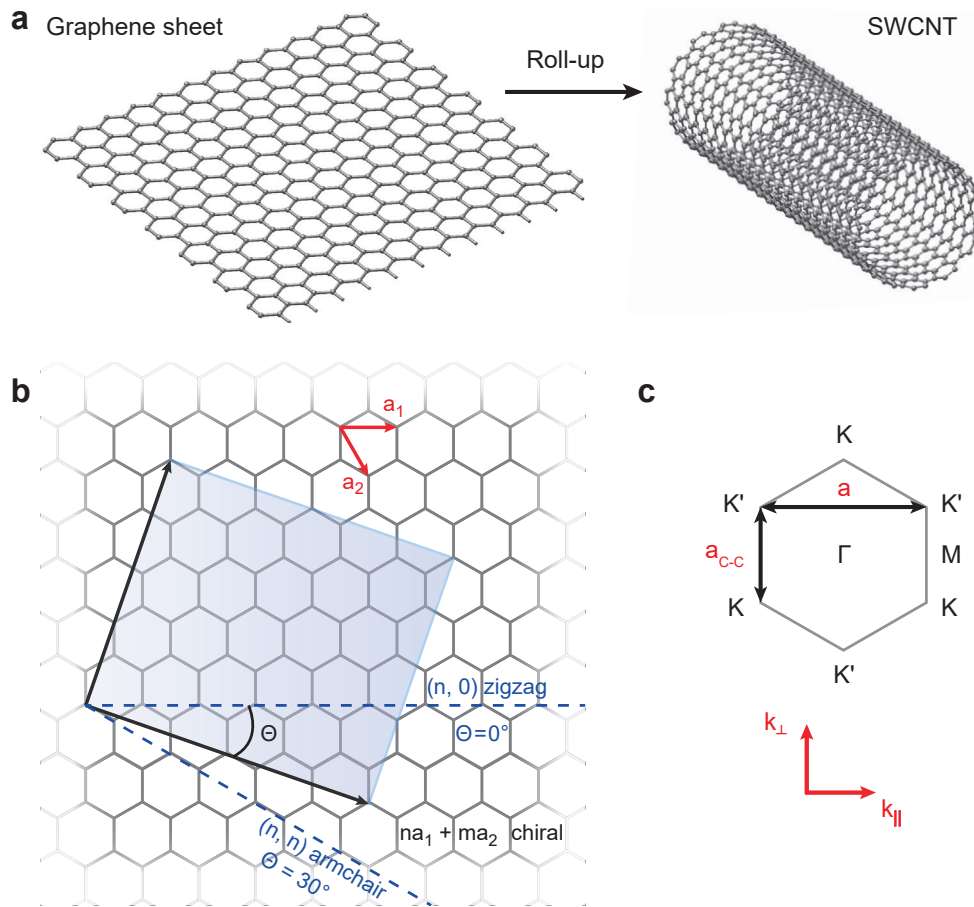
Figure 2.4: (a) Schematic picture of a graphene sheet (2D) rolled into a single-walled carbon nanotube (1D). (b) Graphene direct lattice with basis vectors $\mathbf{a}_1$ and $\mathbf{a}_2$. The chiral indices (n,m) define the roll-up vector $n\mathbf{a_1} + m\mathbf{a_2}$. (c) Reciprocal lattice of graphene, showing the first Brillouin zone with high-symmetry points Γ, M, K, and K'. The carbon-carbon distance $a_{\mathrm{C-C}} = 0.142\,\mathrm{nm}$. *Source: adapted from*[38,60].

and their optical properties.

2.2.1 Electronic structure of carbon nanotubes

The electronic structure of carbon nanotubes is closely related to their atomic structure, such as tube diameter and roll-up angle [40] (Fig. 2.4b, c). The main difference to graphene's physical structure is, that while graphene is a quasi-infinite two-dimensional material, a nanotube is quasi-infinite only in the direction of its axis and consists of only few atoms around the circumference. This additional boundary condition in nanotubes leads to a redistribution of the density of states in so-called van Hove singularities [69,70]. The energy band gap E_{11} between the first two singularities in semiconducting nanotubes is about $1\,\mathrm{eV}$. Carbon nanotube electronic and optical properties are related to curvature effects, depending

on their diameter and chirality. The chirality is determined by the direction (or the angle Θ) at which the graphene is rolled up to a nanotube. This direction, also called chiral vector, (Fig. 2.4b), is characterized by a pair of chiral indices (n, m) and can be expressed as a $\boldsymbol{C} = n\mathbf{a_1} + m\mathbf{a_2}$, where $\mathbf{a_1} = \frac{a_{C-C}}{2}\left(3, \sqrt{3}\right)$ and $\mathbf{a_2} = \frac{a_{C-C}}{2}\left(3, -\sqrt{3}\right)$ are the basis vectors of the graphene honeycomb lattice in the real space [31]. Depending on the chiral angle Θ, carbon nanotubes behave either as a semiconductor with direct band gap, or as a ballistic conductor [38] with "zero" band gap. SWCNTs possess metallic properties, independent on the tube diameter, if the chiral indices $n = m$ and, hence, the chiral angle $\Theta = 30°$ (these tubes are called "armchair"). If the chiral indices satisfy the condition $n - m = 3i$ (with i being an integer value), the nanotubes are quasi-metallic with a small bandgap due to curvature effects, which can be neglected in most applications at room temperature. In reality, the true zero band gap metallic tubes are very rare, because of strain, twist or other defects [71], which open a small ($\sim 0.1\,\text{meV}$) band gap. If $m = 0$, hence the chiral angle $\Theta = 0°$ ("zigzag" tubes), the nanotubes are semiconductors in the band-folding picture [72]. This is true for tube diameters larger than $1\,\text{nm}$, for smaller diameters, however, due to strong hybridization the energy gap is decreased, and nanotubes can be considered as metallic [72]. Those nanotubes with indices satisfying $n - m \neq 3i$ are truly semiconducting [72]. The single-walled nanotube diameter d_t increases with the chiral indices as $d_t = \frac{a_0}{\pi}\sqrt{n^2 + nm + m^2}$, where $a_0 = 0.246\,\text{nm}$ is the lattice constant. The chiral vector length and chiral angle can be expressed through the chiral indices as $|\boldsymbol{C}| = \sqrt{n^2 + nm + m^2} \cdot a_0 = \pi d_t$, and $\cos\Theta = \frac{n+m/2}{\sqrt{n^2+nm+m^2}}$.

In reciprocal space (Fig. 2.4c), the first Brillouin zone is defined by the lattice vectors $\mathbf{b_1} = \frac{2\pi}{3a_{C-C}}\left(1, \sqrt{3}\right)$ and $\mathbf{b_2} = \frac{2\pi}{3a_{C-C}}\left(1, -\sqrt{3}\right)$. The corners of the zone are designated by the high-symmetry points K and K$'$, also called Dirac points, which are not identical. The energy dispersion behaves linearly in the vicinity of these points (for $E \leq 1\,\text{eV}$). Due to the electron confinement around the SWCNT circumference, in the reciprocal space the $\boldsymbol{k}$-vector perpendicular to the nanotube's axis ($\boldsymbol{k}_\perp$) is quantized and has to fulfill the condition $\boldsymbol{k}_\perp \boldsymbol{C} = 2i$ (i is integer) [31,38]. The $\boldsymbol{k}_\parallel$ vector is continuous, assuming an infinitely long SWCNT. Therefore, only discrete subbands are allowed. The band structure of carbon nanotubes can be thought of as slices from the Dirac dispersion cone (Fig. 2.5a, left) perpendicular to $\boldsymbol{k}_\perp$ due to the quantization. Each slice represents the i-th subband with a relativistic dispersion relation given by

$$E_i(k) = \pm\sqrt{(\hbar v_\text{F} k)^2 + \left(E_\text{gap}^i/2\right)^2},$$

where $v_\text{F} = \sqrt{\frac{2E_\text{F}}{m}} = 8 \cdot 10^5\,\frac{\text{m}}{\text{s}}$ is the Fermi velocity at room temperature, $\hbar = 6.582 \cdot 10^{-16}\,\text{eV} \cdot \text{s}$, E_g^i is a electrone-hole subband bandgap and k means $k_\parallel$. Figure 2.5a (right) shows two subbands for semiconducting SWCNTs with chiral indices (8,7) and the corresponding bandgap energies $E_{11} = 0.979\,\text{eV}$, $E_{22} = 1.703\,\text{eV}$. The corresponding density of states (DOS) $g(E)$ is given as the sum over subbands [71]

$$\sum_i g_i(E) = \sum_i \frac{4}{\pi\hbar v_\text{F}}\left(1 - \left(E_g^i/2E\right)^2\right)^{-1/2},$$

where $\hbar = 1.054 \cdot 10^{-34}\,\mathrm{J \cdot s}$, (Fig. 2.5b) and shows van Hove singularities [73]. The approximated energy dispersion of the carbon nanotubes can be described by applying the zone-folding scheme [73] (quantization along the $\boldsymbol{k}_\perp$) to the tight-binding model of graphene [74], where the latter considers the interaction with only nearest neighbors, described by:

$$E(k_\parallel, k_\perp)_\pm = \varepsilon_{2p} \pm \gamma_0 \sqrt{1 + 4\cos\left(\frac{\sqrt{3}a_0 k_\perp}{2}\right)\cos\left(\frac{a_0 k_\parallel}{2}\right) + 4\cos^2\left(\frac{a_0 k_\parallel}{2}\right)},$$

where the parameters γ_0 and ε_{2p} are the interaction energy (defined negatively) between neighboring carbon atoms and energy correction (here, $\varepsilon_{2p} \to 0\,\mathrm{eV}$), a_0 is the lattice constant.

## 2.2.2 Optical properties of SWCNTs

The optical properties of carbon nanotubes are also based on their physical structure, similarly to the electronic properties. One can non-destructively define the optical properties in absorption, Raman, and emission spectroscopy experiments. Emission can be generated due to luminescence (for example, fluorescence) or Joule heating (thermal emission). The latter can be observed from both, metallic and semiconducting species. While the absorption of light is a basic property of the substances, luminescence is attributed only to special materials, for example direct-bandgap semiconductors. Therefore, absorption spectroscopy was utilized first to quantitatively define the composition of the nanotube suspension. [39]
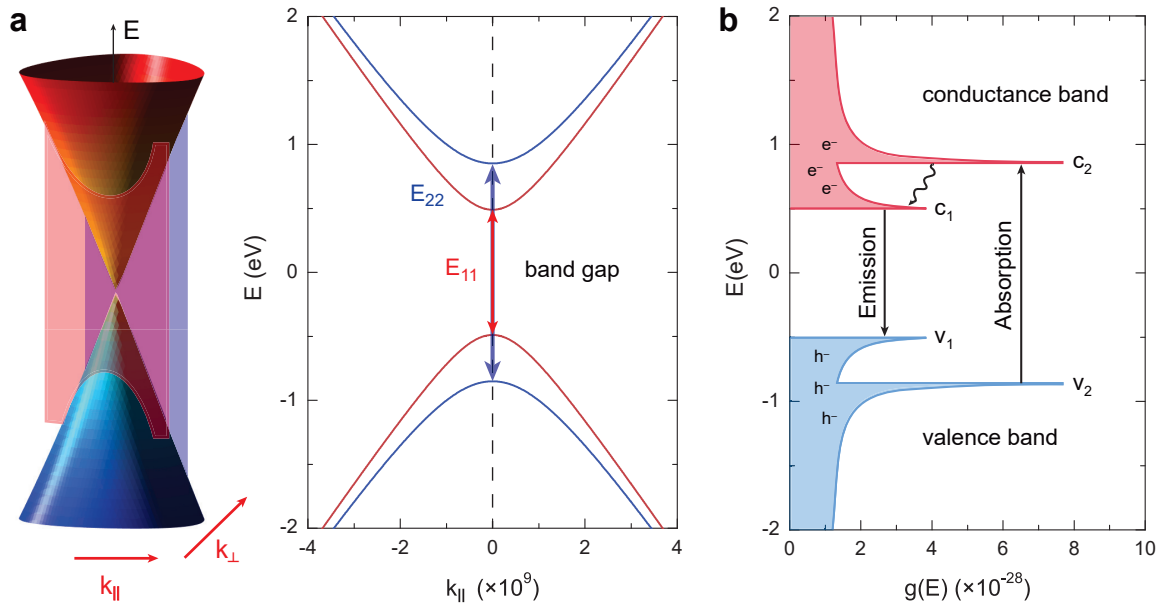
Figure 2.5: Electronic structure of semiconducting single-walled carbon nanotubes. (a) Dirac cone and energy dispersion of sc-SWCNT subbands S_{11} and S_{22} of a (8,7)-SWCNT with diameter $1.02\,\mathrm{nm}$ and energy transitions $E_{11} = 0.979\,\mathrm{eV}$, $E_{22} = 1.703\,\mathrm{eV}$. (b) Respective density of states $g(E)$ (van Hove singularities). *Source: adapted from [38].*

The photoluminescence of individual semiconducting SWCNTs was discovered by O'Connel et al. [61] in 2002. This gives rise to more accurate methods to discover the composition of sc-SWCNT suspension and to assign the chirality of each single nanotube.

In the following, we concentrate on semiconducting nanotubes, as the metallic ones have no bandgap and can not luminesce. Absorption experiments were conducted first, since these could be realized easiest in terms of sample preparation, not needing any complex treatments to absorb light [38]. First experiments showed that optical absorption spectra exhibit distinct peaks, and, thus, differ from the continuous spectrum of bulk graphite, used as a reference. The position of these peaks are related to the optical transitions between the first two singularities in the DOS (E_{11}, E_{22}), predicted by theory. However, these peaks are shifted towards higher energies on $\Delta E (d_t)$ [39]. Thus, as shown by Kataura et al., the values of the SWCNT diameter d_t can be extracted directly from optical absorption spectra (Fig. 2.6a), without the need of transmission electron microscopy. Also the rough estimation of the tube diameter can be performed from the Raman spectra of the breathing mode, which exhibit peaks at distinct energies $E_{\text{peak}} \sim \frac{1}{d_t}$. The theoretical prediction of the diameter's dependency on the subband energies was confirmed by the zone folding method along with tight-binding model calculations [39,75], which reveal the approximated dependency as $E_{11} \approx 0.7/d_t$ (nm) and $E_{22} = 2 \cdot E_{11}$ for semiconducting nanotubes [40]. However, the experimentally measured transition energies of many SWCNT species appeared significantly higher, than the theoretical predictions, generated by parametrized tight-binding calculation of the electronic structure of SWCNTs, and therefore have to be corrected. Initial SWCNT suspensions, independent on the fabrication method, used for production, consist of nanotubes with different chiralities (n, m), and have to be characterized to determine the composition
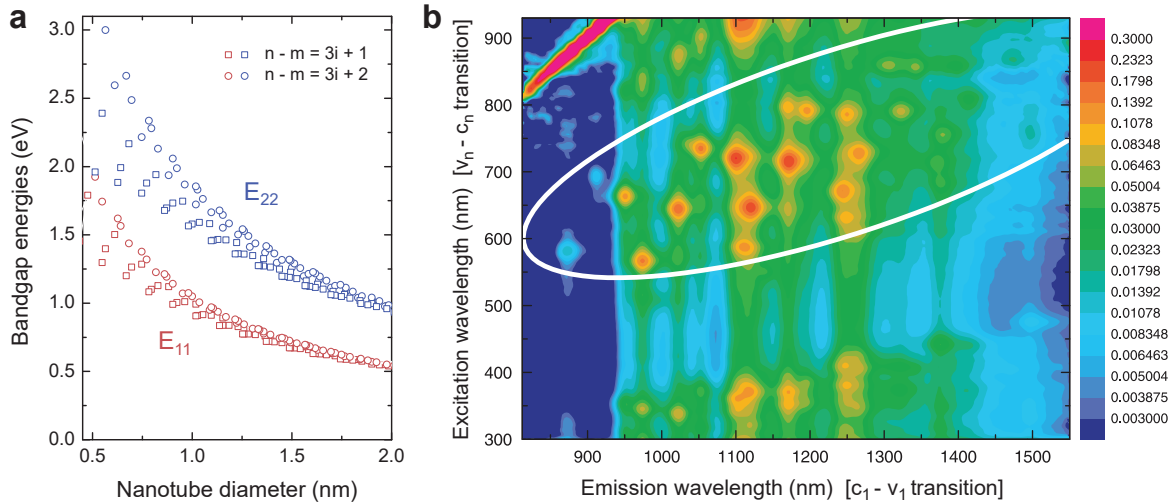
Figure 2.6: (a) Empirical function of bandgap energies E_{11}, E_{22} dependency on the nanotube diameter. Two branches with $n - m = 3i + 1$ (squares) and $n - m = 3i + 2$ (circles) are presented. d_t and, hence, bandgap energies are parametrized through chiral indices (n, m). (b) Phololuminescence intensity versus excitation and emission wavelength for solutions including various SWCNTs, suspended in a surfactant. *Source: (a) adapted from [76], (b) [40].*

of SWCNT suspension. After the photoluminescence of the carbon nanotubes was explored, a new nondestructive and precise technique was developed, allowing the determination of the composition by means of optical spectroscopy [40,62]. The illustration of the photoluminescence process (in approximation of tight-binding model) in SWCNTs is depicted in Fig. 2.5b. If the semiconducting SWCNT is illuminated with light, absorption at the photon energy E_{22} (v_2-c_2) is followed by non-radiative relaxation into the first conductance subband c_1 and emission (c_1-v_1) at photon energy $E_{11} = \frac{hc}{\lambda_{11}}$. It has to be noted, that electrically induced emission would demonstrate peaks at the same wavelengths at similar conditions as result of the same transition levels, although, the excitation can occur between different energy levels. Each allowed transition between the subbands leads to a distinct spot in the emission-excitation plot, whose cross-section strongly depends on the indices (n, m). For a mixture of different SWCNT species a 2D emission map, which contained many spots (Fig. 2.6b), can be recorded. The crucial goal is to characterize the physical properties of each single SWCNT in the mixture [40]. This now widely used technique is applied to designate the suspension components also in our experiment (chap. 3.2.2). Weisman et al. [76] defined empirical functions (Fig. 2.6a) describing the experimental data, which allows the prediction of the optical transition energies for sc-SWCNTs with high accuracy, independent on the theoretical model used by Kataura et al. Two branches with indices satisfying $n - m = 3i + 1$ and $n - m = 3i + 2$ (i is integer) are expressed with different empirical equations. They describe physical properties of semiconducting nanotubes for the first two transition energies E_{11} and E_{22}. No photoluminescence and hence no emission spots appear on the emission-excitation map for the metallic branch with $n - m = 3i$. The white oval in Fig. 2.6b denotes the region of the SWCNT family with optical emission at the energy E_{11}, while excitation occurs mostly at E_{22}. By knowing these energies, the chiral indices can be extracted for each SWCNT. Nevertheless, the tight-binding model remains as a good first approximation for the optical transition, since this prediction satisfies the transition energies for larger tube diameters. It was extended shortly after to predict the subband energies also for smaller tube diameters d_t. [77] The classical tight-binding model does not explain why the E_{22}/E_{11} ratio, as obtained from the experimental data, reaches 1.7, while in this simple theoretical model a ratio of 2 is predicted for large diameters (the "ratio problem" [38]). For smaller diameters the "family spread" problem occurs, i.e. the spread of predicted energies for smaller d_t is much larger in the experiment, than predicted. Extended theory includes long range interaction to account for many-body interactions, as well as C-C bond length variations in SWCNTs with smaller d_t and solving both problems describes the experimental results very well [77].

2.2.3 Photoluminescence

To explain the optical properties of SWCNTs optical transitions have to be considered. As mentioned before, in a first approximation, the light absorption occurs at some E_{ii} subbands after several non-radiative relaxation processes. The recombination of an electron and a hole from c_1 and v_1 subbands appears, and a photon with energy E_{11} is emitted (Fig. 2.5b) [38]. The emission with energy E_{22} (at a wavelength in the visible range) is also possible, but the intensity is much lower compared to the main transition. For light polarized along the nanotube's axis, transitions between the valence and conductance subbands are allowed only

for E_{ii}, $(i = 1,2,3..)$. For polarization across the nanotube's axis, transverse transitions with E_{ij} where $|i - j| = 1$ are allowed (E_{12}). However, these transitions are strongly suppressed due to geometrical anisotropy ("antenna effect") [78]. Both absorption and emission are polarized along the nanotube's axis [62]. Emission lines are narrower for bigger nanotube diameters [62], hence, smaller gap energies. Moreover, the line width decreases with decreasing temperature and the peak center shifts to higher energies (blue shift).

The absorption lines E_{ii} are broadened, as can be seen from the (vertical) cross-section of the photoluminescence excitation spectra in Fig. 2.6b. The vertical green lines in this plot originate from metallic species in the mixture. Besides of the temperature-dependent lifetime broadening, the dielectric environment (contact to other SWCNTs in a bundle or to the substrate) also affects the photoluminescence spectral lines (both absorption and emission); moreover, they can shift them by tens of meV due to special geometrical properties of SWCNTs (all atoms are on the nanotube surface). Therefore, polymer-wrapped SWCNTs, which are widely used in experiments, might have red-shifted values of emission energy E_{11} due to dielectric screening compare to unwrapped species. Reduced charged screening in 1D nanotubes decreases the energy of the emitted photons, predicted by the initial tight-binding theory, since it is easier for an electron and a hole to recombine, if they already are bound by attractive forces to each other, which are less affected by their surroundings. The screening is then further enhanced by the dielectric material, leading to an additional energy shift. Therefore, the knowledge of the experimental conditions is very important for assigning the right chiral indices. The first experiments, which show sharp single peaks in the spectrum, were made on isolated (in a polymer) or suspended ensembles of a small number of different SWCNTs [61,79]. Photoluminescence spectra of individual SWCNTs represent a single asymmetric peak with a width of $10 - 15$ meV at room temperature in air, while the excitation spectra of individual tubes are ca. 30 meV wide. The position of the photoluminescence peak can be shifted due to doping. For example, oxygen doping significantly shifts the resonance of undoped(6,5)-SWCNTs further into the near-infrared spectral range [80]. Hence, it is interesting for the application of doped SWCNTs as single-photon sources at telecommunication wavelengths [46]. The line shape and width are in direct connection with the finite life time of an excited state, which leads to a radiative broadening of the spectral line due to the energy-time uncertainty relation [51]. For the normalized Lorentzian line shape this means that the spectral line width in angular-frequency units satisfies $\triangle\omega_{\text{FWHM}} = \frac{1}{\tau}$. However, the non-radiative transitions are shorter than the excited state lifetime [51], and increase the line width. There is also another type of broadening in solids, which occurs due to local inhomogeneity of the environment supporting the SWCNT.

To describe the photoluminescent transitions more precisely than the theory predicts and to solve the two disagreements between experimental values and theory described above, Coulomb interaction has to be taken into account [38]. There are two energy corrections, excitonic and self-energy (dominating over the first for bigger d_t), which increase both E_{11} and E_{22}. The same dependency on the diameter is observed for electrical excitation of the emission.

2.2.4 Excitonic states in semiconducting SWCNTs

The light absorption produces a strongly bound electron-hole state, an exciton, which was predicted theoretically [78] and shown experimentally [40] for 1D carbon nanotubes. The predicted exciton binding energies are $\sim 1\,\text{eV}$ (around the first bandgap energy). The excitons in SWCNTs are quasi-particles with a size of about a_{C-C} and a diffusion length of about $1\,\mu\text{m}$ at room temperature (the SWCNT length is also in the same order $\approx 1\,\mu\text{m}$ in our devices).

One-dimensional excitonic states can be described by a subbands series (s, p, d...), like Rydberg states in hydrogen atoms, which are below the single-particle bandgap [38] (contribution of Lefebvre et al.) (Fig. 2.7a). This picture can better explain the excitonic states in SWCNTs than the single particle model.

Wang et al. have developed a two-photon absorption model, which supports that optical transitions in SWCNTs arise from excitons [81]. This two-photon absorption process is illustrated in Fig. 2.7a. Two-photon absorption leads to excitation into a p-like exciton state, while single-photon absorption excites s-like state. This is because two-photon excitation obeys different selection rules and can not be explained within the single particle photoluminescence picture [38]. The two-photon absorption process is followed by single-photon emission. Due to transition into different states, the two-photon absorption peak appears at a higher energy in the absorption spectrum than the one-photon absorption peak.

Since absorption and emission occurs between different energy levels, the exciton initially relaxes into the $1s$ subband by non-radiative transitions (denoted by gray dashed lines in Fig. 2.7a). The decay rate is composed from both, radiative (Γ) and non-radiative (k_{nr}) decay rates. Also, other non-radiative processes, such as exciton-exciton annihilation and end quenching, can contribute to the non-radiative decay rate.

Exciton localization in semiconducting SWCNTs

Defects of the nanotube's atomic structure drastically influence its optical and electronic properties, which can be also used as an advantage (i.e. for charge injection or symmetry breaking) [38]. Most important for the current work is that the 0D defect sites can localize the excitons, and therefore antibunching is possible in prolonged 1D nanotube. The first observation of antibunching from photoluminescence in SWCNTs was performed by Högele et al. [44] at cryogenic conditions, where the thermal energy is low enough for localization. Although natural defects exist in almost every SWCNT, the nearest approximation for seamless, defect-free nanotube is single SWCNTs, grown by chemical vapor deposition directly on a chip, suspended over a trench [63,82] or pillars [62]. But SWCNTs deposited (from a suspension) on a substrates like silicon dioxide, or silicon nitride (Si_3N_4) in our experiments, "feel" the dielectric surroundings, OH^--groups on the surface, and its roughness. This introduces a potential well on the defect sites with an energy difference of $\triangle E \sim$ few to tenths of meV (Fig. 2.7b). Hence, the excitons are trapped in a zero-dimensional state, which is locally-induced by defects [46]. This additional energy level is located at $E_{11}-\triangle E$, and due to transition to the ground state a photon is emitted. However, at room temperature, the thermal energy is higher than the trapping energy $k_B T > \triangle E$; thus, such a defect can not localize the exciton. Therefore, the antibunching disappears at room temperature for SWCNTs
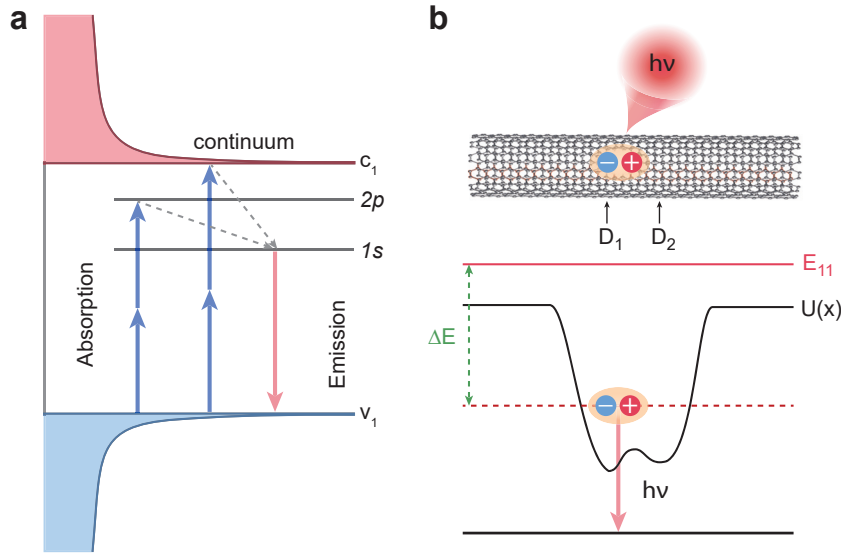
Figure 2.7: Excitonic state. (a) Two-photon absorption as evidence of excitons in a 1D SWCNT. Absorption in a one particle system obeys different selection rules (than without exciton creation) and can either occur at $v_1 - 2p$ or v_1- continuum, while emission occur at $1s - v_1$. D_1 and D_2 are the positions of two defects in the atomic structure of the SWCNT (for example, due to the substrate). (b) Trapped exciton in a zero-dimensional state, induced by a defect (natural or artificial). $\triangle E$ is the energy difference (indicated by the green arrow) between E_{11} (red solid line) and this state (red dashed line). By transition of the exciton into the ground state, a photon is emitted. The potential well $U(x)$ is denoted by a black solid line. *Source: (a) adapted from* [81], *(b) adapted from* [46].

with only naturally-induced defects [46]. Structural defects can also be introduced artificially for scalable and controlled device fabrication. This process allows also for control over the emission position [83] and intensity distribution along the tube. An example of an artificial defects are molecules bound to the carbon atoms of SWCNTs [46] or incorporation into the SiO_2 matrix (creating oxygen dopant states). Then $\triangle E$ amounts to hundreds of meV, which is sufficient to trap the excitons also at room temperature. This trapping prevents excitons from exploiting the quenching sites (nanotube-metal contact interface) and, hence, from non-radiative transition into the ground state. Therefore, effective radiative recombination occurs in the trap. At higher excitation power, several excitons are produced along the nanotube length. If two excitons are trapped in the same potential well, exciton-exciton annihilation (EEA) can occur, and consequently two excitons transit into the ground state without photon emission. This allows a third exciton to generate a single photon during this time, which establishes a single-photon generation. Since the non-radiative transitions due to quenching is then suppressed, the emission is near life-time limited, and such source produces indistinguishable photons. Therefore, a SWCNT with 0D defect sites, induced artificially at a designed position along the nanotube, can be perfectly employed as a room-temperature single-photon source.

2.2.5 Electroluminescence

Both, optical and electrical excitation can be used to generate photon emission from sc-SWCNTs. Hence, since sc-SWCNT is a structure-dependent light source, the central wave-lengths of the emission peaks remain the same for similar excitation conditions. Although, the electroluminescence is broader.

In case of photoluminescence the photon absorption leads to an excitation of the system with subsequent photon emission due to exciton recombination (in approximation). For electroluminescence, charge carriers (or its pair) are produced by current injection. They move directly through the nanotube when an electric field is applied. Depending on the field strength, there are different ways of system excitation. Electron-hole recombination is a dominant mechanism in a weak-excitation regime, while impact ionization is a most probable mechanism at high excitation power. In the first case, for an ambipolar nanotube the electrons are injected from one end while holes are injected from another end [37]. After the transport to the central part of the nanotube they are recombine radiatively. Additional gating of the nanotube in a field-effect transistor geometry can move the recombination site along the nanotube's axis [37] as well as influence the quantum yield of the emission. Carbon nanotube as a semiconductor exhibit the off-state at some combination of the gate and source-drain voltages. The impact ionization occurs, when an accelerated in a high field electron or hole meets on its way an uncharged carbon atom. Their impact results in a creation of exciton (bound carrier pair), which subsequent radiative recombination results in emission of photon. It was noted, that the advantage of electro-excitation of single-photon sources (and accordingly SWCNTs) for future opto-electronic devices is that there is no need for an external laser source and optical filtering. Furthermore, no photobleaching of electroluminescence was observed, in contrast to the case when undoped SWCNTs are subjected to high-power optical excitation over a timescale ≥ 0.5 hours [44]. All our devices are electrically driven by design. Photoluminescence based on the same optical transition can be used to discuss the emission spectra qualitatively. However, the emission bandwidth of electrically driven SWCNTs is larger compared to optical excitation. Also the efficiency of photo- and electroluminescence can differ drastically. In the last case the interface between the nanotube and the contacts plays a crucial role. The difference in a Fermi level results in a Schottky barrier for injection of electrons and holes. The overall resistance of device is a sum of the nanotube intrinsic resistance and additional contact resistances $R = R_{\mathrm{CNT}} + R_{\mathrm{contact}}$. An ideal nanotube resistance is $R_{\mathrm{CNT}} = \frac{h}{4 \cdot e^2} \cdot \frac{L}{l_{\mathrm{MFP}}}$, where L is a nanotube length and l_{MFP} - mean free path.

2.3 Passive and active elements of integrated optics

One of the most intensively employed platform for integrated circuits is silicon nitride on SiO_2 as an alternative to conventional silicon-on-insulator (SOI) technique. Using Si_3N_4 with a high refractive index contrast (in comparison to the surrounding medium) as the waveguide material allows high mode confinement, reducing the bending losses in the tight bends.

Therefore a very high level of integration can be achieved. Moreover, Si_3N_4 is transparent around 1100 nm. Implementing a well-established fabrication techniques, a variety of linear optical components of nanophotonic circuit can be scalably realized.

2.3.1 Planar waveguides and grating couplers

Prolongated planar waveguides are implemented for routing the light on chip, they connect the passive optical elements with an active components of the circuit, like on-chip photon sources and detectors. Planar waveguides have a micrometer-sized rectangle cross-section and are made of materials with a higher refractive index (around $n = 2$ for Si_3N_4 and $n = 1.45$ for SiO_2), therefore they can confine an optical mode in its core. We implement mostly the waveguides, where Si_3N_4 layer was half-thinned, in comparison to fully-etched waveguides. The propagation of light with particular wavelengths is assured in a wider waveguide compare to fully-etched geometry. We describe light as a wave, that means solving Maxwell's equations for this geometry. The propagation of light can be described as a superposition of eigenmodes or guided modes. Such eigenmodes have a constant magnitude along the propagation direction, while only the phase varies. The parameter describing this phase variation along the waveguide is called the propagation constant.

Depending on the geometry and refractive indices, the waveguide can support a single or several modes for a certain wavelength. The group refractive index $n_g(\lambda)$ of the waveguide structure can be calculated according to the equation

$$n_g(\lambda) = n_{eff}(\lambda) - \lambda \frac{dn_{eff}(\lambda)}{d\lambda},$$

where $n_{eff}(\lambda)$ is the effective refractive index of the waveguide. $n_{eff}(\lambda)$ was calculated using finite-element simulation (COMSOL Multiphysics) as shown in Fig. 2.8. The wavelength dependence of the chromatic dispersion in silicon nitride has been accounted for through a Sellmeier equation [84]. For coupling the light into and out of the chip plane, grating couplers [85] are commonly implemented (Fig. 2.9). This is a planar periodical structure, which couple the incident light from the far field into a waveguide. In general the period of the grating structure defines the wavelength, for which a most efficient coupling to a particular guided mode occurs. This wavelength is dependent on the incident angle of a free-space optical beam. The basic operation of a grating coupler is defined by the Bragg condition [86]

$$n_{eff} = n_{top} \sin(\theta) + m \frac{\lambda}{\Lambda},$$

where n_{eff} is the effective refractive index of the grating, n_{top} is the refractive index of the material on top of the grating, θ is the coupling angle measured perpendicular to the chip surface (typically, $\theta = 8°$), m is the particular diffraction mode, λ is the wavelength of incident light, and Λ is the grating period [35]. The grating coupler provides a Gaussian coupling profile centered around the peak wavelength as shown in figure 2.9b, where the transmission spectra through four different devices are presented. Each device contains a waveguide with two equal couplers at its end. The above relation reveals linear dependency of the the central coupling wavelength on the grating period, which also has been proven experimentally (red
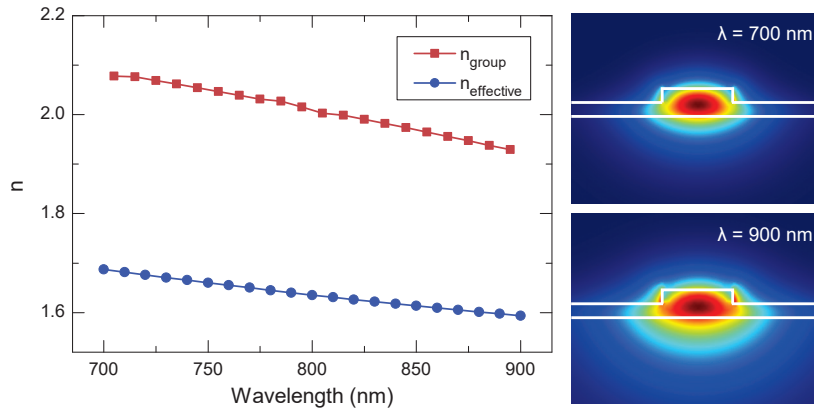
Figure 2.8: Effective and group refractive indices in dependency on the wavelength (left). Cross sectional electric field intensity distribution $\bar{E}^2$ in a single mode rib waveguide (right) for two wavelengths. *Source: Supplementary to [35]*

line in Fig. 2.9c). By varying the grating period, the central coupling wavelength was adjusted at given incident angle of $\theta = 8°$. From the fit, shown in Fig. 2.9c a period can be estimated for each wavelength. Because the optical beam is not parallel, the Bragg-condition is fulfilled for various incident angles inside of its field aperture. Therefore, the bandwidth of the grating coupler has a Gaussian shape with FWHM of about 30 nm. The coupling is polarization sensitive, because $n_{\mathrm{eff}} \cdot \mathrm{TE} \neq n_{\mathrm{eff}} \cdot \mathrm{TM}$ in high refractive index contrast waveguides [87] and provides typically several dB insertion loss. To minimize these losses, a proper fill factor $\left(\frac{w}{\Lambda}\right)$ has to be chosen.
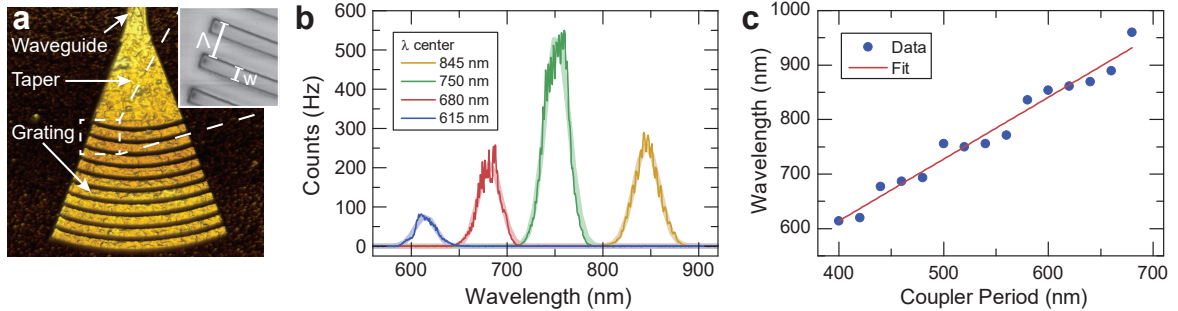
Figure 2.9: (a) AFM image of a grating coupler with period Λ and fill factor $\frac{w}{\Lambda}$, denoted in SEM image (inset). (b) Transmission spectra of four devices with different Λ, hence different central coupling wavelength. All spectra have a Gauss-shaped profile (respective fits are overlayered on measured spectra). (c) Central coupling wavelength for further devices along with a linear fit to these data. *Source: Adopted from Supplementary to [35].*

2.3.2 Single-photon detectors

To carry out the second-order correlation experiment with photons emitted by semiconducting carbon nanotubes and coupled into a waveguide, on-chip single-photon detectors are required. We have employed superconducting nanowire single-photon detectors (SNSPDs), integrated atop of the same waveguide. For accurately probing the temporal distribution of single photons, detectors with high efficiency and high temporal resolution are obligatory. SNSPDs implemented in traveling wave geometry show efficiencies up to 70 % and timing accuracy around 50 ps perfectly meet these requirements. Moreover, they exhibit recovery times in a nanosecond range, that potentially allows for measurement of the count rates up to one Gigahertz. Most important advantage is, that SNSPDs are broad band detectors, operating in visible and NIR ranges, matching the photon energies for sc-SWCNT-induced emission. Another advantage is a low dark count rates $< 1\,\mathrm{Hz}$. In comparison, commercial avalanche photon detectors (APDs) are typically used in fluorescence spectroscopy and correlation measurements. Due to the operating principle based on the semiconductance of the material the detectors are made of, they are sensitive either in the visible or infrared range. For example, the operation range of silicon-based APDs is limited to 400-1000 nm with maximal efficiency around 70 % at the central wavelength with a dark count rate less than 100 Hz. However, detectors for the near-infrared range are more interesting for telecommunication, since the widely used silica-based optical fibers show a low group velocity dispersion at such wavelengths (around $1.3\,\mu\mathrm{m}$ and $1.55\,\mu\mathrm{m}$) [55]. As the name suggest, the SNSPDs operate only at cryogenic temperature range less than 4 K. Detection is based on absorption of photons, which propagates inside the waveguide through the near-field coupling in our traveling wave geometry. This energy locally heats up the nanowire, which creates domains with normal resistivity. Consequently, the current density in the nanowire around this spot increases and reaches the critical value, and the normal domain grows, until it extends to the full nanowire cross-section. At this point, the superconductivity breaks down to the time scale of 30 ps [88], after which, due to self-healing, the superconducting state is restored along the nanowire cross-section. Due to this normal resistivity a voltage spike arises, whose length is, however, around several nanoseconds due to inductance in the nanowire and cables. This process is sensitive to photon energy and nanowire cross-section. Therefore, the spectral sensitivity can be tuned by adjusting the geometry of the nanowire. A suitable geometry for a detector is a long nanowire, bended into meander form, as demonstrated by Gol'tsman et al. [88]. For conventional SNSPDs, which are not waveguide-integrated (Fig. 2.10), a photon beam incidents the detector from the top. Therefore, such a geometry leads to increasing the probability that the photons strike the nanowire and, hence, are not lost [55]. A perfect single-photon detector exhibits a linear proportionality between the numbers of photons incident to the detector area and the detection probability [88]. The meander is connected to metallic contacts, which are used for biasing the nanowire and for detection by measuring its resistance. A crucial parameter for the detector performance is a constant bias current, at which the detector is operating, compared to the critical current, past which superconductivity can not be restored and nanowire has a normal resistance. The bias current inherently influences the detection efficiency and dark count rate of the SNSPDs (for a given geometry). Ideally, a detector has to be biased at the optimal value of the current, where a maximum of internal
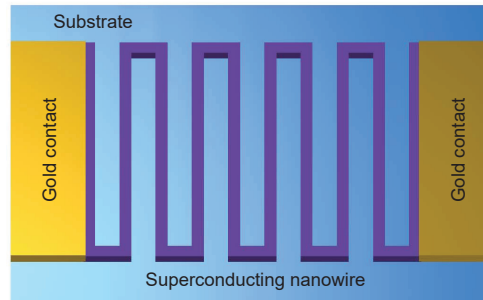
Figure 2.10: A schematic of a superconducting nanowire single-photon detector. The detector has a meander form and is made of niobium nitride.

quantum efficiency is achieved while the dark count rate is minimized, hence the signal to noise ratio is optimized. Around this optimal biasing value the linearity of detector response to the number of incident photons can be ensured.

In the next chapters the integration of carbon nanotubes into nanophotonic circuits is demonstrated.

3 Device realization steps

This chapter outlines the device layout for waveguide-coupled single-walled carbon nanotube (SWCNT) sources. The on-chip experiments and materials, used for fabrication of photonic circuits, are described. The influence of the metallic contacts geometry and its proximity on optical transmission is discussed. In the second part, a brief description of fabrication procedures is given. Then, absorption spectra of carbon nanotube suspensions, sorted by nanotube chirality, are presented. At the end, the deposition method of SWCNTs from sorted suspensions and subsequent electrical transport characterization is discussed.

3.1 Nanophotonic device layout

The SWCNT-based emitter is hybridly integrated with nanophotonic circuits. To explore the properties of such an on-chip emitter and its potential applications, various devices were realized. Typically, all carbon nanotube devices in our experiment consist of three main components - planar silicon nitride waveguides for high mode confinement, metallic contacts, and a carbon nanotube bridging them and aligned perpendicular to the waveguide. The schematic illustration (Fig. 3.1a) shows the layered structure of the device. The nanotube is in direct contact with the waveguide surface, while the nanotube's ends are connecting to the electrodes from the top. The cross-section of the waveguide is superimposed with the calculated electric field intensity $\overrightarrow{E}^2$ for the fundamental mode TE_{00}. In Fig. 3.1b, the central structure of our device is presented. The SWCNTs are visible as thin lines in-between the contacts (inset). Two different waveguide geometries were realized for propagation of light in the visible range up to 1000 nm and near-infrared (NIR) wavelength range around the telecom-band (1550 nm). Also, different substrates were used in these two cases. The layers assigned in Fig. 3.1a have typical thicknesses of 200 nm (Si_3N_4) and 2000 nm (SiO_2) for guiding visible light. For infrared wavelengths, substrates with 330 nm and 3300 nm thickness were used. All experiments described in chapter 4 were performed in the visible range, while for non-classical results (chapter 5), light in the infrared range was explored. This choice is based on the detector sensitivity range which is around 400–1100 nm in case of fiber-coupled and free-space experimental setups (applied for collecting the results in the chapter 4), while broad-band detectors are employed in the last chapter. Nevertheless, the telecom-band (around 1550 nm) is most attractive for non-classical experiments on chip. The waveguide geometry (width and height) have to be optimized to assure propagation of only the fundamental mode. The optimization of the waveguide parameters was performed with the commercial software (COMSOL Multiphysics) due to simulation in a frequency domain prior to fabrication. The results for the visible wavelength range are shown in Fig. 3.2a and b. Typically, half-etched waveguides ($\frac{d}{h} = \frac{1}{2}$) were used in both cases (d = 100 nm and
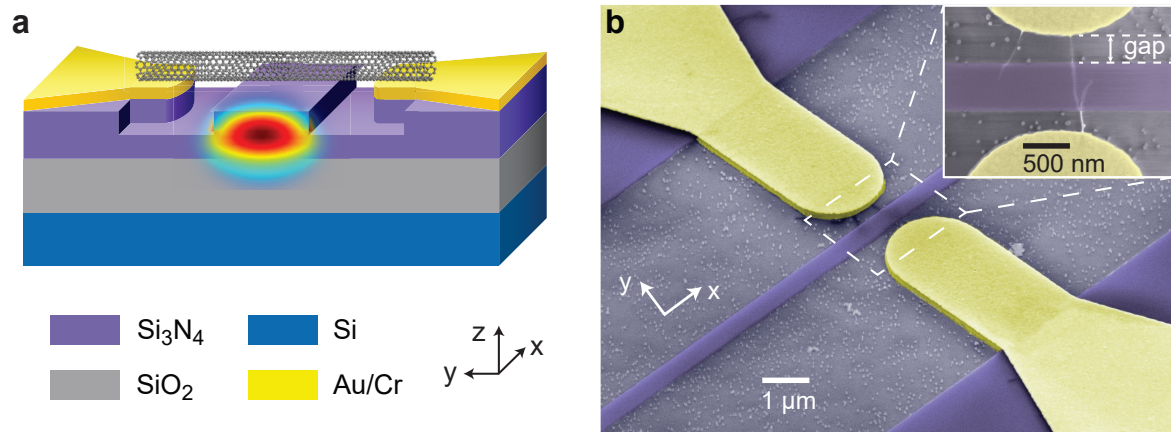
Figure 3.1: SWCNT-based device layout. (a) Schematic illustration of the device's layers. The ridge waveguide is half-etched into Si_3N_4 on top of an insulating SiO_2 layer with silicon substrate. Gold electrodes on a $5\,nm$ chromium adhesion layer are in close proximity to the waveguide (the materials are distinguished by color). The SWCNT is in direct contact with the waveguide and electrodes. To illustrate the coupled mode from the SWCNT, the simulated spatial distribution of the electric field intensity $\vec{E}^2$ is overlayed with the waveguide cross-section. (b) Colored tilted SEM picture of the waveguide, metallic contacts and SWCNTs overpassing them. Inset: High contrast SEM picture of the same device. The SWCNTs between the contacts are clearly visible. *Source:* [35].

$165\,nm$, respectively). Waveguides with such a rib-shaped cross-section (Fig. 3.2b, inset) have the advantage of supporting a mode at a particular wavelength in a narrower waveguide compared to an etched-through one[87], which is important to decrease the mode absorption by the metal electrodes. The minimal waveguide width for constant wavelength (Fig. 3.2a) and theoretical cut-off (Fig. 3.2b) - the maximal supported wavelength in the waveguide with particular width - can be simulated. The cut-off refractive index is $n_{eff} = 1.47$ for half-etched Si_3N_4 waveguides (h − d = $100\,nm$). As can be seen from an example in Fig. 3.2a, a $600\,nm$ wide and $200\,nm$ half-etched waveguide supports a single mode at $850\,nm$ wavelength, while a waveguide width of $\sim 410\,nm$ is the minimal width, hence, no mode is supported in a narrower waveguide. In Fig. 3.2b, all guided modes in a half-etched waveguide with a constant width of $600\,nm$ are shown. Waveguides featuring widths of 500–700 nm for the visible and 800–1150 nm for NIR ranges were fabricated. Most of the time, however, a width of $600\,nm$ was chosen for the devices in the wavelength range $\leq 1000\,nm$.

The large gap between the electrode and waveguide is required to assure that the transmitted mode is not significantly affected by the presence of metal. Considering the short SWCNT length of only $l_{SWCNT} = 1–1.5\,\mu m$, a distance of 1–1.2 μm between two electrodes is sufficient for SWCNT deposition, while a gap of 200–300 nm is ensured if the waveguide width is $600\,nm$ (for visible wavelength range). For the NIR regime, a waveguide width of at least $800\,nm$ has to be chosen to support guiding of light. Hence the gap is only 100–200 nm short for the above mentioned distance between the electrodes.

The ends of all waveguides are terminated with Bragg grating couplers (GC) [85], which allow for coupling light out of the waveguides into the far-field, enabling detection with
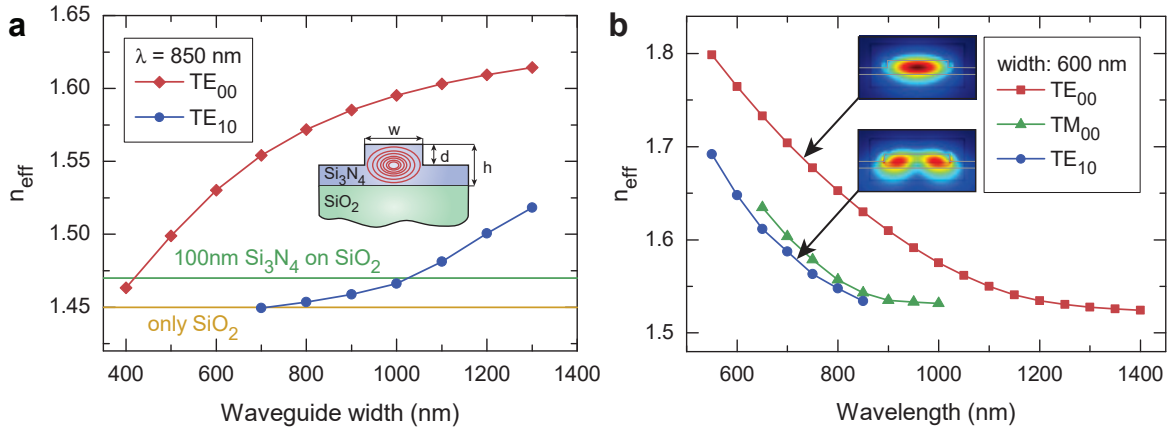
Figure 3.2: Simulation (COMSOL) of the effective refractive index n_{eff} of half-etched Si_3N_4 waveguides. (a) Effective refractive index of the waveguides of various widths calculated for a wavelength of $850\,\text{nm}$. Light cannot propagate below the cut-off refractive index $n_{\text{eff}} = 1.47$ (indicated by a green line). Inset: Schematic of the waveguide cross-section with geometry defined by parameters w, h, and d (width, height, and depth). (b) TE and TM modes supported in a $600\,\text{nm}$ waveguide, half-etched into $200\,\text{nm}$ of Si_3N_4 layer presented in the relevant wavelength range. The electric field intensity $\overrightarrow{E}^2$ distribution for TE_{00} and TE_{01} modes at $\lambda = 700\,\text{nm}$ and $w = 600\,\text{nm}$ are shown as insets.

external detectors. Coupling of light from external sources into the chip plane for spectral device characterization is also provided by the grating couplers. Since the grating period defines the central coupling wavelength and the bandwidth is only about $30\,\text{nm}$, variation of the period on chip is needed to compensate for the fabrication uncertainty (during lithography or etching) and to cover a broader spectral range. The grating period was varied in the range of 400–$700\,\text{nm}$ or 1–$1.4\,\mu\text{m}$ with a fill factor of 0.7 or 0.55 for visible and IR range, respectively.

3.1.1 Mode absorption by metallic contacts

Close proximity of metal can lead to absorption and scattering of the traveling mode in waveguides. The influence of the distance between a waveguide and the metallic contacts, as well as the waveguide's geometry, was investigated. Three different geometries were realized for the NIR range around the telecom-band (since this range is most interesting, because the basic transition E_{11} of sc-SWCNTs lies in the NIR) and compared to find the best approach for minimized attenuation: Rectangular contacts, typically used for SWCNT deposition and allowing for deposition of the SWCNT-films[42], have the strongest impact, due to their longer absorbing path along the waveguide. Round contacts have the advantage of reduced absorption compared to the rectangular shaped contacts, owing to variable gap size. At the same time, at the point of closest proximity the gap is small enough to allow the deposition of short single SWCNTs or films. The third geometry was obtained by dividing a contact into several thin contact teeth (here $200\,\text{nm}$ tip diameter) with round ends. This allows the deposition of several single SWCNTs at each contact pair (at suitable deposition parameters),

while low attenuation can be assured. The optical transmission spectra through a waveguide designed for NIR range (with a constant width of 800 nm along the waveguide) are shown in Fig. 3.3b,c. As can be seen, the wave-guiding mode is attenuated stronger by rectangular contacts at the same conditions (gap size and waveguide width). A series of devices with rectangular contact shape of different widths (w) was fabricated. The results depicted in Fig. 3.3c,d show that, as expected, transmission reduces with decreasing gap (for a particular contact width w) and increases for wider contacts. However, above a certain gap size, the width dependency of the transmission vanishes. This confirms the assumption, that thin contacts show the minimal attenuation of the optical transmission. Therefore this geometry was always used for our device layout, when only several SWCNTs had to be deposited. If dense SWCNT-films are needed, the round contacts are suitable. Additionally, the waveguides for NIR are tapered in-between the contacts (to the width of 800 nm) and are wider everywhere else (1000–1200 nm). Tapering was employed to minimize both the propagation losses along the waveguide, which are bigger for narrower width at a certain wavelength, and attenuation due to proximity of metallic contacts. In case of waveguides for the visible range (with a width of 600 nm), a minimal gap size of 250 nm was used, and the optical mode does not seem to be affected by thin contacts, since the maximal transmission deviations are within the range of measurement error (the data are not shown here). Therefore, for visible wavelengths no tapering was needed.
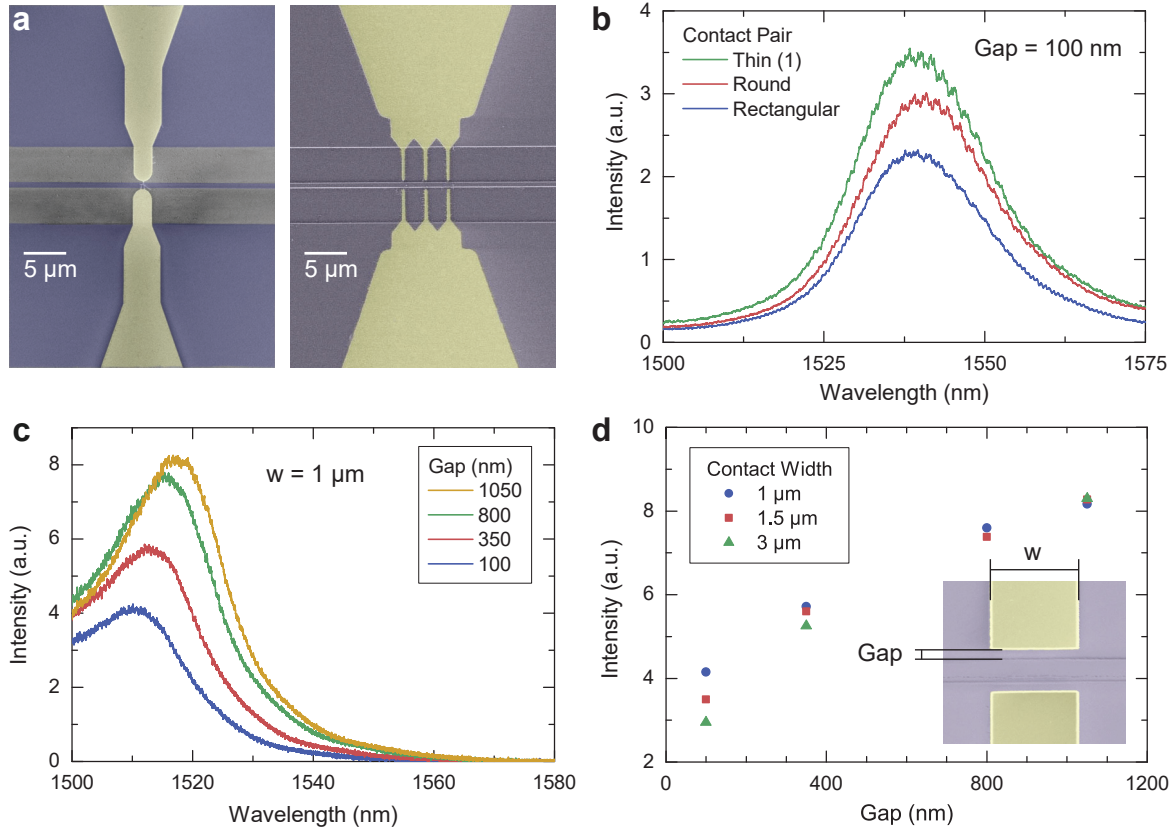
Figure 3.3: Contact proximity impact on the optical transmission in waveguides. (a) Colored SEM pictures of different contact geometries. (b) Transmission spectra in $800\,\mathrm{nm}$-wide waveguides of different shapes with a gap of $100\,\mathrm{nm}$ between the waveguide and the closest contact point. (c) Transmission spectra in similar waveguides. The gap between the rectangular contacts is varied in the range of 0.1–$1\,\mu\mathrm{m}$, with a contact width $w = 1\,\mu\mathrm{m}$. (d) Maximal transmission intensity for different gaps and contact widths w for rectangular geometry, including the data in (c). Inset: SEM picture of rectangular contacts and a waveguide in-between.

3.2 Device fabrication techniques

3.2.1 Fabrication of integrated nanocircuits

In order to fabricate a scalable array of photonic circuits with integrated detectors and sources, a well-established silicon-based fabrication technique was implemented. This technique allows to realize hundreds of nanophotonic devices in a single run, applying several fabrication steps. The integrated photonic devices were fabricated on commercially available silicon nitride-on-insulator wafers, consisting of a layer of buried silicon dioxide (SiO_2) and silicon nitride (Si_3N_4) on top, prepared by low pressure chemical vapor deposition (LPCVD). The substrates have been manufactured elsewhere and were used as delivered.

Samples for the antibunching experiments (described in chapter 5) required an additional fabrication step for the realization of the integrated detectors made of niobium nitride (NbN)

nanowires. Thus, a $4 \pm 0.5\,\mathrm{nm}$ thick superconducting film of NbN was deposited on top of the Si$_3$N$_4$ layer by a collaborating group at Moscow State Pedagogical University (MSPU). For this purpose, high homogeneity DC magnetron sputtering in a nitrogen and argon atmosphere was applied. The deposited superconducting layer was characterized subsequently to determine the surface resistance ($R_s = 336\,\Omega/\mathrm{sq}$) and critical temperature ($\mathrm{T}_C = 10.7\,\mathrm{K}$) [89].

Upon delivery, we diced the wafer into pieces of $15 \times 15\,\mathrm{mm}^2$, which was necessary for lithography structuring. To remove organic residues prior to each lithography step, the samples were cleaned by rinsing or ultrasonication in acetone followed by cleaning in isopropanol. After that, the samples were dried on a hot plate to evaporate the remaining water. For the NbN-coated samples, temperature and heating time were reduced, as the properties of NbN are altered by exposure to high temperature for a long time. The fabrication steps are schematically depicted in Fig 3.4, where the utilized materials are represented by different colors. In the first step (Fig 3.4a), the contact electrodes with alignment markers were defined in positive resist (PMMA, 4.5%) on top of the substrate by means of electron beam lithography (EBL, Raith eLINE or Jeol 5500) and developed for 15 minutes in MIBK:ISO (1:3). After the deposition of $100\,\mathrm{nm}$ gold with a $5\,\mathrm{nm}$ chromium adhesion layer, lift-off in acetone was performed. During the next step (Fig 3.4b), the gold markers were utilized for global and local alignment during EBL. Meander structures made of NbN were defined via EBL in HSQ 6% in MIBK resist, with preliminary evaporated SiO$_2$ as an adhesion layer, and subsequent reactive ion etching (RIE) with CF$_4$ plasma. In the third step (Fig 3.4c), photonic structures were defined in negative resist (ma-N), developed in MF-319 for 1 minute and etched into the Si$_3$N$_4$ layer with RIE in CHF$_3$ atmosphere. Using the gold markers as
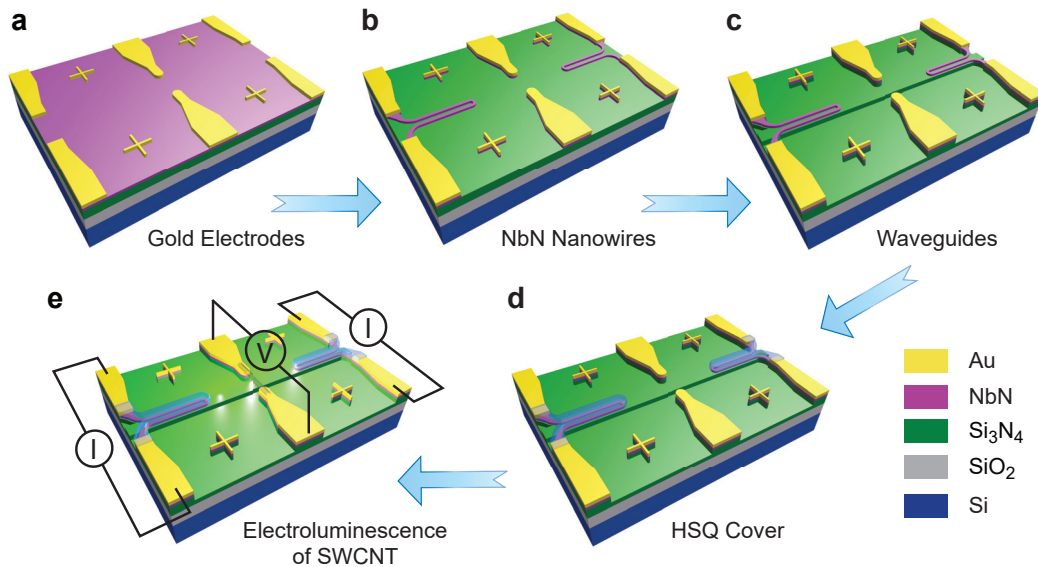

Figure 3.4: A schematic illustration of e-beam lithography steps for device fabrication, shown here for the samples of the antibunching experiments. The arrows indicate the step order. Gold electrodes, NbN nanowires and waveguides are realized in separate processes. *Source: supplementary material to* [57].

local position reference, the waveguides were precisely aligned between the gold electrodes. The waveguides were typically rib-shaped, as mentioned above. Next, the detectors were covered with a 15 % HSQ protective layer (Fig 3.4d) in order to suppress oxidation of the NbN layer during the subsequent SWCNT deposition process. Also the accidental deposition of SWCNTs on the metallic NbN nanowires, which would lead to a conductive shunt and suppression of the detection efficiency, is avoided. The last step was the SWCNT deposition, described below. When a direct or RF voltage is applied to the center contact pair, the source starts to emit light (Fig 3.4e). In case of antibunching experiments, a constant current is applied to the side contacts for allowing the detection of this light (chapter 5).

The fabrication procedure described above was utilized to prepare samples for detection of non-classical light emission from a SWCNT-based source. In other experiments, the procedure was limited to fabrication of metallic contacts and photonic circuits followed by SWCNT deposition (Fig 3.4a,c,e). Extended details of the fabrication steps, such as specific recipes and utilized setups, can be found in the appendix to this thesis. These wafer-scale fabrication techniques are suitable for production of large arrays of devices on a single chip (Fig. 3.5). A scalable SWCNT deposition process is the concluding step of the chip preparation.

3.2.2 Carbon nanotube suspensions

An optimal suspension for our purpose contains only semiconducting SWCNTs (sc-SWCNTs) with a certain chirality and diameter to ensure emission within a small wavelength range. Tuning of this range is possible by carefully presorting of the bulk SWCNTs, typically synthesized by high-pressure carbon dioxide (HiPco) decomposition. Such sorting is prepared by sonication of dispersed in water or toluene nanotubes with addition of 1% dodecyl sulfate or polymer respectively, using a tip sonicator, and subsequent centrifugation for several hours. of as-synthesized suspensions and subsequent separation using size-exclusion gel filtration of suspensions [90,91]. These sorting techniques allow to have control over the spectral properties of the fabricated light emitter. Broad-band thermal incandescent emission or narrow-band electroluminescent sources can be selected by preparing the solutions either with high content
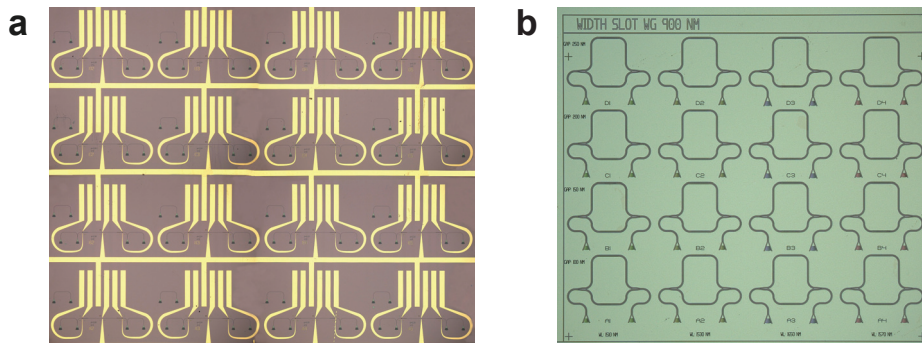
Figure 3.5: Optical pictures of two different samples illustrate a scalable array of devices. (a) A sample used in a cryogenic measurement with gold electrodes. (b) Array of Mach-Zehnder resonators. The grating coupler and beam splitter parameters are varied along the chip.

of metallic SWCNTs or based on dispersions consisting of semiconducting nanotubes with only few chiralities [92,93]. For incandescent sources (which can be also realized with sc-SWCNTs at high electrical power range), the presorting remains important, since it allows to control the quality and concentration of the deposited SWCNTs and the device's electrical properties, albeit the potential electroluminescence spectrum is less important in this case. We utilized different SWCNT dispersions in our experiments. Examples of absorption spectra are shown in Fig. 3.6 (the chiral numbers (n,m) are denoted in the figure). The first kind of suspensions contains only chiral semiconducting nanotubes with 0.9-1.4 nm diameter (blue and red line). These suspensions were prepared in a toluene solution, and depending on the fraction of the centrifugation, consist of SWCNTs with smaller (blue) or larger [42] (red) diameter and only few different chiralities. The water-based suspension contains metallic SWCNTs (green). This suspension was used in an ultra-fast emission experiment (chapter 4) and for comparison of electroluminescent emission of semiconducting SWCNTs with thermal emission in an antibunching experiment (chapter 5).

Another sorting method including a highly concentrated surfactant is described in Ref. [41]. The mono-chiral suspensions are sorted by this method from pristine HiPco material, which allows for large-scale chirality separation. The sc-SWCNTs are coated with a high-concentration surfactant (sodium dodecyl sulfate, SDS), minimizing the interactions (Van-der-Vaals and hydrophobic) with the gel, in which the nanotubes are dispersed. The coverage of single nanotubes with SDS is chirality- and curvature-depended and therefore changes its interaction with the gel (proportionally to the degree of coverage). As a sign of their mono-chirality population, sorted suspensions feature distinguishable colors (Fig. 3.7a), whereas the remaining unsorted and metallic mixtures have a dark-brown color. The photoluminescence emission-excitation map (Fig. 3.7b) allows for designation of the (n,m) indices of semiconducting nanotubes, and hence for determination of the composition of the particular suspension. Here, only four single-chirality PL maps, measured in suspension, are presented. The SWCNTs of
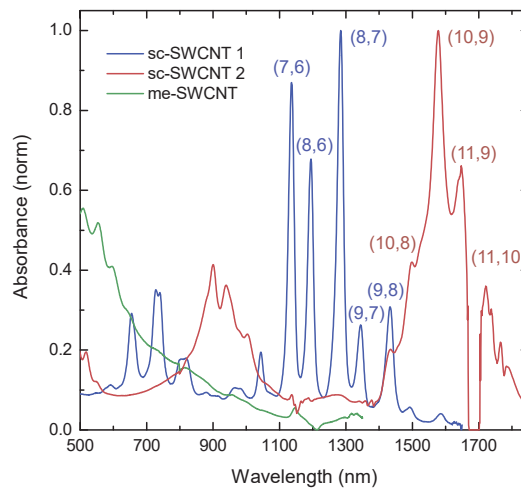
Figure 3.6: Optical absorption spectra of metallic (green) and sc-SWCNT suspensions with small (blue) and big (red) diameter. *Prepared and measured by F. Hennrich (INT, KIT).*
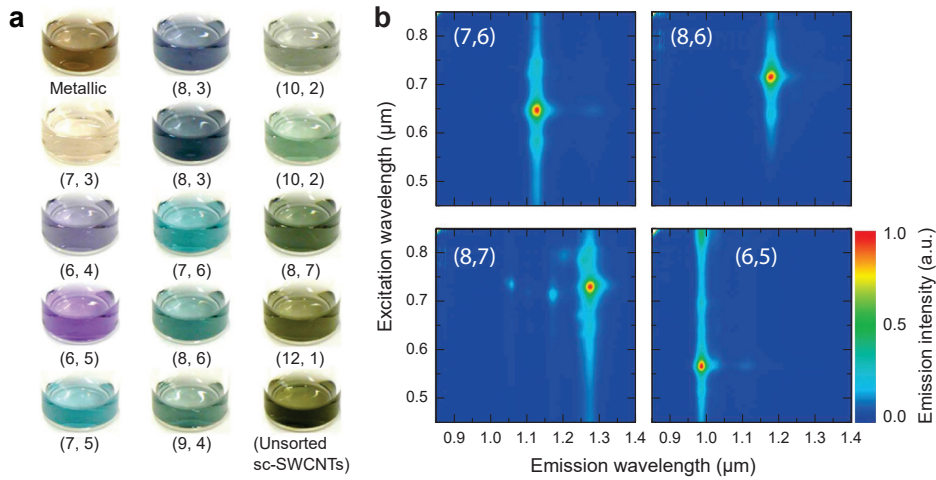
Figure 3.7: (a) Photographs of a broad range of highly sorted SWCNT suspensions with various chirality, clearly distinguishable by their color. (b) Photoluminescence contour maps of four chirality-sorted suspensions, the chirality (n,m) indices are indicated. *Source: adapted from Ref.* [41].

these chiralities are mainly used in our experiment. Sorting of carbon nanotubes is the key technology for wafer-scale fabrication of high uniformity SWCNT-based sources with narrow spectral lines.

3.2.3 Dielectrophoresis of SWCNTs and transport characteristics

After preparation of the sorted suspension, carbon nanotubes were deposited on the array of devices by AC dielectrophoresis (DEP). This technique allows the scalable and well-controllable fabrication of many SWCNT-sources in one deposition step [42,43,94]. For this purpose, each SWCNT source was designed with a common ground electrode on chip, with the second electrode floating (Fig. 3.8a). The nanotubes were forced to precise alignment along a field gradient [96] and placed in-between the adjacent metallic contact pairs. The SWCNT-suspension, containing presorted nanotubes in a high concentration, is diluted in proportion of 1:10 or 1:100 with deionized water or toluene as a solver prior to deposition. This allows a better control over the deposited nanotube densities. Subsequently, this diluted solution was ultrasonicated for 5 minutes in order to separate the nanotube bundles. Afterwards, 20 µl of the suspension was dropped on the chip. An AC electric field with a typically amplitude in the range of 1–10 V_{p-p} and frequency of 1–10 MHz was applied between the common electrode and the silicon gate (Fig. 3.8b) with a function generator (Agilent, SRS DS345). A sinusoidal function with constant amplitude and frequency was used over the entire deposition period. After 5 minutes the sample was rinsed with a solver, suitable for the suspension (water and subsequently methanol, or toluene) and the field was turned off. To improve the contact adhesion, all samples were annealed at 150 °C for 2 minutes on a hotplate (the samples containing NbN) or for 2 hours in an oven (all other samples). The deposition parameters - amplitude, frequency, and duration as well as concentration of nanotubes - were varied to gain either individual SWCNTs or films to be deposited.
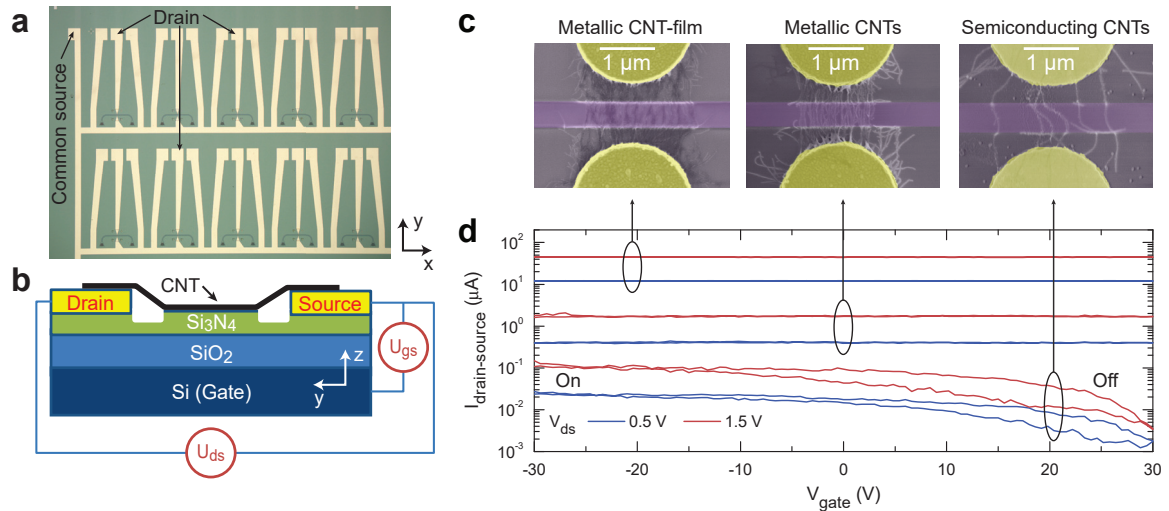
Figure 3.8: Transport characteristics of SWCNT-based devices. (a) Optical picture of a chip layout. All devices in the array have a common source for scalable deposition of SWCNTs. (b) Illustration of the sample's cross-section perpendicular to the waveguide. Si gate and common source are connected either to a function generator for deposition or to a constant voltage source for electrical characterization. The SWCNT device is biased by a source-drain voltage V_{SD} for light generation. (c) SEM micrographs of single SWCNTs and a dense film deposited between the gold electrodes on top of the waveguide. The density of nanotubes is approximately $100\,\mu m^{-1}$ in metallic films (left), $\sim 10\,\mu m^{-1}$ in single metallic SWCNT (center), and $\sim 3\,\mu m^{-1}$ for single sc-SWCNTs. (d) The respective gate dependence of the source-drain current (measured at constant source-drain voltage $0.5\,V$ and $1.5\,V$) reveals a different behavior for metallic and semiconducting devices. On-off ratios of ~ 50 and typical hysteresis are clearly seen in sc-SWCNT devices, while high currents (1–$50\,\mu A$) are observed in metallic SWCNTs. *Source: (a) is adapted from* [95].

After the deposition, the transport characteristics of the devices were measured in order to select the structures with individual semiconducting or metallic SWCNTs, depending on the application. The SWCNT-based device is connected to three electrodes - source, drain, and gate, like a field-effect transistor (CNT-FET, Fig. 3.8b). A p-doped silicon substrate plays the role of the gate electrode. Here, the common electrode is referred to as source and the floating electrode as drain. Thus, the SWCNT is in direct contact with the source and drain, while it is isolated from the gate due to a thick SiO_2 dielectric layer. To characterize the SWCNT-based device properties, the gate voltage was swept in a wide range ($-30\,V$ to $30\,V$) forwards and backwards for three constant values of the source-drain voltageV_{SD}, which was kept relatively low (1–$3\,V$). An important characteristic of a FET is its on-off ratio (I_{on}/I_{off}). It is equal to one for metallic SWCNTs, while for sc-SWCNT it can achieve several orders of magnitude. In Fig. 3.8c,d SEM pictures and respective transport characteristic of three devices with different densities of SWCNTs per unit length are presented: dense metallic films, several metallic and sc-SWCNTs on top of the waveguide. The linear density varies from $\sim 100\,\mu m^{-1}$ to $\sim 3\,\mu m^{-1}$. In case of semiconducting SWCNT, a strong impact of the gate is observed, despite a relatively thick silicon dioxide layer (Fig. 3.8d, lowest set). The

source-drain current decreases with increasing gate voltage, hence, an off-state at positive gate voltages was observed. The on-off ratio reaches three orders of magnitude (100–1000) with an on-current $I_{-30\,V}$ of about tenths of nanoamperes (nA) and an off-current $I_{30\,V}$ in the femtoampere (fA) range. For metallic single SWCNTs and films, the source-drain current remains constant with the gate voltage (Fig. 3.8d, top and middle sets). Devices containing metallic SWCNTs can be distinguished by a relatively high current: $I_{SD} \sim$ µA for single me-SWCNT, while hundreds of µA can be achieved in metallic films with higher density. This is also true for devices with mixed SWCNTs. In case of sc-SWCNT devices in the on-state, the current reaches $1 - 100\,$nA. The extracted current densities for the presented metallic and semiconducting devices with several SWCNTs are $\sim 10^6 \frac{A}{cm^2}$ and $\sim 10^4 \frac{A}{cm^2}$, respectively, which is lower as for graphene nanoribbons ($\sim 10^8 \frac{A}{cm^2}$)[97], but still is remarkable in comparison to bulk materials ($\sim 310 \frac{A}{cm^2}$ for copper). The hysteresis arising because of trapped charges in the dielectric[98,99] can be clearly seen for the sc-SWCNT device (Fig. 3.8d, lowest set). High current density in single metallic SWCNTs is evidence for ballistic transport in the one-dimensional tubes [71,100].

SWCNT-based light emitters containing a SWCNT on top of the planar waveguide were presented. The device geometry, such as waveguide width at a given height and wavelength and also the distance between the metallic contacts were optimized for guiding of the optical mode. The well-established fabrication techniques of integrated circuits, continuous progress in sorting methods of sc-SWCNT suspensions, and dielectrophoretical deposition of the SWCNT between contact pairs together allow for the scalable realization of hybrid devices. Suspensions containing purely semiconducting nanotubes of few chiralities with a negligible part of metallic nanotube were characterized by absorption and emission spectroscopy prior to deposition. The devices are designed with field-effect transistor geometry with silicon substrate as the gate electrode. After the deposition, transport characteristics through all devices were measured. Devices with suitable characteristics (for example, source-drain current, on-off ratio) were selected.

The sorted SWCNT suspensions were prepared by Dr. B. S. Flavel and Dr. F. Hennrich from the group of Prof. Kappes and deposited by Felix Pyatkov from the group of Prof. Ralph Krupke at INT.

4 SWCNTs as classical light source

In this chapter the integration of SWCNT as an active component into photonic circuits with various linear optical components, such as planar extended waveguides, directional couplers and Mach-Zehnder interferometers, is shown. Such hybrid devices with a SWCNT as an active component of the otherwise passive circuit is a first step towards carbon based optical interconnects. The experimental setups, used for characterization and measurements, are briefly described. The evanescent coupling efficiency of SWCNT-light into a waveguide and propagating loss is estimated. We present the integration of a carbon nanotube in a photonic cavity for tunable narrow-band emission. In the second part the application of nanotubes as a high-speed electro-optical transducer is discussed. A conversion into an optical pulse sequence with up to 2 GHz frequency is shown. A minimal decay time of 80 ps for pulsed incandescence is measured.
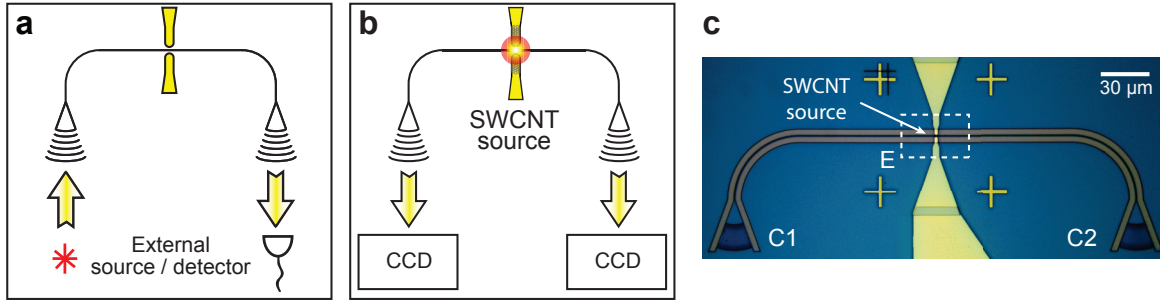
4.1 Fiber-coupled and free-space setups

Two setups were implemented for the characterization of the waveguide-coupled SWCNT-devices and to carry out the experiments. The fiber-coupled setup (Fig. 4.1a) allows the measurement of the transmission through the devices with an external light source and detector, as well as time resolved measurement of ultrafast incandescence produced by waveguide-coupled SWCNTs. In the free-space setup the light from the internal SWCNT-source, emitted directly or coupled to a waveguide, was spatially and spectrally resolved and recorded (Fig. 4.1b). The measurement configurations with external and internal source are schematically depicted in Fig. 4.2. Prior to the SWCNT deposition all samples were characterized using a fiber-coupled setup. The light from an external supercontinuum source (1) (Fig. 4.1, a) is coupled from a fiber array assembly (2) into the chip at the grating coupler, propagated inside of device and coupled out into the far-field, where it can be collected by a fiber in the fiber assembly. The light is detected with a fiber-coupled spectrometer (3). The sample was mounted on a PC-controlled 4-axis piezo stage (x, y, rotation and tilt) and aligned to a fiber array using a CCD camera (4) followed by optimization of the position with respect to the transmitted signal. The distance between two adjacent fibers in the fiber array assembly (2) is 250 μm, hence, the device layout has to be adjusted to this value and the distance between thecouplers C_1 and C_2 has to be a multiple of 250 μm. The optical fiber located above the grating coupler has a core diameter of ~ 8 μm which is smaller than the grating coupler size (for NIR range about 35–40 μm). The position of the fiber and its tilt angle have a great influence on the coupling efficiency and central wavelength of the Gauss-shaped transmission spectra. The sample can be mounted inside of a vacuum chamber (10^{-5}–10^{-7} mbar) equipped with optical and electrical feed-throughs and suited for the above
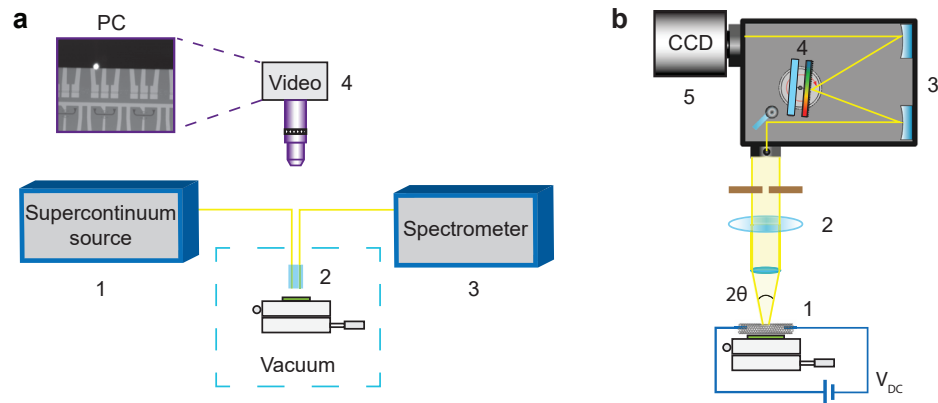
Figure 4.1: Schematic illustrations of the fiber-coupled (a) and free-space (b) measurement setups. First, coarse alignment with an optical camera (4) is made, then transmission optimization and measurement with external supercontinuum source and spectrometer is performed. The sample in (a) also can be analyzed in a vacuum chamber. The SWCNT emission can be measured spatially and spectrally resolved, by using a mirror or a diffraction grating (4), respectively. Data is recorded with a low noise CCD camera. *Source: adapted from supplementary to [35].*

mentioned measurement. The vacuum configuration is utilized during the measurements of pulsed emission of SWCNT-based devices.

The free-space measurement setup (Fig. 4.1b) is used to record spatially resolved emission pictures of the device, but also for spectral characterization of SWCNT-light in the far-field. To reduce the diffuse light background the sample is measured in a light-tight cabinet. The sample is mounted on a motorized stage (1), and the SWCNT device under test is electrically connected through probe needles. The electrically induced light emission is collected with an optical microscope (2), reflected inside of a directly attached spectrometer (3) and coupled into a high-sensitivity electrically cooled low noise 2D CCD camera (5). One of the camera's dimensions is used either for space resolution, then the collected light is reflected by a mirror inside of a spectrometer, or for spectral resolution, thus instead of a mirror a diffraction grating is used (4). The light from the chip is collected from a solid angle depending on the field aperture of the microscope objective, typically less than 44°.

Figure 4.2: Measurement configuration for fiber-coupled measurements, employing an external laser source and detector (a) and free-space measurements with internal SWCNT-based source with external CCD-detector (b). (c) Optical picture of a typical device with grating couplers (C_1 and C_2) for coupling into a far-field and internal near-field SWCNT-emitter (E). *Source: adapted from supplementary to* [35].

## 4.2 Integration of SWCNTs into nanophotonic structures

The unique properties of sc-SWCNTs as a room-temperature telecom-band emitter, with a band gap inversely proportional to the nanotube's diameter, establish them as a promising component for integrated optics and nanophotonics. Carbon nanotubes have recently been efficiently integrated into nanophotonic structures, such as a waveguide [101], microdisc [102] and photonic crystal cavities [33], and, hence, implemented as on-chip nanoscale photoluminescent emitter under constant and pulsed optical bias. In these studies, a free-space laser was utilized for excitation of single SWCNTs and fluorescent emission was coupled into photonic structures. However, electrical biasing of carbon nanotubes is a more preferable and scalable approach, because no additional excitation source is required. Since electrically induced emission from carbon nanotubes was first explored from Misewich et al [36], new avenues for integrated nano-scale SWCNT-based sources have opened up. The advantage of the direct band gap of semiconducting SWCNTs and support of both, n- and p-type conductivity facilitate the successive establishment of carbon nanotubes as optical emitters. Efficient carrier transport through carbon nanotubes make them ideal for low energy consuming carbon-based optoelectronic and photonic devices.

Site-selective placement of pre-sorted SWCNTs directly on the contacts, ensured by dielectrophoretic force, allows for chip-scale realization of a large number of sources in one fabrication run and later separately addressing them electrically. Multiple emitters can be placed on the same waveguide structure (Fig. 4.3) in order to enhance the emission intensity, roughly proportional to the number of sources. At the same time it can be assured, that each contact pair contain only one or few SWCNTs. This is important for better performance, since the electrical current and temperature of the SWCNTs are affected by its film density. For example, bundled SWCNTs conduct reduced current compared to the same number of parallel connected single SWCNTs. Furthermore, bundled SWCNTs have a lower break-down voltage. For single-photon generation, discussed in the next chapter, only a single sc-SWCNT nanotube in-between the single contact-pair is required. To take advantage of the wavalength-dependent electroluminescence of sc-SWCNT, it must be ensured that no metallic SWCNT

were deposited on the same contact pair. Otherwise, the electrical and optical properties of such sources would be governed by the metallic SWCNT with much higher currents compared to semiconducting nanotubes. The SWCNT-based devices, presented in the following chapter, are described as emitters of classical light. The CCD-detector used in the free-space setup is only sensitive to light in the spectral range of $\sim 400\text{--}1100\,\mathrm{nm}$. Therefore, the origin of the emission is mostly of thermal ("incandescent") nature, whose intensity dominates over electroluminescence of sc-SWCNTs in this spectral range. Because the main transition (E_{11}) of sc-SWCNTs and, hence, the brightest line (λ_{11}) in the spectrum, is mostly in the NIR ($\sim 900\text{--}1600\,\mathrm{nm}$ for typical sc-SWCNT in our experiment). Concerning me-SWCNT, only featureless broadband thermal light is expected. Therefore, the chirality of the nanotube, contained in the pre-sorted suspensions, is not specified in this chapter. Upon electrically biasing in the range of $3 - 10\,\mathrm{V}$ (electrical power of $1\text{--}100\,\mu\mathrm{W}$) SWCNTs emit light, which can be seen in a spatially-resolved emission map (Fig. 4.4a) as a clearly distinguishable spot at the position of the SWCNT (E). The background counts are represented in blue. Its size is diffraction-limited (the resolution of the used objectives is given in the Appendix) and increases with the electrical power. The light emitted by the SWCNT (at spot E) is coupled into the underlying waveguide and approximately equally splitted in opposite directions. It propagates over a distance of $150\,\mu\mathrm{m}$ and is diffracted at the grating couplers. Two bright emission spots can be observed in the free-space setup (chap. 4.1) at the grating coupler positions (C_1 and C_2), and no other emission sources are visible along the waveguiding path on this map. This gives evidence that light propagates in the waveguide with no significant losses, which exceed the background illumination and could be observed on this emission map. At the same time, it is known that there are different kinds of losses in a waveguide, for example, absorption, scattering [87], and also bending losses on curvatures of small radius [103] ($= 40\,\mu\mathrm{m}$ in this device).
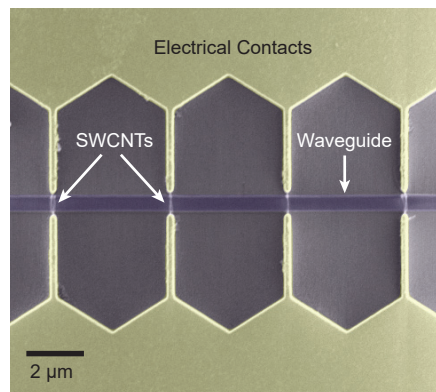
Figure 4.3: Colored SEM picture of electrical contact pairs array (yellow) each containing SWCNTs on top, bridging the waveguide (purple).
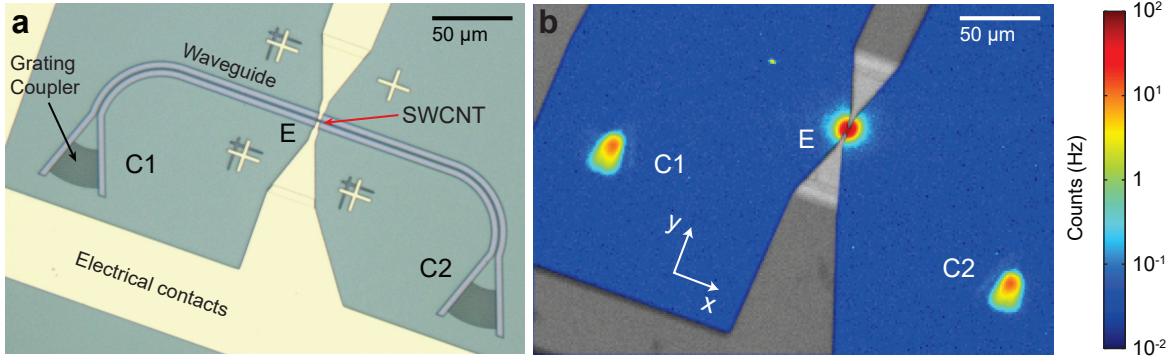
Figure 4.4: Optical picture of standard SWCNT-device with two grating couplers (a) and emission map of similar device (b), recorded with CCD-camera in the free-space setup. Light emitted from SWCNT at E is partly coupled into the waveguide, propagated, and coupled out of the grating couplers (C1 and C2). No emission from the waveguide path (no losses) is seen in (b). *Source: adapted from* [35].

4.2.1 SWCNT emission coupling to the waveguide

SWCNTs produce electroluminescent light, which is linearly polarized along the nanotube's axis [36,104], so they emit most efficiently perpendicular to that axis. The orientation of the SWCNT perpendicular to the waveguide, which is realized in all our devices, takes advantage of this so called "antenna" effect for efficient light coupling into a single mode waveguide. In order to analyze the near-field (evanescent) coupling of the SWCNT-emission into the waveguide structure, a finite-difference time-domain (FDTD) calculation of the electric-field intensity $\bar{E}^2$ was performed [35] using the commercial software package OmniSim, Photon Design [105]. The simulations were carried out in three dimensions using a high grid resolution to ensure convergence within a 5 % error margin. The SWCNT emitter was modeled as an elongated electrical dipole source with dimensions corresponding to the real nanotube emitter. It is placed in direct contact with the top surface of the waveguide and oscillates perpendicular to the xz-plane. To obtain traveling wave modal distributions (shown in Fig. 4.5), the calculation was performed for continuous-wave excitation. The light of the dipole is coupled into the near-field and propagates within the waveguide. It can also be seen that part of the emitted light is far-field-coupled into and out of the substrate plane along the surface normal. The light back-scattered from the substrate interferes with the light emitted directly from the source. The interference fringes shape the spectral profile of the emitted light, coupled into the waveguide as well as directly into the far-field. These interference spectra can be analyzed in the free-space setup, as will be explained later (Fig. 4.7).

The coupling efficiency of SWCNT-emitted light into the waveguide is estimated experimentally. For this purpose, several waveguide structures, terminated with two grating couplers, are studied in the free-space setup. The SWCNT-source was designed to be close to one of the grating couplers. The electrically induced thermal light is collected with a CCD camera directly from the SWCNT-emitter (I_{E}) and after propagation inside the waveguide and coupling out of chip plane into the far-field on the grating coupler (I_{coupled}). On the
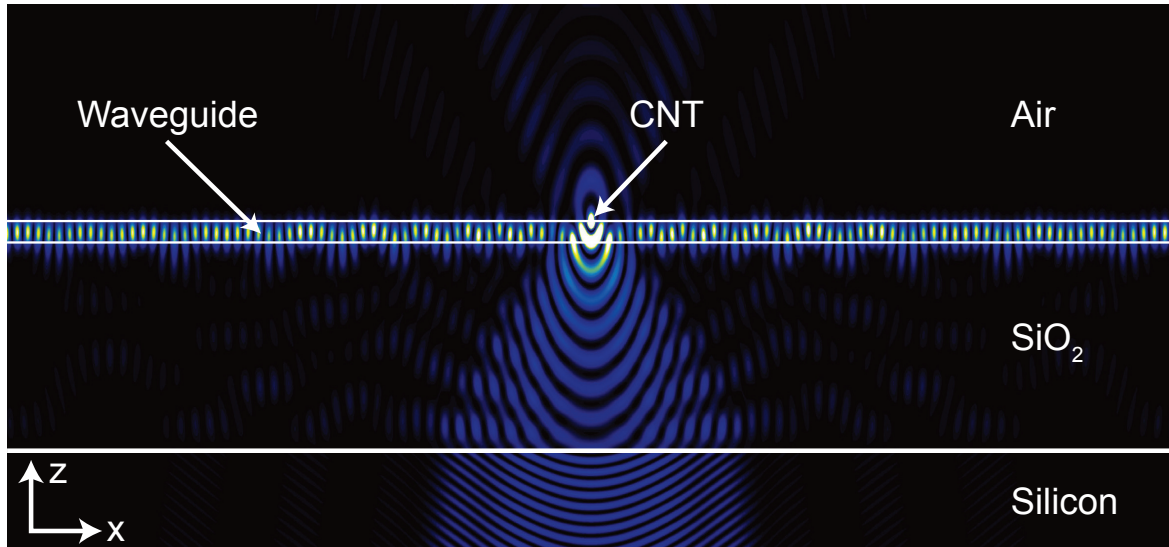
Figure 4.5: Cross-section through a 3D finite-difference time-domain simulation of the electric-field intensity $\bar{E}^2$. The carbon nanotube is simulated as an elongated electrical dipole at the waveguide-air interface, oscillating perpendicular to the x-z-plane. *Source: [35]*.

spatially-resolved emission map (Fig. 4.6a) the light spots of the SWCNT-source directly (E) and of one grating coupler are visible, superimposed with the design layout of the waveguide and contacts for clarity (white lines). Again, no detectable loss in the waveguide is observed (Fig. 4.6a). The resulting coupling efficiency is estimated by comparison of the emission intensities at the source and two grating couplers (I_E and $2 \cdot I_{coupled}$, respectively), measured with the external detector. This was performed according to equation $\jmath_{coupling} = \frac{2 \cdot I_{coupled}}{I_E + 2 \cdot I_{coupled}}$, where $I_E + 2 \cdot I_{coupled}$ is the total emission (approximately) and $2 \cdot I_{coupled}$ is the "usefull" part of the emission, coupled into the waveguide and propagated to the couplers. Both intensities, I_E and $I_{coupled}$, are integrated over equal areas. Here, two other assumptions were made: propagation loss in the $25\,\mu m$ short waveguide between the source and grating coupler as well as the coupling losses due to coupling along the surface normal are assumed to be small and therefore negligible (in contradiction to coupling out at the designed angle of $8°$). In our estimation these two sources of loss are unavoidably included in the coupling efficiency $\jmath_{coupling}$. Due to this approach, the lower boundary of the coupling efficiency is estimated by given equation. In Fig. 4.6b the intensity at the grating couplers is plotted versus the total intensity on both grating couplers and the emitter. The linear fit to the data (red line), measured with the same device at different DC-bias, yields averaged coupling efficiency of $44 \pm 2.5\,\%$ for this device. In Fig. 4.6c the coupling efficiency, calculated for each data point from (b), versus I_E is depicted, revealing a maximal value of $\jmath_{coupling}$ larger than $60\,\%$. The same high value is also calculated for several devices for spectrally resolved incandescent SWCNT-emission in the complete detectable spectral range, showing no spectral dependency of the coupling efficiency $\jmath_{coupling}$ [57]. These estimated values are consistent with those reported in the literature for waveguide-integrated sources [106,107], manifesting the
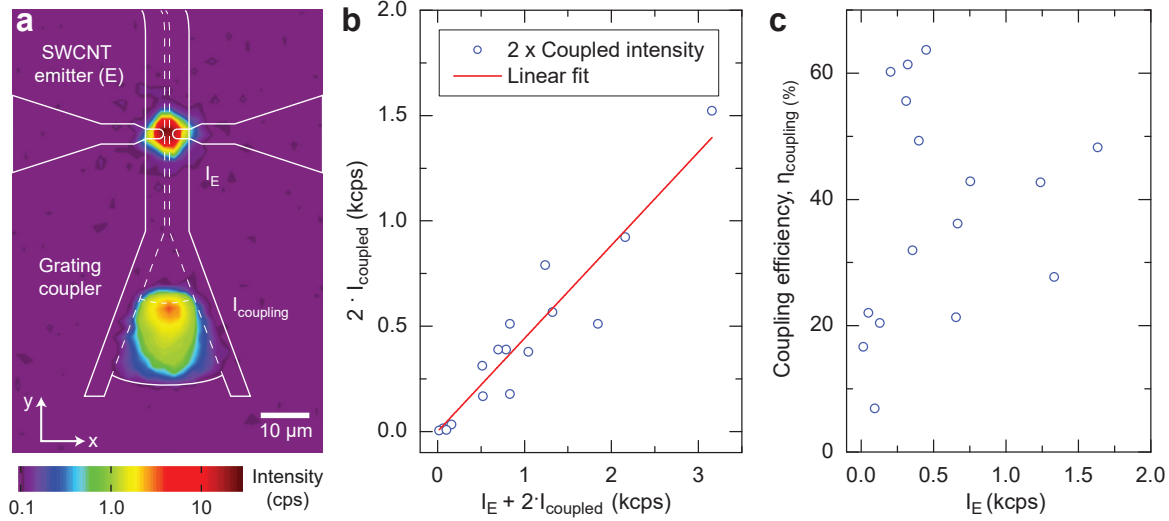
Figure 4.6: Estimation of coupling efficiency ($\jmath_{coupling}$) of the SWCNT-emitted light into the waveguide. (a) Spatially resolved emission directly above the SWCNT (I_E) and after the diffraction on a grating coupler ($I_{coupled}$). White lines depict the device layout with contacts, waveguide and grating coupler position (in positive tone resist). The color scale is intensity in arbitrary units. (b) The intensity on the grating couplers versus total intensity (blue circles), measured on the same device at different DC-biasing conditions (V_{SD}). The fit to the data (red line) shows the estimated coupling efficiency $\jmath_{coupling} = \frac{2 \cdot I_{coupled}}{I_E + 2 \cdot I_{coupled}}$ for this device of $44 \pm 2.5\,\%$. (c) $\jmath_{coupling}$ estimated for each the presented in (b) data versus direct emission of the source (I_E) with the maximal value of $\jmath_{coupling} = 63\,\%$.

coupling to integrated nanophotonic structures as an efficient process. $\jmath_{coupling}$ can be further increased by placing the SWCNT into a cavity, which acts as an enhancement of a particular coupled mode (for example, a photonic beam cavity [108]).

4.2.2 Electron temperature of incandescent SWCNT emitters

The emission spectra of the SWCNT-sources are recorded with a CCD camera in the free-space setup (chap. 4.1) at the position of the emitter (E) and the couplers. In Fig. 4.7a the emission map of one device is presented, spatially resolved in y-direction and spectrally resolved in the other (x) direction. A device sketch is depicted on the right side to clarify the origin of the emission on the map, where the intensity maxima are clearly visible. In Fig. 4.7b a series of spectra emitted directly at E at various values of the electrical power and integrated over the space component is shown (approximated integration area is depicted by the dashed line in Fig. 4.7a). The intensity increases towards longer wavelengths with several broad peaks [35]. This behavior is observed both for direct emission and for light coupled out of the waveguide at the grating couplers. The SWCNT-light propagated inside the waveguide also demonstrates similar fringes in the spectrum, because the reflected light is also coupled into same waveguide from the SiO_2 substrate side (at the SiO_2/Si_3N_4 interface). This spectral picture differs from a typical narrow-band EL signal, with peaks at
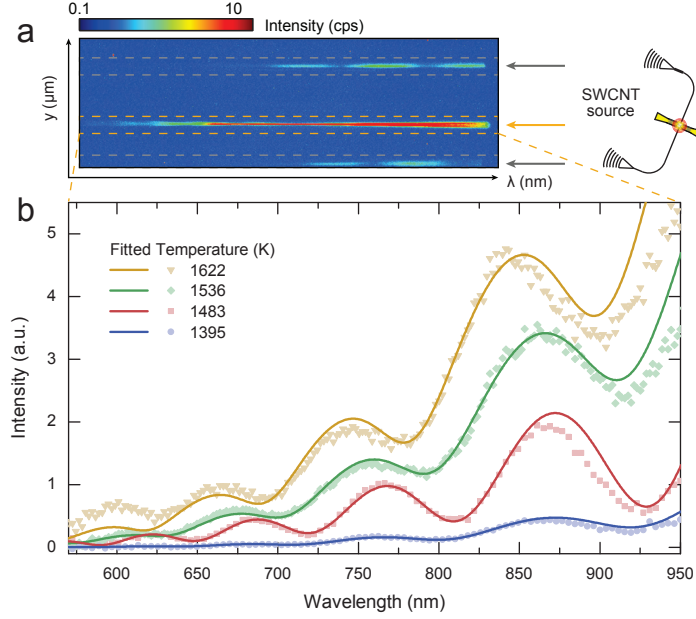
Figure 4.7: Spectrally resolved SWCNT-emission (a) Emission, recorded in the free-space setup at two grating couplers and emitter simultaneously, is spatially resolved in y-direction and spectrally in x-direction. The illustration on the right side show the position of the device under the CCD-camera. The arrows assign the origin of the emission. (b) Emission, integrated over the spatial component, recorded for the devices at different constant bias (symbols) and the best fits to the data (solid lines). *Source: adapted from* [35].

different positions and without overall intensity increase. Therefore, we attribute this spectral dependency to a broad-band black-body radiation, enveloped with intensity modulation due to interference with the reflected light from the Si/SiO$_2$ interface. This is consistent with a fit of these spectra to the function $f(\lambda) \propto f_{\text{Planck}}(\lambda,T) \cdot [a_1 + a_2 \cdot f_{\text{int}}(\lambda)]$, where $f_{\text{Planck}}(\lambda,T)$ is a Planck radiation term, increasing with wavelength and temperature, and $f_{\text{int}}(\lambda)$ is a wavelength-dependent interference term. The ratio $\frac{a_2}{a_1}$ of the coefficients in the interference term reproduces the limited coherence of the light, as explained below. The interference between photons emitted directly into the microscope and photons which are emitted towards the silicon substrate and then reflected back shapes the intensity spectrum, as described by $I(\lambda) = I_1(\lambda) + I_2(\lambda) + 2 \cdot \sqrt{I_1(\lambda) \cdot I_2(\lambda)} \cdot \text{Re}\,(\gamma_{12}(\tau))$ [109]. $\gamma_{12}(\tau)$ is the complex degree of temporal coherence, which is dependent on the time delay between photons emitted directly into the microscope and reflected back, interfering with each other in the focal plane of the objective. This time delay can be calculated as the optical path divided by the speed of light, $\tau = \frac{\triangle l}{c}$, where $\triangle l = 2 \cdot (d_{\text{Si}_3\text{N}_4} \cdot n_{\text{Si}_3\text{N}_4} + d_{\text{SiO}_2} \cdot n_{\text{SiO}_2}) \approx 6.98\,\mu\text{m}$. The visibility

$$\gamma_{12}(\tau) = \int\limits_0^\infty f_{\text{Planck}}(\nu,T) \cdot \exp\,(-2\pi i\nu\tau)\,d\nu$$

of the interference fringes in a spectrum is determined by the magnitude of temporal coherence τ.[110] It varies between a completely incoherent source and a perfectly coherent source: $|\gamma_{12}(\tau)| \in [0,1]$. Hence, the Planck emission spectrum, modulated by the interference term $f_{\text{int}}(\lambda)$, which is decreased by the temporal coherence of a not fully coherent source, describe our data well. The fit function is defined as follows:

$$f(\lambda) \propto f_{\text{Planck}}(\lambda,T) \cdot [1 + 2 \cdot |\gamma_{12}(\tau)| \cdot f_{\text{int}}(\lambda)].$$

By comparison with the equation given above, the following expression can be written: $\gamma_{12}(\tau) = \frac{a_2}{2 \cdot a_1}$. The interference function is calculated with the transfer matrix method, where reflections of the SWCNT-emitted light at the Si_3N_4/SiO_2 and the SiO_2/Si interfaces are taken into account[35]. In this method the interference function is written as $f_{\text{int}}(\lambda) = \text{Re}(r(\lambda) \cdot r^*(\lambda))$, where $r(\lambda) = 1 - k \cdot \text{reflectance}(\lambda)$ and reflectance(λ) is the reflected Fabry-Perot interference term. The coefficient k represents the fraction of light that is streamed into the substrate. The exact form of $f_{\text{int}}(\lambda)$ can not be expressed analytically in one equation, and therefore, is not shown here, but is described detailed in [111]. Additionally to the wavelength, the interference term is dependent on the thicknesses and refractive indices of the chip layers, as well as on the incident angle of the emitted light (assumed to be 0°). The intensity peaks are observed around 670 nm, 740 nm, 800 nm, 850 nm, 900 nm and 950 nm for the presented device with a SiO_2 thickness of 2 μm. The peak positions differ for different SiO_2 thicknesses, while the Si_3N_4 thickness plays a less important role. The temperature, silicon nitride thickness, coefficient k and degree of coherence are extracted from the fit, while the silicon oxide thickness is kept as constant. The non-linear fitting procedure based on the Levenberg-Marquardt algorithm with an initial guess and a upper and lower boundary for each parameter is applied, to ensure realistic fitting values. The fitted value of $|\gamma_{12}(\tau)|$ varies in the range of 0.016–0.025 for the presented temperatures T = 1395–1622 K. This relatively high value for a thermal emitter can be explained by the reduced dimensionality of nanotubes [112,113], as well as, probably, by the limited spectral bandwidth of the CCD detector.

The appearance of a broad-band thermal emission in the spectra instead of narrow-band electroluminescence emission with characteristic wavelength λ_{11} or λ_{22} of the first and second optical transitions can be explained by injection of high current and heating of the nanowure. Additionally, the limited sensitivity of our CCD-detector to the spectral range of $400 - 1100$ nm plays an important role. Here, the thermal emission of the SWCNT at a high-bias overcomes the weak electroluminescent emission of the S_{22} transition (750–850 nm for employed nanotubes with diameter ~ 1 nm), which could potentially be seen in the given detection range. Unfortunately, the S_{11} emission of the sc-SWCNT suspensions used in this experiment is beyond the spectral cut-off of the applied CCD-detector (1100 nm). SWCNT with strong emission at λ_{11} in the visible range have significantly smaller diameters than 1 nm. Thus, the realization of such devices is more complicated due to the sophistication in the sorting and deposition processes. Nevertheless, the sc-SWCNT-induced electroluminescent emission with the characteristic wavelength λ_{11} of the fundamental optical transition S_{11} can be evanescently coupled into the waveguide, similarly to thermal emission. The coupling efficiency of the polarized emission is high, as shown above in the simulation and in the

experiment (subchapter 4.2.1).

For the investigation of electroluminescent emission, several improvements have to be done. To fabricate pure sc-SWCNT devices and to avoid the contribution of metallic SWCNTs to the thermal emission, the devices have to be prepared more carefully out of highly sorted suspensions with low content of metallic nanotubes. A gate voltage can be applied to increase the emission intensity of such devices [36], which therefore can be driven at lower source-drain voltage V_{SD}. Hence, unwanted black-body radiation can be decreased. Also, the overall device temperature can be decreased, which was done in a cryogenic setup performing the second-order correlation measurements (chapter 5). The simplest solution is to employ a detector, suitable for the NIR spectral range, to study the S_{11} optical transition. However, the dark count rate (DCR) of such a detector is usually higher than that of a CCD detector for visible light. Thus, integration over an extended period of time have to be performed with carefully reduction of the scattered background.

4.2.3 Scattering of emission at grating couplers

Here, the spectral behavior of the SWCNT-light coupled out of grating couplers (C_1 and C_2) is studied [35]. In Fig. 4.8a, an emission map of SWCNT-light recorded with a CCD-camera and a high resolution objective in the free-space setup is presented. The colored map has 95% opacity and is superimposed with a SEM image for clarity. Therefore, the end of the taper and the gratings can be seen. After a bias is applied to the SWCNT device, the emission is extended over the whole coupler area, where two regions can be identified. The first one starts close to the taper end, extends over the first several gratings and has a high intensity profile. Here, photons with a wavelength outside of the designed coupler bandwidth are scattered diffusively. The second region extends over the bottom part of the coupler grating. The photons are spectrally filtered by the coupler grating, so their wavelength is inside of the coupler's bandwidth. These photons are Bragg-scattered into the far-field with a designed tilt angle to the chip surface normal of 8°. The fiber assembly of the fiber-coupled setup is optimized for coupling of light which is Bragg-scattered at this particular angle (8°), while the microscope objective of the free-space setup collects the light in a field aperture of $2 \cdot \Theta$ (see Appendix) with respect to the chip surface normal.

Fig. 4.8b shows the SWCNT incandescence emission spectra of the diffusive and Bragg-regions for two devices with different grating periods, and therefore different central wavelength of the Gauss-shaped coupling profile (λ_1 and λ_2). The overall spectral intensity shows similar interference features compared to the spectra recorded directly at the position of the emitter (E). Here, only a part of the spectrum with two interference minima and one maximum is presented. However, a clear difference is observed at the characteristic wavelengths of the grating couplers ($\lambda_1 = 849\,\text{nm}$ and $\lambda_2 = 873\,\text{nm}$, respectively). At these wavelengths, the spectra of the diffusive region show a distinct dip, and the spectra of the Bragg-scattering region show a peak. This is clear evidence that the photons with this wavelength are filtered by the grating and coupled out on its bottom part. Therefore, the spectra recorded in the Bragg-scattering region are much more narrow and defined mostly by these photons. Such narrow-band spectra (FWHM $\sim 30\,\text{nm}$) can regularly be seen in the fiber-coupled setup. In the latter only a small part of the light from the diffusive scattering region can be collected,
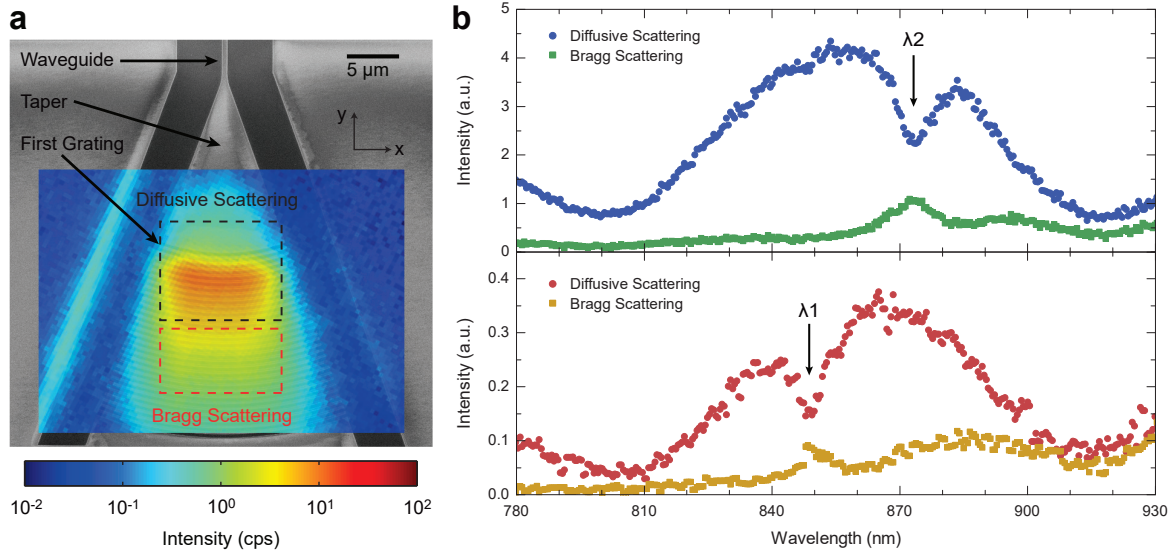
Figure 4.8: Two types of emission are observed in the grating couplers. (a) SEM picture of the grating coupler, superimposed with an emission map of scattered SWCNT-light, recorded in the free-space setup with an objective with $44°$ aperture. Two coupling regimes are defined - diffuse scattering at the taper and first several gratings, and Bragg scattering at the coupler's bottom part. The waveguide, taper and first grating are denoted with arrows. (b) Emission spectra of two devices with different grating periods and, hence, central wavelengths (λ_1 and λ_2). A dip / peak is observed at $\lambda_1 = 849\,\mathrm{nm}$ and $\lambda_2 = 873\,\mathrm{nm}$ respectively. *Source: adapted from* [35].

due to the small field aperture and tilted angle. As a result, a grating structure implemented into a photonic waveguide directly after the SWCNT-source, or a more sophisticated photonic beam cavity [108] can be used for spectral filtering of broadband incandescent light.

4.2.4 Extended waveguides

In potential applications of photonic circuits, optical interconnects will replace the high-speed electrical interconnects for higher performance and faster data transfer. On a wafer-scale, extended single-mode waveguides will replace the electrical wiring to connect the various distant nanocircuit optical components. The propagation losses within the waveguide play a crucial role for future device generations. For on-chip quantum photonic applications implementing single-photon sources, any loss of photons degrades the photon statistics and, hence, decreases the fidelity of the operation. We have demonstrated, that the light coupled from an electrically driven SWCNT-source propagates within extended waveguides and have determined the propagation losses, which results in the attenuation of the emission [35]. For this purpose, a series of waveguides with different lengths (Fig. 4.9) and asymmetric distance between the emitter (E) and the two couplers (C_1 and C_2) were prepared. The first distance (d_{E-C1}) was kept constant ($25\,\mu m$), while the second distance (d_{E-C2}) was varied systematically between $3.6\,mm$ and $10.1\,mm$ (thus $d_{E-C1} < d_{E-C2}$). The waveguides were designed with several bends, their number and radius were equal for all devices in this series,
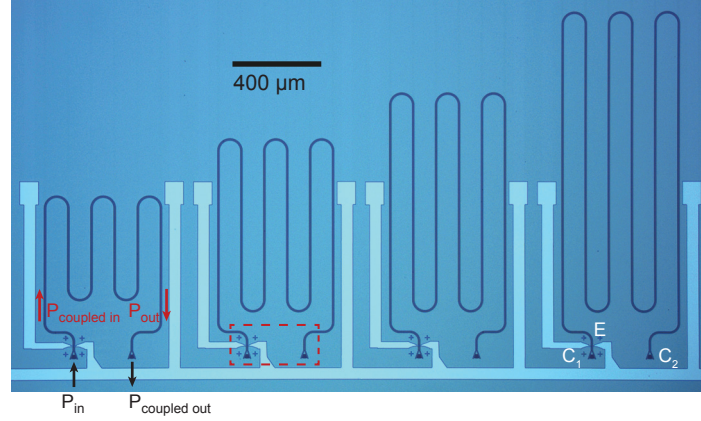
Figure 4.9: (a) Optical picture of four out of seven extended waveguide structures used for the estimation of propagation losses. Here, the total lengths L of the waveguides between the couplers are $3.6\,\text{mm}$, $5.3\,\text{mm}$, $6.5\,\text{mm}$ and $7.3\,\text{mm}$. The light power P_{in} is the input power of the external source before coupling into the chip plane (at the end of the fiber assembly). $P_{\text{out}}^{\text{coupled}}$ is the power measured with a spectrometer after coupling out of the chip plane. $P_{\text{in}}^{\text{coupled}}$ and P_{out} are the power values at the waveguide ends, before and after propagation, which can not be measured directly. All grating couplers have the same geometry, and coupling losses are assumed to be equal. *Source: adapted from* [35].

keeping the radiation losses equal. Thus, the increase in propagation losses is caused by scattering and absorption losses, which scale with the length of straight paths. In general, to calculate the propagation losses in a waveguide, the transmitted optical power through a section of the waveguide of known length was measured. The loss coefficient is defined as the difference between input and output (transmitted) power in dB, divided by the waveguide length: $\mathcal{L}\left[\frac{\text{dB}}{\text{cm}}\right] = \left(P'_{\text{input}} - P'_{\text{output}}\right)/L$.

The losses measured with an external supercontinuum source were compared to measurements with an internal SWCNT-source, thus the waveguide integrated SWCNT-emitter was exploited as a tool for measuring the waveguide losses. In this case, the SWCNT-emitter is the only source of photons on chip. The zoomed area of the internal emitter and both grating couplers are depicted in Fig. 4.10a. The emission map recorded in the free-space setup (Fig. 4.10b) shows bright spots at both, grating couplers and the source, similar to previous figures (Fig. 4.4). The same zoom factor as in Fig. 4.10a is used for clarity. The SWCNT-source is positioned $25\,\mu\text{m}$ away from the first coupler and $(L-25)\,\mu\text{m}$ away from the second one. With increasing length $\text{d}_{\text{E}-\text{C2}}$ the propagation loss increases, leading to a decrease in emission at the second coupler, observable in the emission map. The emission intensity collected by an objective into the field aperture $2\Theta = \sim 25°$ at both couplers $(I_{\text{C1}}, I_{C2}(L))$ is integrated over an equal area ($30 \times 30\,\text{pixels}$) indicated in Fig. 4.10b with a dashed rectangle. The background I_{BG}, integrated over the same region is subtracted. Making the assumption of equal coupling losses, the optical loss coefficient is defined as $\mathcal{L} = \frac{\text{d}}{\text{dL}}\left(10 \cdot \log_{10}\left(\frac{I_{\text{C1}}-I_{\text{BG}}}{I_{C2}-I_{\text{BG}}}\right)\right)$ again in units of $\left[\frac{\text{dB}}{\text{cm}}\right]$ (Fig. 4.10c), where $I_{\text{C1}}(L)$ is waveguide length dependent. The loss per length ($\mathcal{L}$) measured with the internal source is estimated
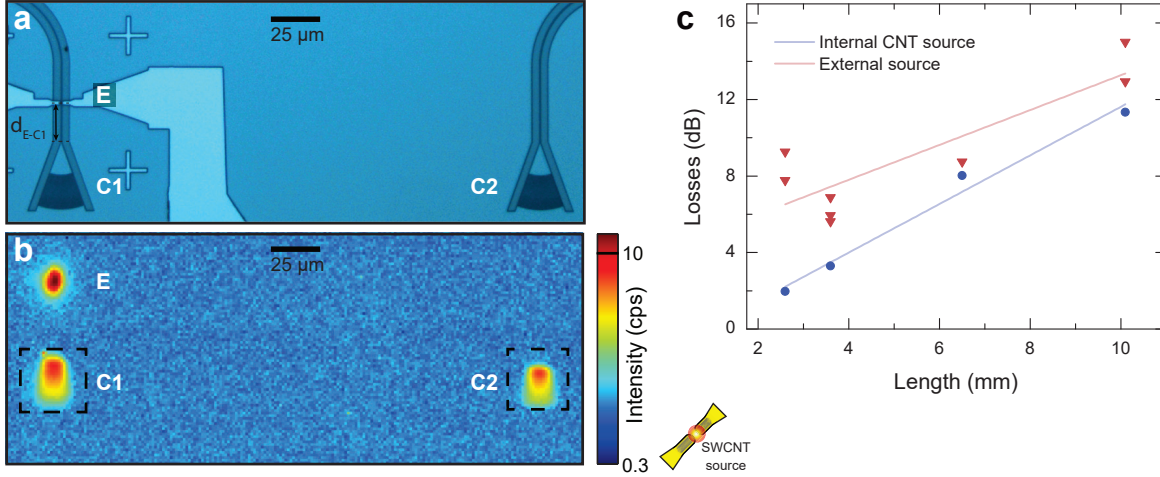
Figure 4.10: (a) Optical picture of a zoomed area, denoted on the previous picture with dashed line. The emitter and coupler positions are marked as E, C_1 and C_2. (b) Emission map of the same device with a length of $6.5\,\mathrm{mm}$. The emission is seen from the emitter directly and both coupler spots. (c) Propagation losses calculated with external (blue circles) and internal (red sqares) sources for four devices. In case of the internal SWCNT-source, measurements at various DC-biases were performed for statistics. Linear fits to the data reveal propagation losses of $9.1 \pm 2.1\,\frac{\mathrm{dB}}{\mathrm{cm}}$, measured with SWCNT-source and $12.7 \pm 1.2\,\frac{\mathrm{dB}}{\mathrm{cm}}$, observed with the external supercontinuum source. *Source: adapted from* [35].

from the slope of the linear fit to the data as $9.1 \pm 2.1\,\frac{\mathrm{dB}}{\mathrm{cm}}$. The propagation losses are averaged over the bandwidth of the CCD detector ($\sim 600\,\mathrm{nm}$). Waveguide contaminations due to the deposition of the nanotubes (e.g., surfactant residues, which is deposited mostly between the contacts) elevate the propagation losses and causes the discrepancies in the data points (Fig. 4.10c, red squares). Also this contaminations can be a reasonable explanation, why $\mathcal{L}$ is above the expected value for $\mathrm{Si_3N_4}$ waveguide.

The fiber-coupled setup (subchapter 4.1) with an external supercontinuum light source and an external spectrometer was also used to determine the propagation loss. The grating structures at the waveguide ends were used to couple the light into and out of the chip plane. Because of the unknown coupling coefficients ($\eta_{\mathrm{coupling}}^{\mathrm{in}} = P_{\mathrm{in}}^{\mathrm{coupled}} - P_{in}$, $\eta_{\mathrm{coupling}}^{\mathrm{out}} = P_{\mathrm{out}}^{\mathrm{coupled}} - P_{\mathrm{out}}$), the exact light power after coupling into and prior to coupling out of waveguide are unknown. Therefore, the loss coefficient was measured for several single mode waveguides with different length. Assuming that the coupling losses at all grating couplers are equal, the resulting loss coefficient ($\mathcal{L}$) was estimated from the linear fit to the data, where the losses plotted in dB (Fig. 4.10c). Obviously $0 \leq \eta_{\mathrm{coupling}}^{\mathrm{in}}, \eta_{\mathrm{coupling}}^{\mathrm{out}} < 1$. Then, the optical loss coefficient ($\mathcal{L}$) of a waveguide with total length L [cm] between the couplers can be calculated as $\mathcal{L} = \frac{\mathrm{d}}{\mathrm{dL}}\left(P_{\mathrm{in}} - P_{\mathrm{out}}^{\mathrm{coupled}}\right)$, where the light power is measured in dB. However, our spectrometer measures the light intensities in counts per second (cps), and the loss coefficient was calculated as $\mathcal{L} = \frac{\mathrm{d}}{\mathrm{dL}} \log \frac{I_{\mathrm{in}}}{I_{\mathrm{out}}^{\mathrm{coupled}}}$. The input intensity was measured with a reference detector. The transmission spectra of four devices are presented in Fig. 4.9b. They
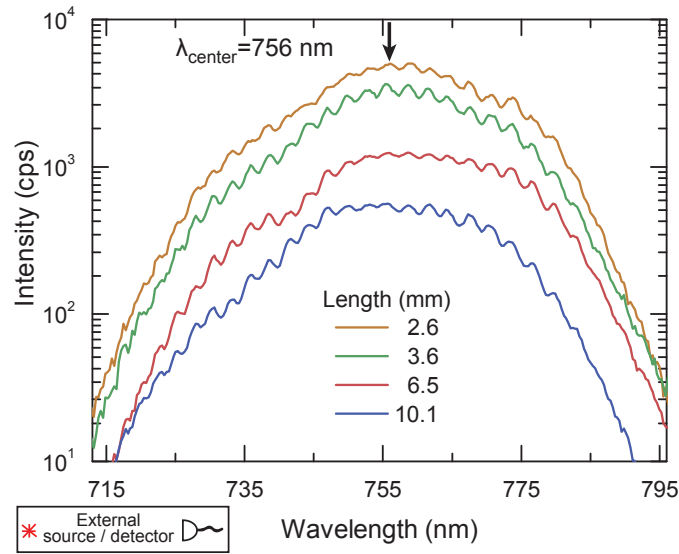
Figure 4.11: Transmission spectra, measured with a supercontinuum light source and a spectrometer for four waveguide lengths. The propagation losses are calculated for the center wavelength of the Gauss-shaped profile, $\lambda_{\text{center}} = 756\,\text{nm}$. *Source: adapted from* [35].

reveal the Gaussian spectral shape, typical for grating couplers. The intensity modulation with the free spectral range of $\sim 3\,\text{nm}$ and the cavity length of approximately $\sim 90\,\text{µm}$ causes most probably by Fabry-Perot interference between the fiber-array bottom and the grating coupler. Owing to the low spectral resolution of the spectrometer ($1.5\,\text{nm}$), these features are not completely resolved. The loss was calculated for one particular wavelength ($\lambda = 765\,\text{nm}$) - the center wavelength of the transmission spectrum for the presented grating couplers. The resulting average loss per unit length calculated with this method is $12.7 \pm 1.2\,\frac{\text{dB}}{\text{cm}}$. This value is in good agreement with the one calculated with an internal source after the SWCNTs deposition. The difference might be explained by the discrepancy of the results measured with the internal source. However, the absolute value of $12.7\,\text{dB}$ is high compared to the intrinsic absorption losses of Si_3N_4 [114]. It is probably caused by a high scattering loss due to side roughness of the waveguides, which can be reduced by more accurate fabrication.

4.2.5 Mach-Zehnder interferometer

We realized a series of Mach-Zehnder interferometer (MZI) devices on a chip, with waveguide-coupled SWCNT-sources integrated and measured (in transmission and emission modes) by the same methods as in the previous chapters. Fig. 4.12a shows one such MZI-device, consisting of two grating couplers, an on-chip emitter and an in-plane interferometer, which contains two Y-shaped beam-splitters and two waveguides with different path lengths in-between. The waveguide starts at the first grating coupler (C_1) and passes the metallic contact pair with the integrated SWCNT-source (E). The waveguide is then divided into two arms with a path difference $\triangle L$ by a beam splitter, which are combined again at the second beam-splitter. The light is coupled out at the second grating coupler (C_2). The transmission

spectra, measured with a supercontinuum light source (Fig. 4.12b) and a spectrometer, are intensity-modulated Gauss-shaped grating coupler spectra, due to interference of the modes passing the resonator arms with $\triangle L = 50\,\mu\text{m}$ prior to recombination. The path lengths between the grating couplers are $640\,\mu\text{m}$ and $690\,\mu\text{m}$ for bottom and top arms, respectively. The measured (blue circles) and calculated (green line) spectra with wavelength dependent intensity proportional to $\cos^2 \frac{\pi\lambda}{\triangle\lambda}$ multiplied by a Gauss function are presented in Fig. 4.12b. The distance $\triangle\lambda$ between the maxima, called free spectral range (FSR), depends on the wavelength and can be extracted from this data. The theoretical function is calculated based on a Gauss function multiplied by an interference term:

$$f_{\text{transmission}} = y0 + \frac{A}{\sqrt{\pi/2}w} \cdot \exp\left(-2\left(\frac{\lambda - \lambda_0}{w}\right)^2\right) \times \cos^2\frac{\pi\lambda}{\triangle\lambda}$$

The free spectral range FSR ($\triangle\lambda$) is calculated according to the following equation $\triangle\lambda = \lambda^2/(n_{\text{g}}(\lambda) \cdot \triangle L)$ (Eq.), where $n_{\text{g}}(\lambda)$ is calculated from $n_{\text{eff}}(\lambda)$, as shown in chapter 2.3.1 [115]. The FSR is also extracted from the measurement with an internal source for comparison. Upon electrical biasing, the SWCNT emits light in the visible range, which can be recorded with a CCD camera directly at E, C_1 and C_2. In an emission map recorded at C_2 (Fig. 4.13a) narrow maxima of interference fringes are clearly visible, compared to broad maxima, originating from interference with the back-reflected light from the substrate (Fig. 4.7a). The spectra shown below (Fig. 4.13b) were obtained by integrating over the spatial component. Like in a previous chapter (4.2.2), the integration was performed over a small area, reproducing the geometrical size of the coupler (marked with a dashed line in Fig. 4.13a for C_2). For comparison, a spectrum recorded at E is shown in the same plot. The overall intensity at C_2
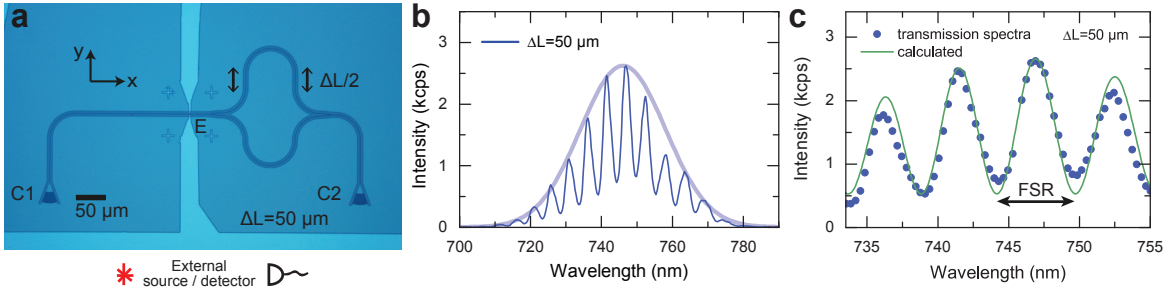

Figure 4.12: Mach-Zehnder interferometer: (a) Optical picture of the device. The waveguide is split into two arms with path difference $\triangle$L, and combined again. The emitter is integrated on the waveguide prior to splitting. Light passing the MZ resonator interferes and is coupled out at C2. (b) Transmission spectra through the MZI-devices with path differences $\triangle\text{L} = 50\,\mu\text{m}$, measured with an external supercontinuum source and spectrometer, enveloped with the Gauss function to illustrate the spectral bandwidth of the couplers. (c) Zoom into the central wavelength range of the spectrum shown in (b). Transmission spectra (blue circles) show a typical Gauss-form modulated by interference fringes and calculated interference spectrum ($\sim \cos^2 \frac{\pi\lambda}{\triangle\lambda}$) multiplied by a Gauss-function with the amplitude of the measured spectrum (green line). The free spectral range (FSR, $\triangle\lambda$) is indicated by a black arrow. *Source: adapted from* [35].

(red) follows the same trend as for the direct emitter position (E) (blue), where a long-wave modulation due to substrate interference along the surface normal is seen with intensity maxima at approximately 750 nm and 850 nm (subchapter 4.2.2). Short-wave interference in the chip plane has a period ($\triangle\lambda$) of a few nanometers, which slightly increases with the wavelength. Thus, two simultaneous interference processes are observed, the first one with a period of 100 nm (mostly defined by interference in a 2 μm SiO$_2$ substrate) and a second one with a period of several nm due to the MZI. Interference fringes from electrically driven incandescent SWCNT-light is evidence that the thermal light from a source with reduced dimensions is partly temporal coherent, as was shown above in context of overall spectral shape modulated by interference along the surface normal (subchapter 4.2.2). The transmission and emission spectra recorded in the same device with a path difference $\triangle L = 50$ μm are shown side-by-side in Fig. 4.14a. The values of free spectral range ($\triangle\lambda$), extracted from these curves, are plotted in wavelength dependency (Fig. 4.14b). This periodicity ($\triangle\lambda$) can be also calculated according to the equation mentioned above (Eq. 4.2.5). The calculated value of 5.7 nm (at a wavelength of 768 nm) is close to the values measured with the SWCNT-source ($\sim$ 6 nm) and with the external source (5.8 nm).

4.2.6 SWCNT coupling to directional coupler

The integration of SWCNT emitters into directional coupler and nanobeam photonic cavity were tasks of the master students Randy Fechner and Valentin Fütterling, who completed their master thesis in our group.

Directional coupling between two parallel waveguides, brought into close proximity, allows for routing of the propagated light and wavelength-depended power transfer from one waveguide to another. Directional couplers, similar to Mach-Zehnder interferometers or prolongated waveguides, are common elements of nanophotonic circuits [116]. The implementation of a carbon nanotube emitter coupled to such a device (Fig. 4.15) is shown in this subchapter. The directional coupler (DC) consists of two waveguides, which are brought close to each other for a specific coupling length L_{coupl} (Fig. 4.15b,c). In the central part of the DC, evanescent fields of optical traveling modes in two parallel waveguides are overlapped. Hence, power of the propagating mode from the input port is coupled into the adjacent waveguide and back. The splitting ratio is wavelength and coupling (interaction) length L_{coupl} dependent. After a certain path length $L_{100\%}$ the power is completely transferred from the input to the "drop" port, hence, if $L_{\text{coupl}} = L_{100\%}$ no transmission at the "through" port is obtained. A series of devices with various coupling lengths was fabricated. We compared two devices with $L_{\text{coupl}} = 5$ μm and $L_{\text{coupl}} = 21$ μm and different grating period. The coupling (or interaction) length is defined here as the path length, where the waveguides are parallel to each other, the actual interaction length is slightly longer. The coupling efficiency is proportional to $\sin^2\left(\frac{\pi}{2} \cdot \frac{L_{\text{coupl}}}{L_{100\%}}\right)$, according to theory [118]. For example, in the second order correlation experiments (chapter 5) on-chip a 1:1 splitting ratio has to be realized, then the required interaction length is half of the interaction length for the 100 % coupling ($L_{50\%} = \frac{1}{2} \cdot L_{100\%}$). If the interaction length is further increased, more power is transferred into the adjacent waveguide. The coupling efficiency of a directional coupler, which is defined as $\eta_{\text{DC}} = \frac{I_{\text{through}}(\lambda)}{I_{\text{through}}(\lambda) + I_{\text{drop}}(\lambda)}$,
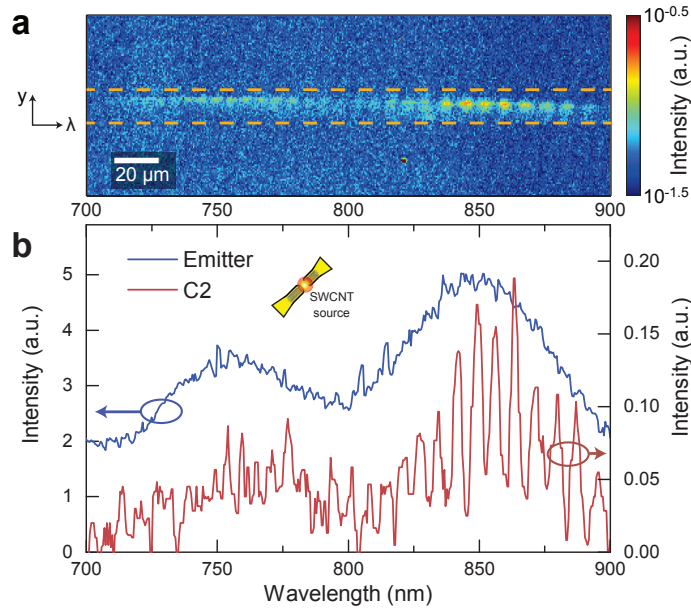
Figure 4.13: Interference of SWCNT-light in a Mach-Zehnder device. (a) Emission map of SWCNT-light recorded with a CCD detector, spatially resolved in y-direction. The dashed line marks the position of the coupler C_2. The direct emission and emission at the coupler C_1 are not shown on the map. (b) SWCNT emission-spectra, integrated over the spatial component (in-between the dashed lines in a), recorded (not simultaneously) at E (blue) and C_2 (red). Here, the overall spectral modulations with a period of $\sim 100\,\mathrm{nm}$ is caused by out-of-plane interference, while the short-wavelength modulation with $\sim 5-8\,\mathrm{nm}$ period is due to in-plane interference in the Mach-Zehnder interferometer. *Source: adapted from* [35].
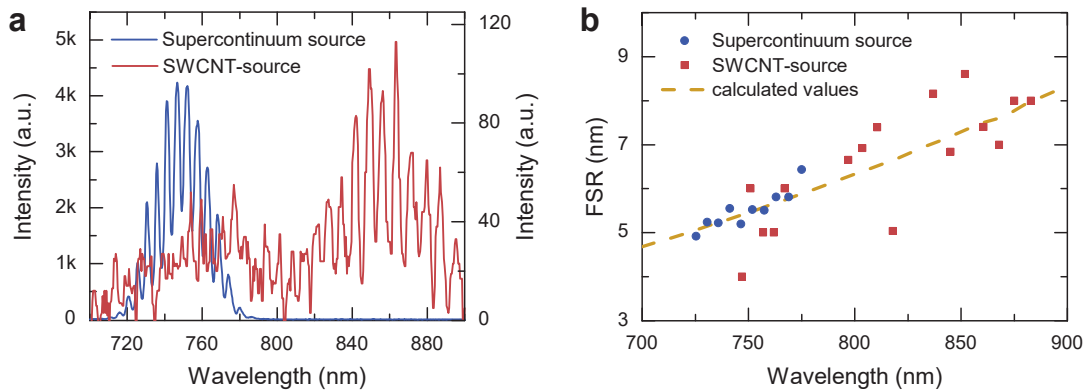

Figure 4.14: (a) Transmission (blue) and emission (red) spectra measured in the same device with $\triangle L = 50\,\mu\mathrm{m}$. (b) Free spectral range (FSR), extracted from the spectra shown in (a), along with calculated FSR values (orange line). *Source: adapted from* [35].
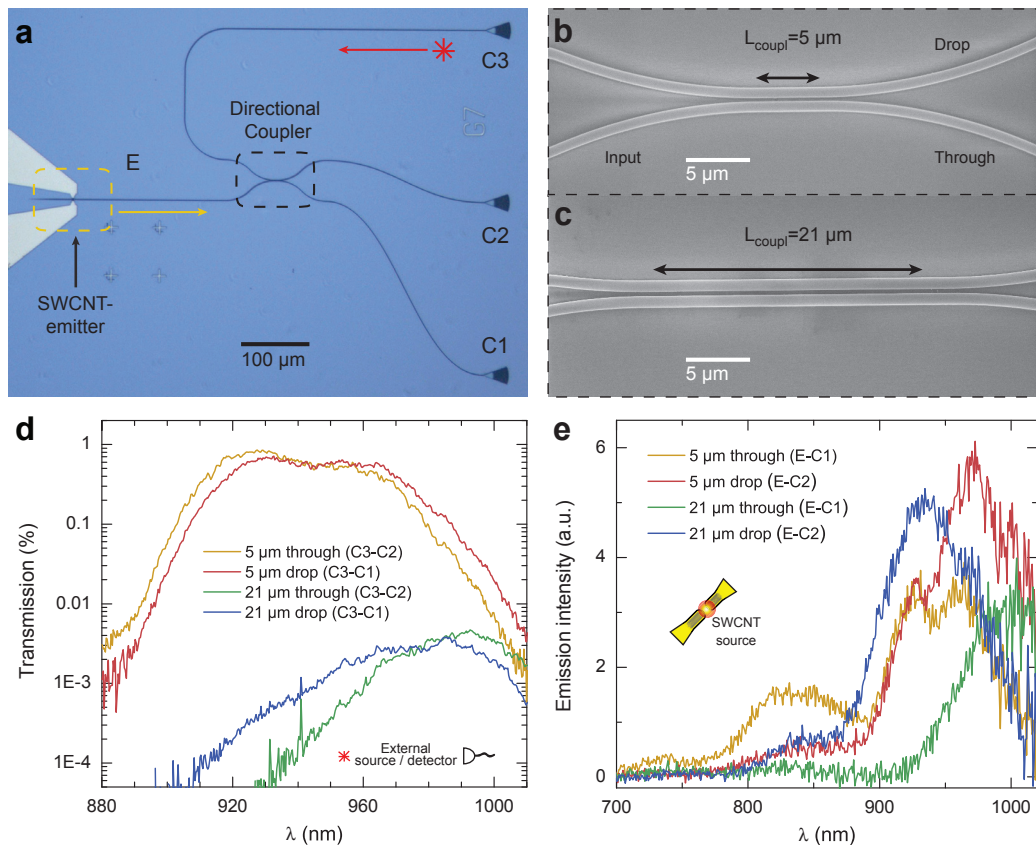
Figure 4.15: (a) Optical micrograph of a SWCNT-emitter (E), integrated in a directional coupler device. (b,c) SEM pictures of the area marked directional coupler in (a), with a coupling length of $L_{\mathrm{coupl}} = 5\,\mu\mathrm{m}$ (b) and $L_{\mathrm{coupl}} = 21\,\mu\mathrm{m}$. (d) Transmission spectra of external light, coupled into the waveguide through C_3, transmitted directly towards C_2 and coupled by the directional coupler towards C_1. Two devices with $5\,\mu\mathrm{m}$ and $21\,\mu\mathrm{m}$ coupling length and different grating coupler periods were measured. Both spectra have a Gaussian-shape, typical for grating couplers. (e) Emission spectra, measured with an internal SWCNT-source. Light coupled from E propagates to the right, is directly transmitted towards C_1 and is coupled by the directional coupler towards C_2. The emission spectra recorded at the couplers C_1 and C_2 show typical for our devices intensity modulation with period on the scale of $100\,\mathrm{nm}$. *Source: adapted from* [117].

was extracted from measurements with an external light source (Fig. 4.15d), as well as based on metallic SWCNTs internal source (Fig. 4.15e). The external light was coupled into the waveguide from the grating coupler C_3. Transmission spectra were measured at both C_1 and C_2 grating couplers (Fig. 4.15d), after propagating inside the "through" and "drop" waveguides. The spectra reveal the Gauss-shaped profile of the different gratings. The emission spectra represent thermal light, modulated by the interference with a period of $\sim 100\,\mathrm{nm}$. In the spectra recorded at the shorter device ($5\,\mathrm{\mu m}$) an intensity drop at the coupler specific wavelength (at normal incidence) is clearly visible (in particular, in orange plot). At the points where the transmission on both output couplers is equal, the coupling efficiency is $50\,\%$, meaning that half of the power is transmitted into the "drop" port (C_1) while the other half is propagated into the "through" port (C_2). For the internal SWCNT-source, transmission spectra can be measured in a wider spectral range (700–$1000\,\mathrm{nm}$) than for the external supercontinuum source, whose spectrum is shaped by the grating coupler's profile (880–$1010\,\mathrm{nm}$). The coupling efficiency η_{DC} is calculated from the transmission as well as emission curves respectively, measured at the "through" and "drop" ports for a certain interaction length of the directional coupler. Therefore, it can be observed in Fig. 4.16, that the extracted coupling efficiency shows an expected $\eta_{\mathrm{DC}} \sim \sin^2$ behavior. The extracted efficiency from the external source perfectly matches the one measured in emission mode for both long and short coupling length. The $50\,\%$ coupling efficiency $\eta_{50\%}$ is observed at a wavelength of approximately $950\,\mathrm{nm}$ and $975\,\mathrm{nm}$ for a coupling length of $5\,\mathrm{\mu m}$ and $21\,\mathrm{\mu m}$, respectively. As conclusion, an on-chip power splitter was combined with an internal SWCNT-emitter. A wavelength-dependent coupling efficiency was shown for two device geometries (long and short interaction length) with a good agreement between measurements with external and internal light source.
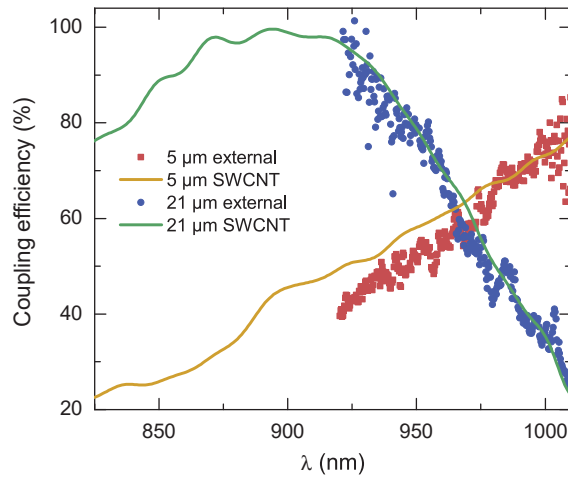
Figure 4.16: Coupling efficiency, calculated from the spectra, shown in Fig. 4.15d, e for external (scatter) and internal (lines) sources, respectively for two devices with an interaction length of $5\,\mathrm{\mu m}$ and $21\,\mathrm{\mu m}$. The results reproduce each other for both geometries, respectively. For the wavelengths $950\,\mathrm{nm}$ and $975\,\mathrm{nm}$ a splitting ratio 1:1 is observed for given geometries. *Source: adapted from* [117].

### 4.2.7 SWCNT inside of a nanobeam photonic crystal cavity

For optical on-chip communication, an integrable source with nanoscale footprint and a narrow spectral emission line would be of great advantage. The broad-band thermal light, presented in the previous subchapters, requires optical filtering in order to fulfill this condition of narrow-band emission. A photonic crystal nanobeam cavity (PCNBC) (Fig. 4.17) is designed to couple and enhance particular optical modes, which are further propagated within a waveguide. Hence, PCNBC-based devices can perfectly combine the advantages of established integration techniques of SWCNTs with high quality optical filtering. Therefore, broad-band thermal emission can be transferred into narrow-band light (down to several nanometers), as required in many on-chip applications. A photonic crystal cavities can similarly tailor electroluminescent quantum light, broadening due to hot carrier injection or surface interaction (with a bandwidth of $\sim 50\,\mathrm{nm}$). Due to high reproducibility of the spectral properties, a hybrid SWCNT-PC-device can be used as an indistinguishable photon emitter.

In a first approach, Park et al. [29] coupled electrically induced light from a semiconducting nanowire (CdS) into a photonic crystal cavity. A SWCNT-emitter placed in the center of such a photonic crystal cavity was shown as an ideal approach for wafer-scale applications [33]. We have employed a photonic crystal nanobeam cavity for optical filtering of the broad-band incandescent spectrum of a SWCNT-emitter [108]. Figures 4.17a and b show SEM-images of the fabricated device and zoomed area of the PCNBC, which consists of an under-etched air-suspended waveguide. Devices with an airmode and dielectric mode cavity were fabricated. In the first case, the maximum electric field was situated within the etched holes, while the SWCNT bridging the two electrode fingers is placed on top of the waveguide in-between the two central holes (Fig. 4.17a, inset), and thus, in a field node. Therefore, the SWCNTs do not affect the waveguided mode. The waveguide is terminated with the two grating couplers. The emission is evanescently coupled with high efficiency and in a symmetric PCNBC design transferred equally in both directions, as can be seen in a FDTD simulation of the fundamental mode (Fig. 4.17c). The light is scattered into the far-field on the grating couplers. Similar to all our devices, three high intensity spots are observable on the emission map (not shown here). The zoomed area of the PC-SWCNT-source under external illumination along with the superimposed spatially resolved emission intensity is depicted in Fig. 4.17d. Light with a wavelength outside of the cavity bandwidth is suppressed and partly scattered on the punched structure indicating the PCNBC (purple lines along the waveguide right and left from the center emission spot). The PCNBC can also be designed as a mirror and transmit the optical mode only in one direction, if the number of holes left and right is not equal. From the side with more holes the SWCNT-emission reflects almost completely. Thus, the optical properties of a PCNBC can be tailored to select and enhance light with a certain wavelength, as well as for power splitting. The grating coupler transmission spectrum is centered at a wavelength of $980\,\mathrm{nm}$, as well as the fundamental mode of the nanobeam cavity. Within the bandwidth of the grating couplers, several resonant modes of the PCNBC were tuned by adjustment of the photonic crystal geometry. The simulated and measured spectra from the air mode cavity are shown in Fig. 4.18. The normalized transmission was simulated with the FDTD method and depicted in Fig. 4.18a, showing two asymmetric and one symmetric cavity resonances, designated as 1a, 3a and 2s. The field distribution of the
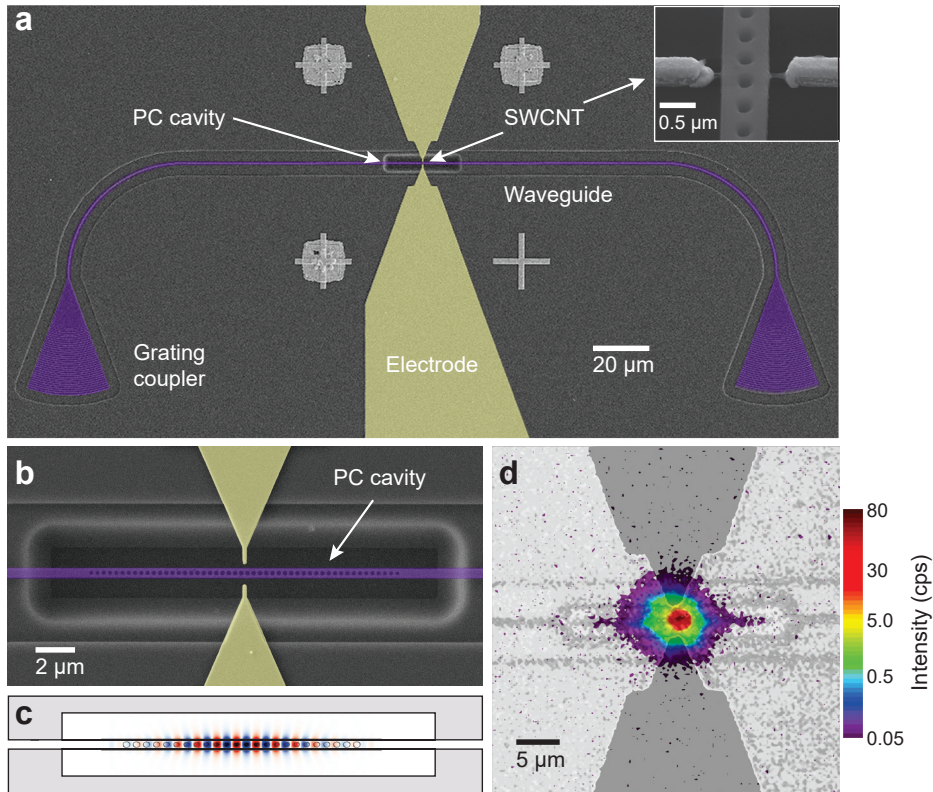
Figure 4.17: SWCNT-source integrated into a photonic crystal cavity. (a) SEM micrograph of a PC-device with a waveguide integrated SWCNT bridging metallic contacts. (b) SEM picture of zoomed area of the air mode cavity between two electrodes, and SWCNT bridging them. (c) Simulated optical mode in the cavity from (b). (d) Emission map of the SWCNT-emission, recorded in the free-space setup (colored), superimposed with a gray-scale optical picture of the PC-device with symmetric cavity. *Source: adapted from* [108].

fundamental mode (1a) is presented in Fig. 4.17c. The transmission from two devices with different cavity geometry, measured in the fiber-coupled setup, is shown in Fig. 4.18b and c. The narrow-band peak positions experimentally reproduce the simulated PC-cavity design dependentvalues. Deviations between the measured and simulated wavelengths are due to fabrication uncertainties of the hole diameters. One can observe that the fundamental mode (1a) is strongly suppressed due to absorption of the metal contact, however the secondary mode (2s) dominates the spectrum. The internal SWCNT-source, integrated into the cavity, was then employed. The emission spectra recorded at the grating couplers reveal narrow peaks at a certain wavelength similar to the transmission spectra due to coupling to the cavity modes. The line width is close to the spectral resolution of the free-space setup (1.3 nm), and hence, an order of magnitude narrower than the EL bandwidth. Concluding, we show that the emitted, waveguided radiation is strongly enhanced at the cavity resonance and realize efficient coupling into the underlying waveguide [108]. Emission enhancement and high quality factor reveal an electrically driven SWCNT-emitter placed in a cavity as a preferable
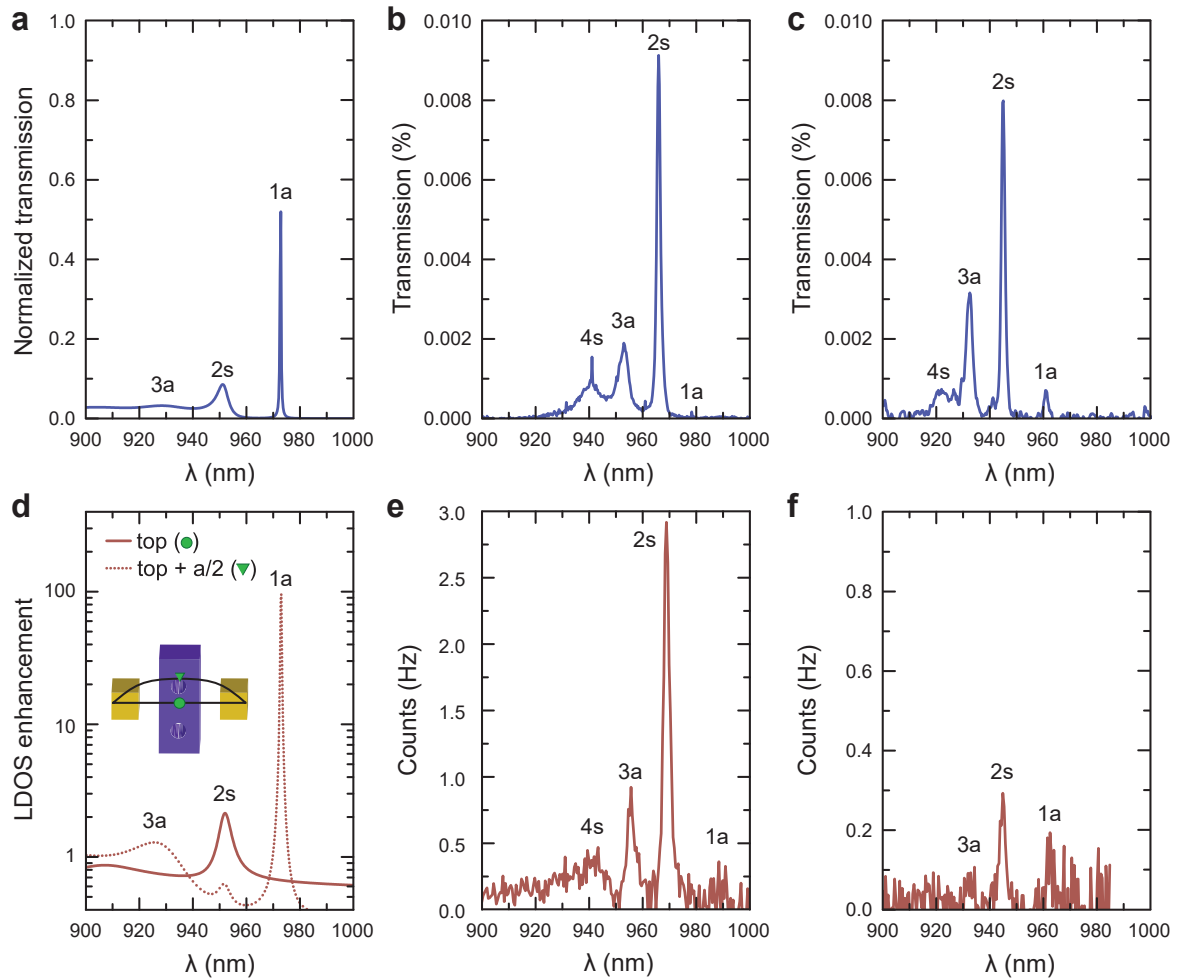
Figure 4.18: Transmission and emission spectra of SWCNTs integrated into waveguides with an air mode phonic crystal cavity. (a) The simulated transmission spectrum. (b), (c) Experimentally recorded transmission spectra for devices 1 (b) and 2 (c). (d) Simulated normalized intensity enhancement for light emission at the cavity center (red line) and over the photonic crystal holes (red dots) . The inset shows the position of the SWCNT for both cases. (e), (f) Spectra of the electrically driven SWCNT sources recorded at the grating couplers for devices 1 (e) and 2 (f), respectively (compare with (b), (c)). *Source:* [108].

choice as a high efficiency photon source with tunable narrow spectral range. Emission peaks at arbitrarily designed wavelengths, an order of magnitude narrower compared to electroluminescence, can be achieved. Moreover, cavity-enhanced emission can be operated in a GHz frequency range due to high-speed electrical biasing. These experiment and results are discussed in the next part of this chapter.

4.3 Pulsed emission from RF-biased CNT

A fast conversion from electrical into optical signals and vice versa is the key technology for many hybrid opto-electronic systems. In this chapter, an application of SWCNT-based incandescent sources as high-speed electro-optical transducers fully compatible for integrated photonic platform is discussed. The realization of a hybrid photonic waveguide-SWCNT-device is demonstrated, and the generation of an optical pulse train with a frequency of 2 GHz and a decay time of 80 ps is shown, making SWCNTs a good candidates for nanoscale electrically-driven pulsed light sources in the GHz range [95].

4.3.1 TCSPC setup

Our time-correlated single-photon counting (TCSPC) setup is a modified version of the previously described fiber-coupled setup. The transmission through the waveguide with grating couplers was optimized first, using an external source (white light source, LEUKOS). The difference to convenient device transmission measurements is, that after this optimization, the external source was disconnected, and the driven electrodes of SWCNT-device were contacted to explore the light emission of the internal waveguide-coupled SWCNT-source. A pulsed electrical bias voltage is applied to the SWCNT-based source through a contact probe (Cascade Microtech), whose position can be optimized by means of a 3-axis stage. The RF-voltage was produced by a pulse generator (PG, Agilent 8131A, 8133A), enabling sharp pulses in a different range of frequencies and widths. Unfortunately, this value is too low for generation of stable emission, because of attenuation due to propagation and coupling losses. The emission intensity after propagation inside the waveguides and coupling out of the chip surface has to be high enough for time-resolved detection in the fiber-coupled setup. In particular, it must be higher as the scattered background light. The estimated overall detection efficiency of the setup is about$\sim 10^{-6}$. It was limited due to the small collection aperture of the fibers, spectral selectivity of the grating couplers, as well as detection efficiency of the CCD-detector. The maximal amplitude of the pulses (V_{RF}) is 3–5 V, depending on the pulse width and generator model. Therefore, additional DC-biasing was applied by a constant voltage source (Keithley 6430) via bias tee (ZFBT-6GHz, Mini Circuits) to circumvent this limitation. The DC-voltage (V_{DC}) was chosen as the minimal value needed to overcome a device-dependent threshold voltage, after which the count rate (CR) exceeds a background (100 cps), hence, emission can be detected. The RF-amplitude is chosen as big as can be generated for a given pulse width.

Upon applying a RF bias, the SWCNTs emit pulsed light, which is evanescently coupled into the underlying waveguide, splitted by it in two opposite directions at a splitting ratio of approximately 50:50, and is coupled out into the far-field. Where it is detected by a

ultrafast, fiber-coupled detector. Due to the implementation of a high-speed low-noise single-photon avalanche detector (τ-SPAD-100) or superconducting nanowire single-photon detector (SNSPD), a high timing resolution is achieved. The TCSPC technique [55] (start-stop technique) is used to record a time resolved emission (Fig. 4.2a, b). The arrival times of incoming photons, defined as the time delay between start and stop signals ($\tau = t_{\text{start}} - t_{\text{stop}}$), are accumulated into a histogram with a maximal timing resolution of 4 ps by a calibrated pulse counter (Picoharp 300). The synchronized output of the pulse generator has been set to generate inverted pulses and is used as a counting start t_{start}. A pulse amplitude of -300 mV was chosen to fulfill the input signal conditioning of the counter. An incoming photon is absorbed by the detector and initiates a short current pulse either due to an electronic avalanche in the SPAD or breaking of the superconductivity in the SNSPD (subchapters 2.3.2, 5.1). This pulse acts as a stop signal at time t_{stop} for the counting. The histogram counts were collected over many electrical pulses. Pulses in a frequency range of 1–5 MHz and various widths ($w = 150$ ps–200 ns) were applied to the SWCNT-devices during the experiment. The time-resolved electrical pulses were measured with a fast oscilloscope (Infinium 6 GHz, Agilent). To do so, we applied the pulsed voltage from the generator to the metallic leads on the chip, which were connected by the utilized RF-contact probe, and measured with the oscilloscope, also connected to these on-chip leads. For comparison, the electrical signal was measured directly on the oscilloscope. The amplitude V_{RF} measured on the chip was reduced, compared to the directly measured one. Also, the rising and falling edges of the signal appeared smoother. The absolute value of the pulse amplitude V_{RF} changes with the w and period in case of "slower" PG (Agilent 8131A), and for pulses shorter than 1 ns, V_{RF} is significantly decreased (due to pulse generator itself). The "faster" PG (8133A) on the contrary, is suited for shorter pulses down to $w = 150$ ps. The TCSPC experiment was performed both at ambient conditions and in vacuum (10^{-5} mbar). In vacuum, a much higher V_{DC} can be applied (up to 20 V), since the electrical breakdown voltage of the SWCNTs is higher than in air (Fig. 4.19c). Count rates up to 10^5 cps are achieved and remain stable over hours of measurement. Such high count rates help to reduce the accumulation time and, therefore, to increase the signal to background ratio. Also, the vacuum chamber has the additional function of reducing the unwanted dark counts. The intrinsic dark count rates of the respective detectors are around 70 cps for τ-SPAD and < 1 cps for SNSPD. Nevertheless, we can assume, that the origin of the "background" in the accumulated histogram is mainly because of the constant SWCNT emission under V_{DC}, which is applied during the whole pulse period. Insufficiently low V_{RF}, enabled by PG output, could be also amplified, instead of applying V_{DC}, but a broad-band high-speed amplifier is needed for this purpose.

Films and single SWCNTs, obtained from a gel-filtrated HiPco material, were implemented. As already explained in the previous chapter (3.2.3), the carbon nanotubes were deposited by DEP between the metal contacts. The sc-SWCNT-based as well as metallic SWCNT-based devices (inevitably) were operated in the incandescent mode. The waveguide and couplers are optimized for the visible wavelength range, while the main electroluminescence transition (E_{11}) is expected in the near-infrared. This choice is setup-limited, since the τ-SPAD detector employed in this experiment are sensitive only in the visible range. The nanotubes are aligned perpendicular to the waveguide, thus the incandescent emission is evanescently coupled into the waveguide with over 50% efficiency, propagates inside and couples out of the grating
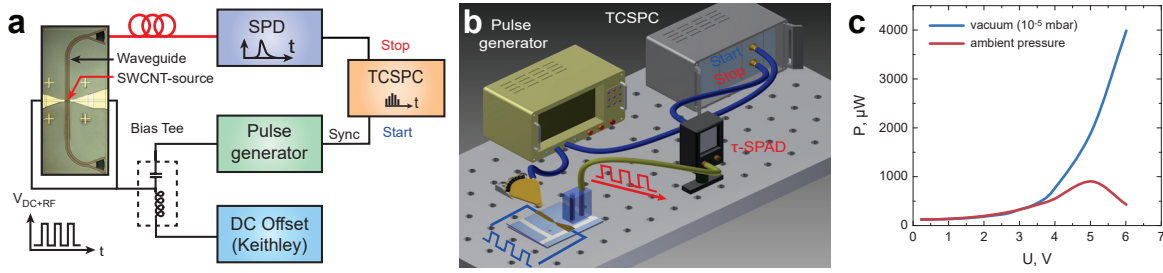
Figure 4.19: Time-correlated single-photon counting (TCSPC) measurement setup. (a) Schematic view: after pulsed (V_{RF}) and DC-voltage V_{DC} are applied to the driven electrodes over a bias Tee, SWCNT-emission propagates inside the waveguide, coupled out and is detected by the single-photon detector. The photon arrival times are accumulated into a histogram with TCSPC. (b) 3D view: a fiber array assembly and multi-contact electrical probe are aligned to the particular device. Optical pulses are generated after the pulsed voltage is applied. The time-synchronized electrical signal from the pulse generator was acting as a trigger. (c) Voltage dependency of electrical power in vacuum (10^{-5} mbar) and under ambient conditions. A breakdown voltage of $5\,V$ is observed in air for the presented device. *Source: adapted from* [95,108].

structures into free space, where it is detected. An important advantage of the TCSPC method is, that measurements at much lower excitation power is possible due to higher sensitivity of the detector.

4.3.2 Results and discussion

Ultrashort optical pulses were demonstrated to be emitted by a SWCNT-based light source, driven by electrical pulses at high frequency. The electrical pulses were applied to the driven electrodes by a fast pulse generator, the RF signal was biased by a DC voltage to overcome the minimal threshold for incandescent emission, which varies with different SWCNT-devices. As shown in figure 4.20 the optical pulses (bottom) follow well the applied electrical signal with different pulse length (top). After a short period of rapid increase of the intensity, a region with slow increase can be observed (Fig. 4.20, bottom). We attribute these two processes to a fast heating of the nanotube and a slow heating up of the substrate. These processes occur on a time scale of sub-nanosecond and tenths of nanoseconds, respectively. Once the electrical bias is switched off, the optical signal decays exponentially, and the value of the decay time can be extracted. The metallic leads on the chip were not designed for high frequency signals, thus causing the amplitude variation during the pulse. Time-resolved optical spectra reveal the distinct intensity drops at $\sim 25\,\text{ns}$ and $\sim 75\,\text{ns}$. Some time later the optical signal stabilizes.

The intrinsic decay time for incandescent emission of SWCNT can be theoretically estimated on the order of $10\,\text{ps}$. The value of the decay time of thermal emission depends on the mass density ρ_{CNT}, the specific heat capacitance c_{CNT} and the net thermal conductance g to the underlying dielectric substrate [34,119] and can be calculated as $\tau_{\text{therm}} = \frac{\rho_{CNT} \cdot c_{CNT}}{g}$. These three parameters were estimated from the literature for a SWCNT-diameter range of $0.8\text{--}1.2\,\text{nm}$ and a temperature range of $1000\text{--}1500\,\text{K}$ (the choice of this temperature range
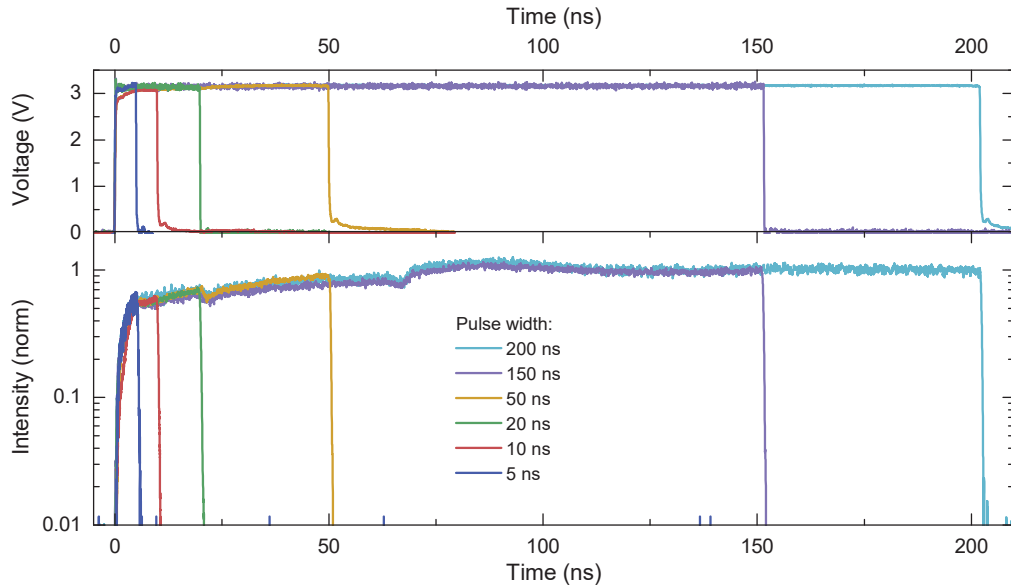
Figure 4.20: Upper panel: electrical pulses with various width of $w = 1 - 200\,\text{ns}$ and period of $1\,\mu\text{s}$, measured with an oscilloscope. Lower panel: normalized emission intensity upon driving the SWCNT-based devices with a pulsed electrical bias voltage, shown in the upper panel. The time-resolved optical signal is collected over many periods with the TCSPC technique. The variations in the intensity, in particular, the drops at $\sim 25\,\text{ns}$ and $\sim 75\,\text{ns}$, are due to impedance mismatch between on-chip metallic leads and pulse generator. *Source: adapted from* [95].

is discussed below). ρ_{CNT} varies between $0.7\text{--}1.8 \cdot 10^{-15}\,\text{kg/m}$, c_{CNT} varies in the range of $2500\text{--}3900\,\text{W} \cdot \text{s/kg} \cdot \text{K}$ [120,121] and thermal conductance g has a value of $0.1\text{--}0.3\,\text{W/m} \cdot \text{K}$ [119]. Thermal conductance is relatively low because of the small nanotube-substrate interface, which limits the heat transfer into the substrate. The heat capacitance is a parameter which increases with the temperature, while ρ_{CNT} and g do not possess such strong dependency in the above-mentioned temperature range. Out of these theoretical consideration follows, that the incandescence decay increases with the temperature. This calculated value of the time decay varies in the range of $5\text{--}70\,\text{ps}$ for the parameter range, given above. The theoretical value of SWCNT incandescence decay ($10\,\text{ps}$) leads to a potential rate of $100\,\text{GHz}$ for SWCNT-based electro-optical transducers.

We experimentally realized a fast, nanoscale photonic source, which generates optical pulse trains with rates of up to $2\,\text{GHz}$. This maximal value of applied frequency is limited by the pulse generator, and can, theoretically, be further increased up to $100\,\text{GHz}$. The pulsed optical signal propagated within the waveguides are shown for 1 and $2\,\text{GHz}$ rates in figure 4.21a and b. The width of the pulse at the half of the maximum (FWHM) is below $250\,\text{ps}$. The optical pulse trains also were recorded under a bias frequency of $0.2\,\text{GHz}$ and $500\,\text{ps}$ pulse width on metallic SWCNT-based device (Fig. 4.22, a). The fitted decay values of each peak of the train differ from each other, even though they were recorded on the same device. We obtain an averaged value of $\tau_{\text{exp}} = 219\,\text{ps}$. The decay times of the
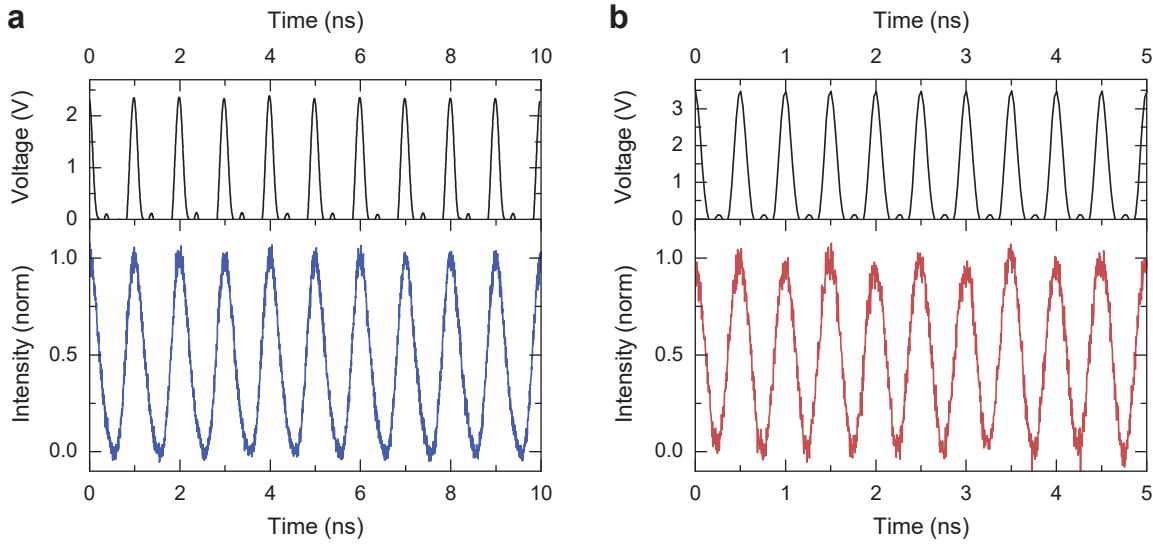
Figure 4.21: Normalized SWCNT-emission intensity (lower panel) detected with TCSPC with respective sequence of short electrical pulses (top panel) with $150\,\mathrm{ps}$ width and a frequency of $1\,\mathrm{GHz}$ (left) and $2\,\mathrm{GHz}$ (right). An RF-voltage with an amplitude of 2–$3.3\,\mathrm{V}$ of the pulsed sequence and an additional DC-bias voltage of $\sim 10\,\mathrm{V}$ were applied (the DC-offset is not shown in the top panel graphs). *Source: (b) is adapted from* [95].

time-resolved emission were extracted out of the optical pulse data (Fig. 4.22b) for devices with various nanotube densities (1–$100\,\mathrm{\mu m^{-1}}$) and different biasing conditions. Metallic as well as semiconducting nanotubes were explored. The decay times were extracted from the fitting to the optical emission decays between $10\,\%$ and $90\,\%$ of the pulse amplitude. Pulse trains but also "single" pulses with a lower frequency of 1–$5\,\mathrm{MHz}$ were obtained. Here, the term "single" pulse means, that only one pulse is applied during the $200\,\mathrm{ns} - 1\,\mathrm{\mu s}$ period and can be observed on the plot, because the limit of the time axis is $\sim 200\,\mathrm{ns}$ for $4\,\mathrm{ps}$ resolution. The values estimated from different devices were combined into a histogram (Fig. 4.22c). As can be seen from this graph, the decay varies between 180–$480\,\mathrm{ps}$. The normal distribution fitted to this data is centered around $230\,\mathrm{ps}$, while a higher averaged value of $270 \pm 90\,\mathrm{ps}$ is observed. The reason could be the low total histogram count and, hence, unresolved exponential decay. Concluding, the measured decay time does not systematically depend on any parameter, neither on density of the SWCNTs nor on their chirality. It is rather an instrumental restriction, occurring due to the cumulated timing jitter of the detector, pulse generator and the counting system $\tau_{\mathrm{all}} = \sqrt{\tau_{\mathrm{detector}}^2 + \tau_{\mathrm{el.\,pulse}}^2 + \tau_{\mathrm{Picoharp}}^2}$, where $\tau_{\mathrm{detector}} = 350\,\mathrm{ps}\,(\mathrm{FWHM})$, $\tau_{\mathrm{el.\,pulse}} \sim 80\,\mathrm{ps}\,(\mathrm{decay})$ and $\tau_{\mathrm{Picoharp}} = 16\,\mathrm{ps}\,(\mathrm{FWHM})$, while the last one can be neglected compared to the first term. As can be seen from this equation, the maximal timing error arises from the detector jitter, which can be avoided by implementing of detectors with a smaller timing jitter, like with SNSPDs (with a $20 - 40\,\mathrm{ps}$ FWHM). We have implemented commercially available fiber-coupled SNSPD detectors with $40\,\mathrm{ps}$ timing jitter (SCONTEL [122]) and extracted a much lower decay time of $79\,\mathrm{ps}$ (Fig. 4.22d). This value is close to the electrical pulse decay time ($\tau_{\mathrm{el.\,pulse}}$). The demonstrated decay time below
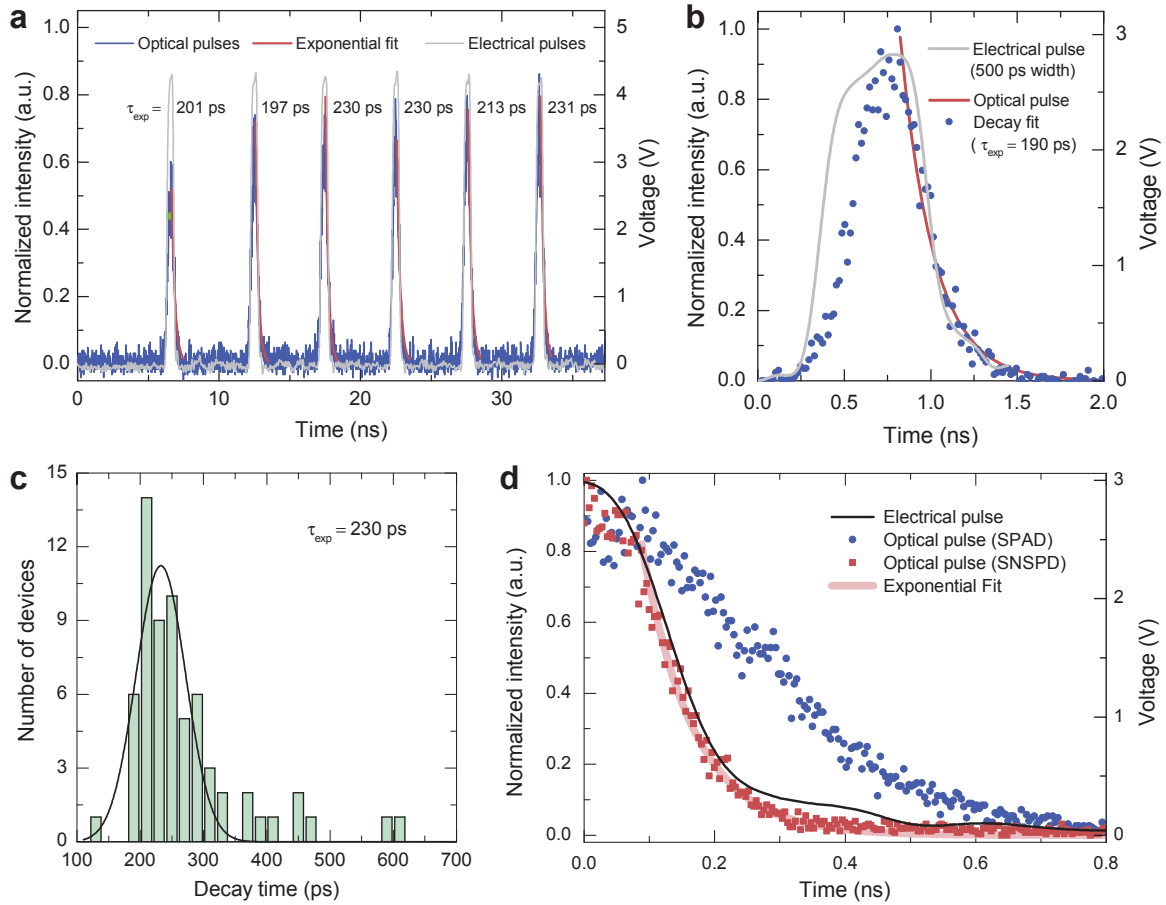
Figure 4.22: (a) A pulsed optical emission at $0.2\,\mathrm{GHz}$, each pulse is fitted to a single exponent, revealing an averaged $\tau_{\mathrm{exp}} = 219\,\mathrm{ps}$. (b) The optical emission (blue dots) of the film of single semiconducting SWCNTs under electrical bias (gray line) with $500\,\mathrm{ps}$ pulse width. The decay time τ_{exp} extracted from the exponential fit (red curve) is $190\,\mathrm{ps}$. (c) A histogram showing the decay time distribution for a large number of measured devices with an averaged $\tau_{\mathrm{exp}} = 270 \pm 90\,\mathrm{ps}$, while the normal distributed value is $230\,\mathrm{ps}$. (d) An optical emission decay of a high-speed SWCNT-transducer, measured with SNSPD (red rectangles) and SPAD (blue dots) detectors. The decay obtained from the exponential fit to the SNSPD measurement data is $\tau_{exp} = 79\,\mathrm{ps}$. *Source: (d) is adapted from* [95].

$80\,\mathrm{ps}$ for our waveguide-coupled SWCNT-sources manifests, that rates of up to $12.5\,\mathrm{GHz}$ can be experimentally realized. Due to the described restrictions, the intrinsic value of the SWCNT incandescence decay can not be resolved with the present setup, but still the obtained value below $80\,\mathrm{ps}$ is a significant step toward a high-speed waveguide-coupled SWCNT-based electro-optical transducer. If the decay time would be significantly (several times) higher than jitter, more accurate estimation would be possible by the TCSPC method, as for example, in many time-resolved fluorescence experiments. Fluorescence decay time of molecules with a typical value of several nanoseconds can be measured using detectors with jitter in the picosecond range (around $300\,\mathrm{ps}$ for commercial avalanche detectors). Thus, precise decay

times can be extracted in this case. As the next step towards more precise estimation, the instrument response function (IRF) with a setup-specific decay has to be recorded for further deconvolution [123] from the fluorescence signal. Then a "real" decay time can be estimated.

For an electroluminescent device with a lifetime comparable to the setup-limited decay, measurement of the IRF signal appears to be complicated. An alternative electrically driven source with much shorter decay time has to be measured with the same setup instead of the SWCNT-device. However, the SWCNT-source itself has a decay time, comparable to the commercially available light-emitting diodes (LEDs), which show decay times around 300 ps.

In addition, the pulsed incandescent emission of a SWCNT-based device has been studied in our free-space setup to investigate the spectral properties of the source and to estimate the temperature range of the SWCNT-emitter under pulsed bias. The light emitted from the SWCNTs directly into the upper hemisphere was collected by an objective and routed into the spectroscopy unit. Here, either a spatial intensity distribution or spectral-resolved emission was recorded (Fig. 4.23a and b). The spatially-resolved intensity was measured under various biasing conditions, such as different pulse amplitude V_{pulse}, DC bias V_{DC}, pulse width w and the duty cycle ($D = w/\text{pulse period}$) to characterize the fast response of the SWCNT-based pulsed emitter (Fig. 4.23a). As can be seen from this graph, the integrated emission intensity normalized to a duty cycle $I_{\text{norm}} = I/D$ is only voltage-dependent. Moreover, I_{norm} depends only on the pulsed amplitude V_{pulse}, if one neglects the device-specific constant bias V_{DC}, applied to overcome the emission threshold. Fig. 4.23a shows the emission intensity plotted on a logarithmic-linear scale versus $1/V_{\text{Pulse}} \left[\text{V}^{-1}\right]$. The pulsed light from four different devices was studied in a wide range of w (10–1000 nm) and D (0.02–0.2). It is clearly visible on the
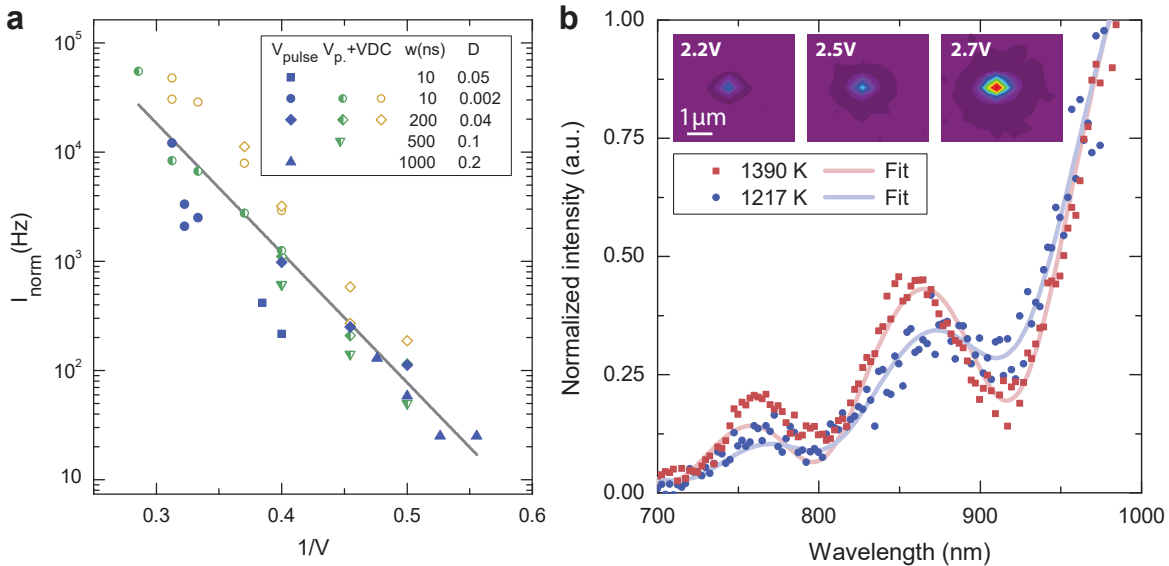
Figure 4.23: Normalized integrated emission from the incandescent SWCNT-transducer versus $1/V$ spectra under various biasing conditions (a); spectrally-resolved emission (symbols) with a fit (solid lines) (b). The inset shows the spatially resolved emission under the pulsed bias with $V_{\text{pulse}} = 2.2$, 2.5, 2.7 V amplitude. *Source: adapted from* [95].

log-lin scale, that the measured intensity (Fig. 4.23a) is distributed around the best linear fit (red line), yielding a slope of $c_{\text{slope}} = -27.3 \pm 1.9$. Hence, the exponential law $I_{\text{norm}} \sim e^{c_{\text{slope}}/V}$ applies. The dissipated electrical power, and therefore the temperature of the SWCNTs, increases linearly with the voltage ($T \sim V$), if the SWCNT is driven at high bias, as has been shown previously [119,124,125]. Therefore, this implies, that the exponential dependence $I_{\text{norm}} \sim e^{-E/kT}$ takes place. This dependence is typical for a thermal emitter at much higher temperature, hence with kT much larger than the characteristic energy E, detected by the experimental setup [95]. A similar behavior has been observed by Mann et al. for suspended CNTs. [126]

Three spatially-resolved emission maps were recorded with the free-space setup at the same device under different V_{pulse}. Fig. 4.23b (inset) show the bright spots at the position of emitter. The light intensity and spot size increases with the electrical pulse amplitude V_{pulse} at the constant values of $V_{\text{DC}} = 2.5\,\text{V}$, the pulse width $w = 200\,\text{ns}$ and duty cycle 0.04.

The spectrally-resolved emission of the SWCNT-source was measured as well. Similar to the SWCNT under DC-bias, the pulsed emission spectra reveal the typical behavior of thermal (Planck) sources superimposed with interference fringes due to the underlying substrate, independent on the chirality of the SWCNTs. The temperature obtained from the fit to the data is 1217 K for 2 V and 1390 K for 3 V pulse amplitude. The fitting procedure is discussed above (4.2.2). These extracted temperatures vary between 1000–1500 K, depending on the biasing voltages and the density of SWCNT film of the particular device. This temperature range was used for estimation of the intrinsic decay τ_{therm}.

Single-chirality SWCNTs have been shown as a wavelength-sensitive detector in the telecommunication wavelength range. Therefore, the introduced devices could also be implemented for reverse conversion of a high-speed optical signal into an electrical one. The ultrafast pulses of the external laser, coupled and propagated inside the waveguide, would evanescently excite the sc-SWCNT and lead to a photocurrent which could be recorded by TCSPC. However, the realization of such devices reaches beyond the scope of this work.

Conclusion

Our results show that SWCNTs can be seamlessly integrated into nanophotonic circuits and serve as internal waveguide-coupled source with high coupling efficiency. Our approach can potentially replace external fiber-coupled sources for a future device generation. Instead of narrow-band electroluminescent radiation of sc-SWCNT-based sources, a broad-band spectrum originating from thermal light due to Joule heating of the carbon nanowire was observed. Several broad peaks in the optical spectrum are owing to interferences along the surface normal. This interference is an evidence for partial coherence of the thermal light. Several hybrid devices with integrated SWCNT-emitter and linear optical elements for practical on-chip applications were realized. SWCNT nanoscale sources were implemented for signal transmission through extended waveguides. Directional couplers for routing and power splitting of the light emitted by the carbon nanotube were shown. The equal power splitting (1:1 ratio) is required, for example, in the device geometry for second-order correlation experiments. The appropriate minimal interaction length of directional couplers for a certain wavelength was estimated. A Mach-Zehnder interferometer with integrated SWCNT source

was realized to study coherence of thermal emission from a source with reduced dimensionality. Grating couplers were used to couple the waveguided SWCNT-induced light out of the chip plane into the far-field. Two distinct regions were defined at the coupler grating, where Bragg scattering of the light within the coupler bandwidth takes place and where diffusive scattering of the remaining light occurs. While the brightness of the emission can be easily adjusted with the current through the nanotube, the optical spectrum can be tailored by the photonic environment. The broad band incandescent emission was adjusted by integrating the SWCNTs into a photonic nanobeam cavity, enhancing the emission at designed wavelengths with high quality factor. The implementation of a broad-band detector in the NIR will provide the possibility to study the nanotube-specific electroluminescent light at the main transition E_{11}. The continuing improvement of SWCNT's sorting methods and controllable deposition processes allow the fabrication of devices with similar optical and electrical properties on a wafer-scale.

5 SWCNTs as non-classical light source

In the previous part, the basic operation principles of our integrated devices were shown. The coupling of the electrically driven carbon-based source into a waveguide was demonstrated, as well as the scalable fabrication of devices. These are the first steps leading to our main goal, the realization of single-photon sources. For demonstration of the non-classical nature of the light, generated from a carbon nanotube, correlation experiments have to be performed. Two single-photon detectors (typically avalanche photodetectors) are needed for this experiment. However, in a cryogenic setup, where we performed the measurements to suppress the thermal emission and the break-down due to the high power, avalanche photodetectors cannot be used. Therefore, two traveling-wave superconducting nanowire detectors at the ends of the waveguide were used, where the coupled source was integrated in its center. The efficiency of this detection method is much higher than that of external avalanche detectors, additionally to the broad-band spectral properties. After the deposition of the sorted suspension, consisting of semiconducting nanotubes with a particular emission wavelength, the sources can be driven purely electrically. The second-order correlation of the emission intensity can be measured with these two detectors in a Hanbury Brown and Twiss configuration. Moreover, the scalable integration of all components on the same device, such as source, detectors, and optical waveguide is performed. Scalability is necessary for indistinguishable single-photon sources, and co-integration is a crucial requirement for quantum optics on chip.

This chapter is based on and partly adapted from [57] *and its supplementary material.*

5.1 Nanophotonic device layout and measurement setup

Our nanophotonic device consists of three components: classical rib-waveguides, a single semiconducting SWCNT, bridging the metallic leads and oriented perpendicular to the waveguide, and superconducting nanowire single-photon detectors (SNSPDs), co-integrated on the same waveguide (see Fig. 5.1, Fig. 5.2). The non-classical electroluminescent light generated by individual sc-SWCNTs is efficiently coupled into the underlying waveguide, similarly to the incandescent light discussed in chapter 4. It is split in opposite directions inside the waveguide (as shown in the simulation, Fig. 4.5) and detected in the optical near-field by two superconducting nanowire (NbN) single-photon detectors, spaced equidistantly ($200\,\mu m$) from the SWCNT emission center. The design with two detectors, first used by Hanbury Brown and Twiss (HBT), [52] was used to perform the second order correlation experiments (subchapter 2.1.2). The co-integration of all three components allows for performing the measurements directly on chip without the need of an external detector. This is contrary to common second order correlation studies of SWCNT photoluminescence typically performed in a confocal setup using external detectors [46]. The fabrication of SWCNT single-photon sources and SNSPDs (chapter 3.1) is fully compatible with the well-established hybrid technique of
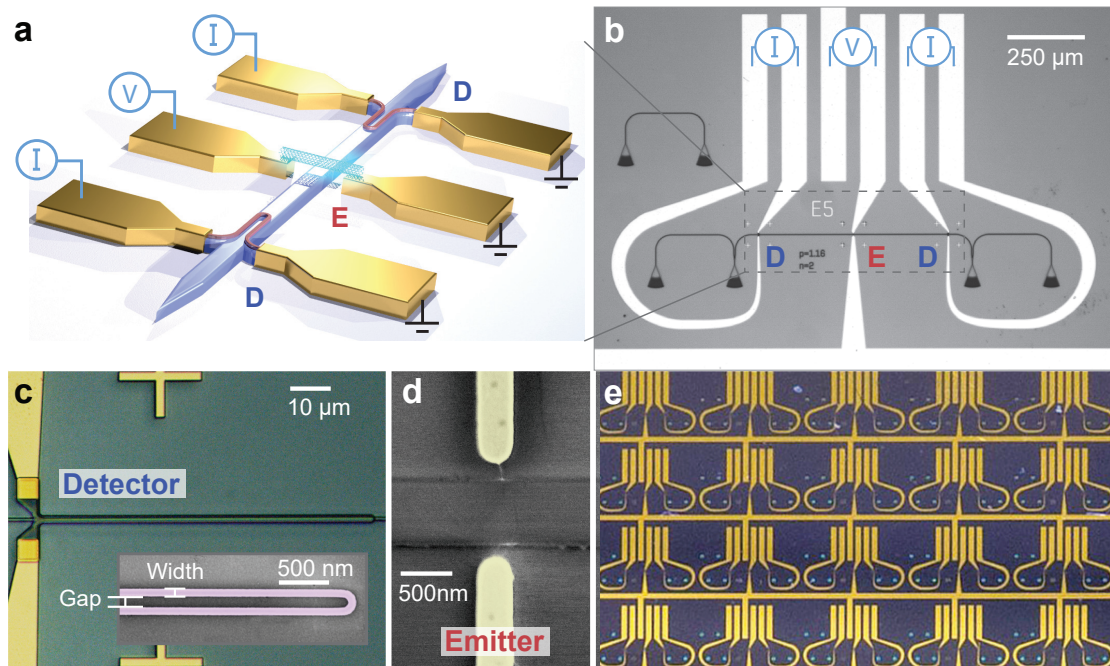
Figure 5.1: Design of the Hanbury Brown and Twiss (HBT) experiment on chip with a SWCNT-source. (a) Schematic view of electrically biased device with integrated on top of a waveguide SWCNT and two single-photon detectors. (b) Optical picture of of fabricated device with three pairs of metallic contacts. Emitter and detectors position are denoted with capital E and D. (c) Optical picture of detector and zoom of the meander end. Strip width and gap between two strips are denoted. (d) SEM picture of a single sc-SWCNT emitter on top of the waveguide in-between of two metallic contacts. (e) Optical picture of an array of devices combined by a common contact. *Source: adapted from* [57].

fabricating of photonic circuits. This helps to overcome the challenge of scalable combination of the single-photon sources and detectors. A highly efficient sorting method [90] to prepare suspensions containing SWCNTs with particular spectral characteristics (subchapter 3.2.2), along with the scalable deposition of single SWCNTs by dielectrophoresis (subchapter 3.2.3) allows for fabricating arrays of hundreds nearly identical sources (Fig. 5.1e). Both techniques manifest themselves as a highly preferable non-invasive integration techniques. All device components are driven purely electrically. The grating couplers at the ends of the waveguides (Fig. 5.1b) were used first for alignment purposes inside of the cryogenic setup. The second reason was to determine the detection efficiency upon illumination by an external laser. The inset (Fig. 5.1c) represents a U-shaped geometry with dimensions of 80 nm width and 100 nm gap between the nanowires. These dimensions were chosen based on previous studies of Si_3N_4 waveguide integrated detectors [127,128]. The optimization performed for a wavelength of 1550 nm revealed that the absorption coefficient α of a single U-shape NbN detector increases with nanowire width w and decreases with gap and wavelength, and so does its detection probability [129]. Also the waveguide width influences α with a peak value around 1000 nm [129]. This value of the waveguide width was used in the device layout with grating

couplers. Due to fabrication uncertainties, the NbN width and the gap size varied along the chip in the range of 70–90 nm and 90 nm to 120 nm, respectively. An optical picture of a detector with protective coating on top of the waveguide in-between the metallic leads is depicted in figure 5.1. Figure 5.2 shows an optical picture of a fabricated device (without grating couplers) and SEM images of the zoomed areas of the detector and source. The inset represents an AFM image of the nanowire's end (coated with resist) atop of the waveguide. The single-photon source ideally consists of only one sc-SWCNT to avoid multi-exciton generation.

5.1.1 Cryogenic setup

The second order correlation measurement on a SWCNT-based single-photon source was carried out in a cryogenic setup (Fig. 5.3a) to enable the operation of the superconducting detectors. In this environment, the chip position, electrical signals applied to the sample, and the temperature can be precisely controlled. Two different device designs were fabricated, consisting of the waveguides without and with grating couplers. The grating couplers enable the preparation of a large array of devices on a single chip, but at the same time they complicate the measurement, since an optical alignment is needed each time after moving to the next device. The device without grating couplers is wire-bonded, which simplifies the electrical connection procedure, but limits the number of devices that could be measured in a single cool-down cycle. Since the setup features only eight RF ports, the number of devices was consequently limited to four. The common ground electrode of the SWCNT-based sources were connected to the ground of the cryostat. Optical pictures of both kinds of devices are presented in Fig. 5.1 and 5.2, respectively. The sample without grating couplers was wire-bonded on a custom-built sample holder (Fig. 5.3c). The sample with grating couplers was placed on a nanopositioning system with XYZ and rotational stages (Attocube systems AG). An optical fiber array assembly, brought in close proximity to the chip surface, was used for the alignment. At the same time, a multi-contact RF Probe (Cascade Microtech) was brought in physical contact with the pads for electrical biasing and readout (Fig. 5.3b). No other optical access apart from the fiber array assembly is provided in this cryogenic setup. Therefore, the external laser source (TLB-6600, New Focus) at the wavelength 1550 nm, and a
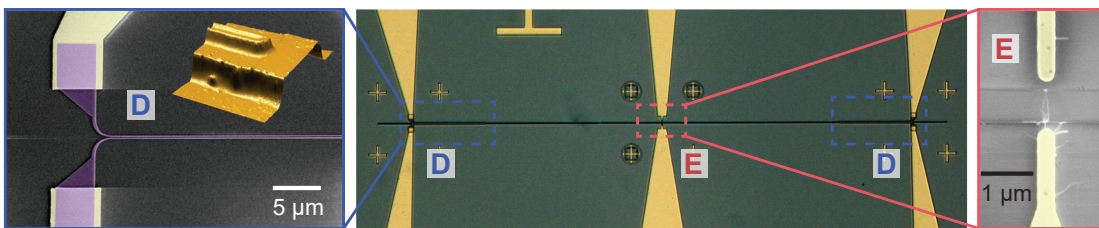
Figure 5.2: Optical picture of a fabricated device without grating couplers (middle). The zooms into the source and detectors areas denoted with colored lines. False-color SEM picture of a waveguide-integrated superconducting single-photon detector (D) (left). The inset represents a SEM picture of the nanowire end (coated with a protective layer) atop of the waveguide. SEM picture of sc−SWCNT source in the central device region (E) (right). *Source: adapted from supplementary to* [57].
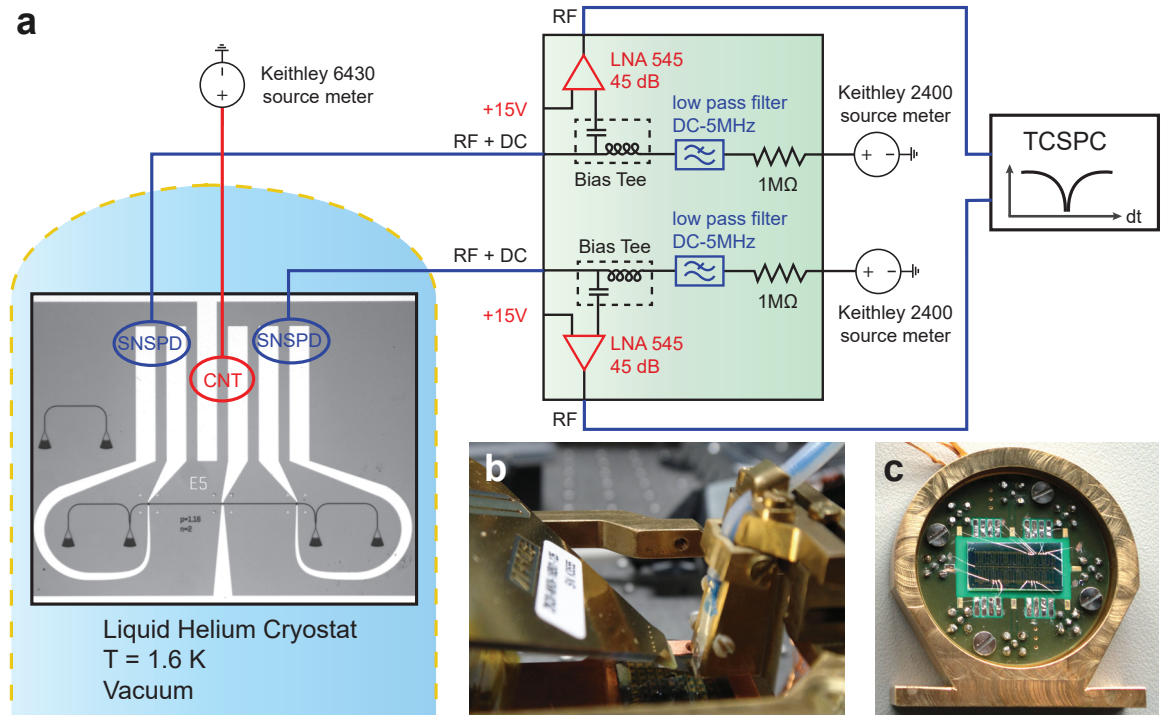
Figure 5.3: (a) Electrical connections of the cryogenic setup. SWCNT-source and SNSPDs are biased with constant voltage sources. (b) Optical picture of the sample with grating couplers under the fiber array assembly and RF-probe. The first provides an optical access, while the second is used for biasing and readout. (c) The sample without grating couplers was bonded on a holder for electrical wiring of source and detectors. *Source: adapted from* [57].

high sensitive power meter (HP 81635A) were used for alignment. The vacuum pressure in the sample chamber of the cryogenic setup was sufficiently low. A liquid helium flow cryostat was used to reach temperatures below 4.2 K. After pre-cooling with liquid nitrogen and cooling with liquid helium, a temperature in a sample chamber around 1.6 K was established due to controlled helium evaporation inside of the sample chamber and in the 1 K pot chamber. The SWCNT sources were driven by a DC-voltage source (Keithley 6430) with a pre-amplifier allowing for the precise current measurement in the fA range. The superconducting detectors were biased in a constant current mode by applying a constant voltage (Keithley 2400) over a resistor (1 MΩ) (Fig. 5.3a). The high frequency components of the bias current are filtered with a low-pass filter (BLP-5, DC-5MHz), additionally connected to the DC port of a bias tee. An incident photon breaks the superconductivity of the detector for a short time (tens of ps), after which the superconductive state recovers. But due to the kinetic inductance of the U-shape nanowire, governed by its geometry, the next photon can be detected only after several nanoseconds. The finite resistance causes a redistribution of the bias current to the external readout circuitry, which leads to a detectable voltage pulse. The latter is amplified by a low-noise RF amplifier (LNA-545 with 45 dB gain), connected to the RF port of the bias tee. These voltage pulses or clicks are then registered with a time-correlated

single-photon counter (Picoharp 300, Picoquant) or fast sampling oscilloscope (Infinium 6 GHz, Agilent). For counting with a TCSPC unit, a negative pulse amplitude, which is proportional to the DC biasing voltage of SNSPDs, was set. The appropriate trigger level of the counting system was determined. This was established by measuring the count rate (CR) in dependence of the trigger level at a constant bias voltage. For a low trigger level, compared to the amplitude of the click, the count rate appears to be higher than the count rate obtained from photoluminescence, because electrical noise is counted along with the real signal. With increasing trigger level, the low-amplitude noise does not contribute, and therefore, the measured count rate decreases. In a suitable trigger range, the observed count rate is equal to the expected photon signal rate. The trigger level was set to the middle of this range. Upon further increase, the measured CR reduces rapidly to zero if the trigger level surpasses the pulse amplitude. A typical value of the trigger level was in the range of 50–100 mV.
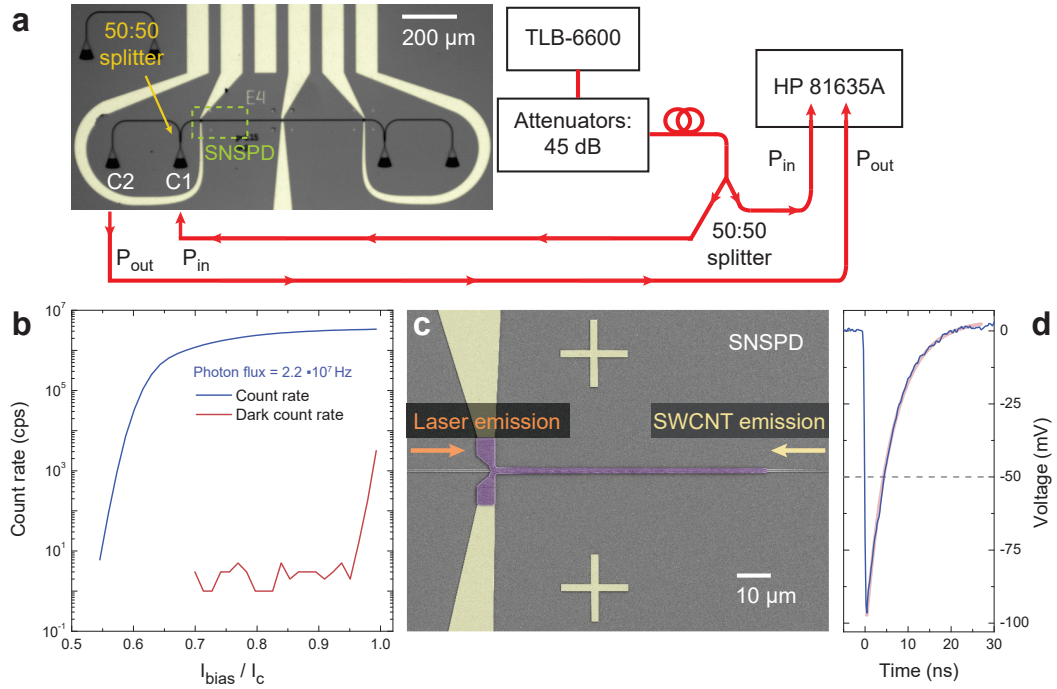
5.1.2 On-chip detection efficiency of SNSPDs

Waveguide-integrated SNSPDs provide efficient and fast detection of single photons, and represent a fundamental building block for integrated photonics at telecommunication wavelengths [88,127,130]. Their characteristics, such as efficiency and dynamic properties (jitter and dead time), can be tuned by their geometrical dimensions (the meander length, width and gap), as well as by the biasing conditions. A saturation of the on-chip detection efficiency (OCDE) ('plateau') is beneficial since it allows to reduce the bias current without affecting the OCDE. The detector noise is negligible (< 1 Hz) when operating the detector well below the critical current.

The detection efficiency of a SNSPD depends on the probability to absorb the incident photons in the NbN nanowire (which increases with the nanowire length) along with the probability that an absorbed photon forms a resistive state in this nanowire (which increases with decreasing width) [55]. The OCDE of the SNSPDs was estimated using a CW Laser (TLB-6600, New Focus) at a wavelength of 1558 nm, two optical attenuators (HP 8156A), and a power meter with two channels (HP 81635A) (see Fig. 5.4a). The photon flux at the detector was calculated with the following equation

$$\Phi = \frac{1}{2} \cdot \sqrt{\frac{2P_{\text{out}}}{P_{\text{in}}}} \cdot \frac{P_{\text{in}}^{\text{att}}}{\hbar\omega}$$

Here, P_{in} is the reference power, measured with the power meter. Assuming negligible differences in the losses in both arms of the external 50:50 power splitter, this value is equal to the input power on coupler C_1 (Fig. 5.4a). Our second assumption was the equal coupling losses on both couplers (C_1, C_2). P_{out} is the transmitted power measured using the power meter, $P_{\text{in}}^{\text{attenuated}}$ is the attenuated reference power, and $\hbar\omega$ is the photon energy at the given laser emission wavelength (1558 nm). An attenuation of 45 dB was used to reduce the photon flux to the SNSPD detectors, to avoid continual loss of superconductivity at higher count rates. The photon flux Φ at the presented SNSPD has a constant value of $2.2 \cdot 10^7 \frac{\text{photons}}{\text{second}}$. Fig. 5.4b shows the averaged count rate (blue) along with the dark count rate (red), as measured by

Figure 5.4: OCDE measuring scheme. (a) Device optical picture and external optical connections within the cryogenic setup for the estimation of SNSPD on-chip detection efficiency. (b) Count rate (blue) and dark count rate (red) measured with SNSPD in dependency on the biasing current normalized on a critical current of this detector. Constant photon flux is $2.2 \cdot 10^7$ Hz. (c) Colored SEM microphotography of a SNSPD device covered with a HSQ protective layer. The photons propagated from the left side are used to calculate the OCDE. (d) Negative voltage pulse (blue) due to loss of superconductivity and kinetic inductance of the nanowire with decay time ~ 10 ns, extracted from the single exponential fit. *Source: adapted from [57].*

the time-correlated single-photon counter (Picoharp 300). The count rate was plotted in dependence of the normalized detector bias current ($\frac{I}{I_c}$). The dark count rate was measured without laser light and with an attenuation of 120 dB. The count rate saturates on a log scale towards higher bias currents. The resulting detection efficiency η_{SNSPD} of the presented detector amounts to 13.6 %, when the detector was biased at 90 % of the critical current ($I_c = 25.6$ μA). This calculated value is relatively low in comparison to waveguide-integrated detectors of 80 nm width ($> 40\%$) [127], or a maximal value of the OCDE $\eta_{\mathrm{SNSPD}} = 70\%$ at $I = 61\% \cdot I_c$ measured for a similar detector geometry [131]. A possible reason is that by accessing the detector from the back side, the NbN meander branches might partly absorb and scatter the traveling mode and, hence, affect the detection efficiency. Therefore, we can estimate only a lower boundary of the OCDE, when back-illuminating the detector, while the real value of the OCDE might be higher.

5.1.3 Timing jitter and decay time

The SNSPD detectors show a low timing jitter of about 40 ps (FWHM) compared to commercially available avalanche photodiodes operating at room-temperature. The latter possess a timing jitter as high as 350 ps. Even smaller timing jitters (20 ps) are achievable with SNSPDs by increasing the nanowire width to 120 nm [132]. This is essential for measuring excitation lifetimes such as of SWCNT-based sources, which were estimated in our experiment to be < 150 ps. The overall system jitter also depends on the TCSPC jitter and is expressed as

$$\tau_{\text{system}} = \sqrt{2 \cdot \tau_{\text{SNSPD}}^2 + \tau_{\text{Picoharp}}^2} = \sqrt{2 \cdot 40^2 + 32^2}\,\text{ps} = 65\,\text{ps}.$$

Another important characteristic of SNSPD is the decay time, defining the maximal possible count rate that can be resolved by a detector. A decay time of 10 ns was measured for a detector with a width of 80 nm and a length of 80 μm, as shown in Fig. 5.4d. The decay time decreases from 12 ns to 5 ns when increasing the nanowire width from 60 nm to 120 nm [127]. The counting capability of SNSPDs with a decay time of 1–10 ns is in the range from 100 MHz up to 1 GHz well above the demonstrated emission rate of the SWCNT-source.

### 5.1.4 Measurement of the correlation function

We measured the correlation function in a Hanbury Brown and Twiss configuration. Two high-frequency outputs of SNSPDs were connected to the input channels of the TCSPC, which was operating in a histogram mode (start stop mode). The arrival times of the single photons triggering two detectors were recorded, subtracted from each other, and accumulated in a histogram by the counter. The minimal resolution of 4 ps, limited by counter hardware, was set for all measurements. The maximal count rate of a single channel of the Picoharp is approximately 10 MHz, since the time needed to perform the above mentioned operations ("dead time") is ~ 90 ns. This is the most significant limiting factor of the detection system, considering the much smaller "dead time" of the SNSPD (1–10 ns). It is possible to shift the center of the histogram from 0 to 45 ns, in order to measure a symmetrical curve with a negative time delay directly in the Picoharp software (up to 100 ns), without the need for an additional delay line. While the histogram resolution of 4 ps is established to resolve the antibunching dip, the maximal span of accumulated delay times was 260 ns. This was sufficient since the extracted electroluminescence decay times are less than 150 ps. Each measurement lasted from several minutes to several hours to resolve the antibunching dip. The accumulation time depends on the coincidence count rate. The minimal appropriate count rate on each detection channel is $\sim 10^4$ Hz, resulting in a coincidence rate of $10^2 - 10^3$ Hz. At lower count rates, the integration time for a histogram rose up to more than 10 hours, which is not suitable. Therefore, the second order correlation function was measured for count rates higher than $\sim 10^4$ Hz. Nevertheless, a bright single-photon source has to be realized, thus smaller count rates are not suitable.

5.2 Device efficiency

5.2.1 Conversion efficiency of the single-photon source

An important device parameter is the count rate N'. It represents the number of photons emitted by the source, coupled into the waveguide, propagated within the waveguiude toward detector and triggered a SNSPD. Therefore, we studied the electrical bias dependency of the count rate for different SWCNT-based devices. Although only sc-SWCNTs show distinct electroluminescence in the NIR region and therefore are relevant for application as a single-photon source, we employed also metallic SWCNT nanotubes in correlation experiments for comparison. The device conversion efficiency of the device with metallic SWCNTs was also estimated. The current and power dependency of the count rate is presented in a log-log plot (Fig. 5.5a, b). The count rate of the me-SWCNT device increases continuously with increasing power, revealing the typical behavior of incandescent emitters. The sc-SWCNT (Fig. 5.5a) starts to emit at higher voltages (but smaller currents) than me-SWCNT. Another important difference is that the count rate kinks around a bias voltage of 25–35 V which corresponds to a current of 3–11 nA (this kink is highlighted with * in Fig. 5.5a). Linear fits to the distinct regions in the electroluminescence plot (Fig. 5.5a) reveal a change from the super-linear regime with a slope of 1.4 to the sub-linear regime with a slope of 0.4. Several devices studied in this thesis show similar behavior, as can be seen in Fig. 5.5b. Similar to our results, a kink was observed also in a continuous wave photoluminescence in sc-SWCNTs [82]. The count rate reported in [82] (CW optical excitation) is plotted together with our data (Fig. 5.5b, visualized as stars). Here, the linear increase with slope 1 of the emission count rate with laser power (in a log-log scale) turned to the sub-linear range with slope 0.5. This can be explained by the change in average number of excitons, reaching unity at the kink. For pulsed optical excitation, the saturation of the count rate is observed at distinct power values [45,46], and no increase in the count rate can be observed at higher power. Hence, exciton-exciton annihilation (EEA) starts to play a crucial role [65,82] with increasing the power, because the average number of excitons along the nanotube is increased (subchapters 2.2.4, 5.3.1). The saturation behavior can be explained due to EEA dynamics, implying that the maximal density of excitons is reached at some specific excitation power [133]. During the short (femtosecond) optical pulse, several excitons are generated in the nanotube simultaneously at high laser power. The lifetime of the excitons is longer than 1 fs, so they coexist in the nanotube, diffuse along its axis, and encountering each other recombine non-radiatively due to EEA. Further increase of the laser power does not lead to higher count rates, because a higher number of coexisting excitons leads to a higher EEA rate. In case of continuous wave optical excitation higher power increases the rate of excitons generation, but due to randomness of pumping laser light the excitons in the nanotube are also generated randomly. So, the EAA rate is lower for CW excitation than during the laser pulse. Therefore, the count rate does not saturate, but kinks, like in our case, which is essentially "continuous wave" electrical excitation. So, we attribute this first kink to EEA.

In Fig. 5.5a after further increasing the electrical power, a second kink in the count rate can be observed at 50 nA (2 μW), past which the count rate increases linearly with a slope of 1.1. The second kink in the count rate was observed only in the electroluminescence
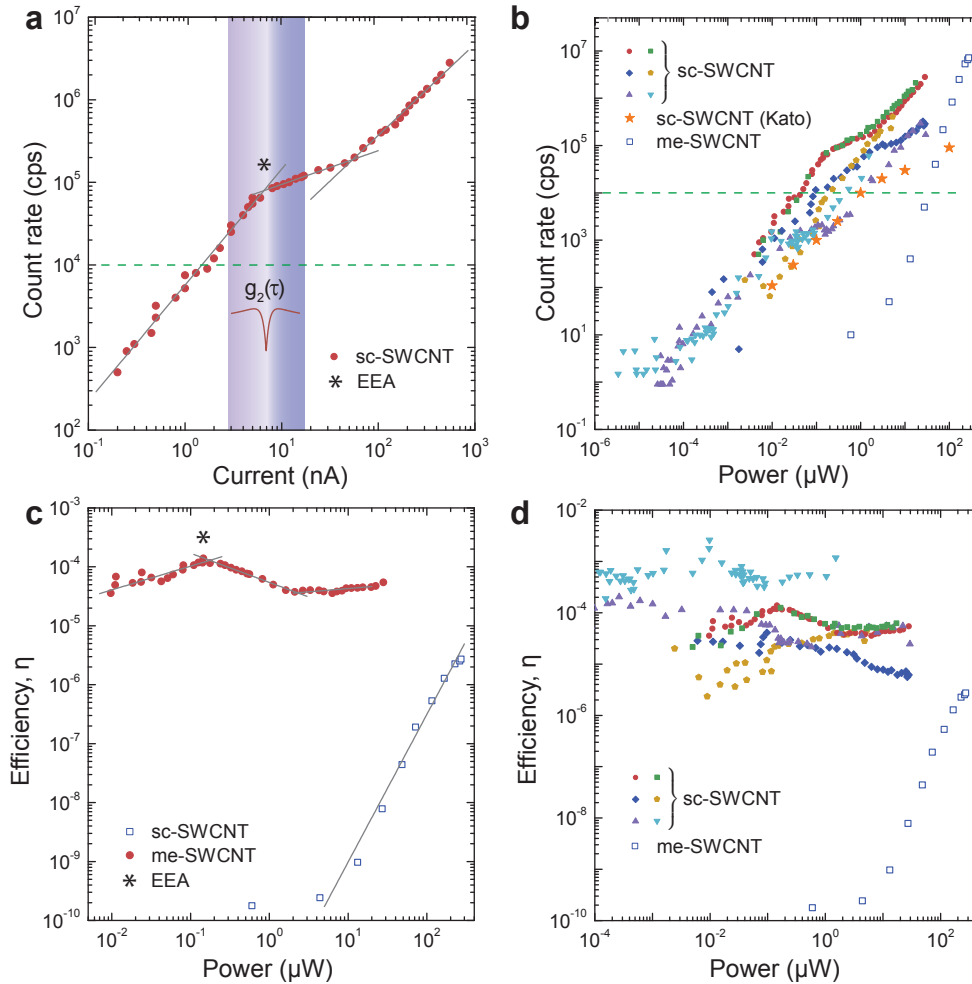
Figure 5.5: SWCNT source efficiency and count rate. (a) Count rate dependence on the current through sc-SWCNTs. The exciton-exciton annihilation (EEA) and non-classical regimes are highlighted. Linear fits with slopes 1.4, 0.4 and 1.1 at different biasing modes (gray solid lines) are plotted. (b) Count rate dependence on electrical power. For comparison, the count rate of an optically excited sc-SWCNT [82] is plotted (star symbol) along with our data. The count rate saturates at $1\,\mu W$ optical power. The green dashed line is an empirical minimal count rate level needed for the antibunching measurement. (c,d) Internal SWCNT-source conversion efficiency of semiconducting and one metallic nanotubes versus electrical power. Linear fits with slopes 0.4, -0.5 and 0.1 (gray lines) for sc-SWCNTs at low, medium and high biasing mode, along with a linear fit with slope 2.5 for a me-SWCNT at relatively high power (gray line) are plotted in (c). *Source: adapted from [57].*

experiments and can be attributed to additional incandescent emission, whose onset is located at high power similar to me-SWCNT. Nevertheless, the thermal emission in this power range, apparently, is not significantly high compared to electroluminescence, considering much larger slope (~ 3) of me-SWCNT emission.

By simultaneously recording the count rate N' along with the electrical current I_{SD} through the nanotube, the device conversion efficiency was estimated from the number of emitted photons per number of charge carriers (electrons and holes), driven through the sc-SWCNT:

$$\eta = \frac{N'_{\text{photon}}}{N'_{\text{carrier}}} = \frac{2N'/\eta_{\text{coupling}}\eta_{\text{SSPD}}}{I_{SD}/2e^-}.$$

Here, the detection efficiency η_{SSPD} of the respective detector is estimated with the procedure described in subchapter 5.1.2. The maximal coupling efficiency of the photons emitted by the source was estimated as 0.6 (4.2.1). Hence, the lower boundary of the conversion efficiency of the source yields

$$\eta \geq \frac{4 \cdot 1.6 \cdot 10^{-19}}{0.6} \cdot \frac{N'}{I_{SD}\eta_{\text{SSPD}}} \geq 10^{-18}\frac{N'}{I_{SD}\eta_{\text{SSPD}}}.$$

The conversion efficiency versus power for those devices whose count rate is shown in Fig. 5.5a, b is depicted in Fig. 5.5c, d. The value of the estimated conversion efficiency for sc-devices varies from 10^{-5} to $10^{-3} \frac{\text{photons}}{\text{carriers}}$, which is surprisingly high for nanotube electroluminescent emission. It is even several order of magnitude higher than for photoluminescence. The reason for this could be the difference in the mechanism of excitation by current, where each charge carrier is driven through the nanotube, while only a small fraction of photons provided by a laser is absorbed by the sc-SWCNT. This fraction is about $\sim 10^{-4}$ and is defined as focusing dependent laser spot size per nanotube size. The device conversion efficiency $\eta(P)$ plotted in Fig. 5.5c has a maximum value of $10^{-4} \frac{\text{photons}}{\text{carriers}}$ around 0.1 mW power, corresponding to the first kink in the count rate (Fig. 5.5a). As was explained above, we attribute this to EEA (marked with * in figure 5.5c), limiting the count rate and quantum yield of the electroluminescence. Such maxima were also observed in several other devices as shown in Fig. 5.5d (except for the sc-SWCNT marked with yellow pentagons and the metallic SWCNT). One of the sc-devices showed a surprisingly high device conversion efficiency of 10^{-3} at the maximum, before the onset of EEA reduces the quantum yield. This value is one order of magnitude higher than the quantum efficiency of an electroluminescent sc-SWCNT p-n-diode reported earlier [134].

The incandescent emission of the metallic devices turned out to be a less efficient process for photon generation, especially in the low and medium power range. Nevertheless, the me-SWCNT devices, measured in the cryostat, can be biased at much higher power due to low temperature and vacuum. Thus, a conversion efficiency of 10^{-6} was achieved at $P = 100\,\mu\text{W}$. This is a relatively high value of efficiency especially for an incandescent emitter. The conversion efficiency of the thermal emitter increases approximately as squared power $\eta \sim P^2$ (assuming $T \sim P$ and approximating the temperature dependence of a 1D thermal emitter as $\sim T^2$). The linear fit to the plot shown in Fig. 5.5c yields, however, a slope ~ 2.5 in a log-log scale. In comparison, the second kink in the count rate of sc-SWCNT emission

(Fig. 5.5a) corresponds to a point where the conversion efficiency grows slightly again, however with a slope of only 0.1. This can be explained by the additional contribution of thermal emission to the electroluminescence, which is, however, not so high. Further increase of the electrical power applied to our device would most probably lead to a behavior similar to incandescence but with higher slope, since at some point the thermal emission overcomes the electroluminescence. This is different from pulsed photoluminescence, where the efficiency continuously reduces in the high power range due to the saturation of the count rate. No further kinks in efficiency are observed also for continuous wave optical excitation [82,135].

The efficiency in the low bias range (prior to the first kink) seems to be proportional to $\eta \sim \sqrt{P}$, or $\sqrt{T}$, if we assume that the temperature is proportional to the electrical power applied to the sc-SWCNT. This is observed from the slope 0.4 in a log-log scale (Fig. 5.5c), which is higher than the one in photoluminescence experiments. A possible explanation is that this dependence originates from exciton diffusion through the sc-SWCNT, whose velocity is expressed by $v = \sqrt{\left(\frac{kT}{m}\right)}$, where m is the effective mass of the exciton. Hence, the exciton diffusion length increases with $\sqrt{T}$ [133]. This elevates the probability of an exciton which was created near a contact side, reaching a local trap, placed $0.5\,\mu m$ away from the contact on the waveguide during its lifetime, where a photon is emitted by radiative recombination.

We can assume that sc-SWCNT simultaneously emit electroluminescent and thermal light. Increasing the power, the SWCNT electron (and optical photon) temperatures also increase, and so does the thermal emission. Here it is important to note that the electron temperature T of the SWCNT is not equal to the acoustical photon temperature, which is responsible for the thermal flux into the substrate on the interface with the nanotube surface. Therefore, the temperature, extracted from the optical emission is not equal to the temperature of the underlying substrate. The latter remains in equilibrium with the thermal bath, hence, at several Kelvin. Therefore, it is important to estimate the SWCNT's temperature depending on the electrical power, since many effects in SWCNTs are temperature-depended (i.e. the EEA rate, emission decay time, and bunching due to the thermal component of light). In particular, the temperature in the power range where distinct antibunching was observed in our experiments is important to know. We fitted the count rate dependence on the power for metallic nanotubes (blue open squares in Fig. 5.5b) to an exponential law $\sim \exp\left(-E/kT\right) \sim \exp\left(\text{const}/P\right)$ [126], and the same dependence for sc-SWCNT (Fig. 5.5a) to the sum of $\sim \text{const}_{\text{EL}} \cdot \sqrt{P} + \text{const1}_{\text{th}} \cdot \exp\left(-\text{const2}_{\text{th}}/P\right)$. A temperature around $100\,K$ was found for a power around $0.15\,\mu W$. This value is on the same scale as the observations of Berger et al. [135], where the photoluminescence efficiency also experienced a maximum at $50\,K$, like in our observation of the maximum efficiency at $0.15\,\mu W$.

For the semiconducting devices, clear features of non-classical light (antibunching) were observed in the range of these efficiency maxima (presented in figures 5.8a-e and 5.9). For the remaining semiconducting devices (marked with yellow pentagons in Fig. 5.5d), no peak in the estimated quantum yield was observed. Consequently, only weak antibunching ($g^{(2)}(0) \geq 0.93$), suppressed by bunching, (Fig. 5.10a) was observed for this semiconducting device. As expected, metallic devices showed no antibunching in our experiment, and consequently can be used only as classical photon sources.

Concluding, the electrically-triggered sc-SWCNT device is an attractive highly efficient emitter in the visible and NIR spectral range. A long-time stable high-emission count rate of over 10^5 was achieved in a power range suitable for the generation of non-classical light.

## 5.2.2 Gate dependence of the source quantum efficiency

Additional improvement of the count rate of our source can be provided by implementation of a gate. The sample was realized on a p-doped Si substrate, which is used as an unibipolar [136] back gate. All devices were characterized at ambient condition prior to the measurements in the cryostat in order to determine the on-off ratio of the current at negative and positive gate voltage. Two presented semiconducting devices measured at ambient and cryogenic temperature (Fig. 5.6) show different behavior when switching from p to n conductance. In contrast to photoluminescent devices, the electrically triggered sc-SWCNT device performance (such as count rate and current) can be positively affected by applying a gate voltage. The electrically insulated silicon substrate was connected to an external DC power source (Keithley 2400). The conversion efficiency η of the sc-SWCNT source was measured under different constant gate voltages, varying the source-drain bias. The presented device shows pronounced antibunching which will be discussed later (Fig. 5.8). A clear maximum is observed in case of neutral, positive, and negative gate voltages (0 V, 100 V, and -100 V). Negative gating elevates the peak value of η by a factor of three and shifts it slightly to higher power, while a positive gate voltage doubles this value along with a peak shifted to lower power. Unfortunately, the effect of the gate appeared to be not stable over a prolonged period of time. Therefore, gating was not used during the measurements of antibunching, as these usually lasted several hours. However, an improvement in the gate structure, for example realization of a more sophisticated bipolar gating, can provide more control over stability and significant increase in brightness.
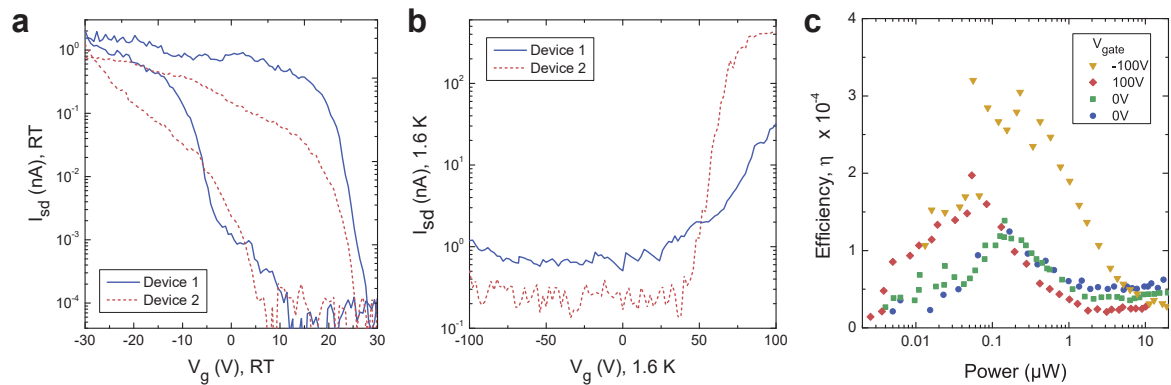
Figure 5.6: Transport characteristics of two devices (solid and dashed lines) at ambient (a) and cryogenic (b) conditions. (c) Electrical power dependence of the conversion efficiency η for the sc-SWCNT-device at various gate voltages. Distinct antibunching was measured this device (Fig. 5.8). *Source: adapted from supplementary to* [57].

5.2.3 Stability of the count rate emitted by sc-SWCNTs

A constant count rate over an extended period of time is an essential characteristic of a
stable single-photon source. A long-time stable count rate was observed in individual devices
between $1\,\text{kHz}$ and $10\,\text{MHz}$ for various electrical power ranges. A constant voltage of $30\,\text{V}$
(electrical power of $75\,\text{nW}$) was applied to the sc-SWCNT source presented in Fig. 5.7. As
was proven by the antibunching measurement, this SWCNT source emits non-classical light
in this power range. The photon arrival times of one detector were recorded in real time (T2
mode) and averaged over $100\,\text{ms}$ time bins (Fig. 5.7a). The data redistributed over $100\,\text{cps}$
bins are normally distributed and show a central average count rate and a standard deviation
of $7.8 \pm 1.6\,\text{kcps}$. Similar to this measurement, the count rate variation was recorded for
different power ranges. At a voltage of $40\,\text{V}$ applied to this SWCNT-source, a count rate
of $29.7 \pm 10.5\,\text{kcps}$ was observed on the same detector. The reason for the short term count
rate variation are fluctuations in the current through the SWCNT, which are up to $50\,\%$ of
the average value. This intensity variation is also a possible reason for the bunching effect
discussed below (sub-chapter 5.3.2).
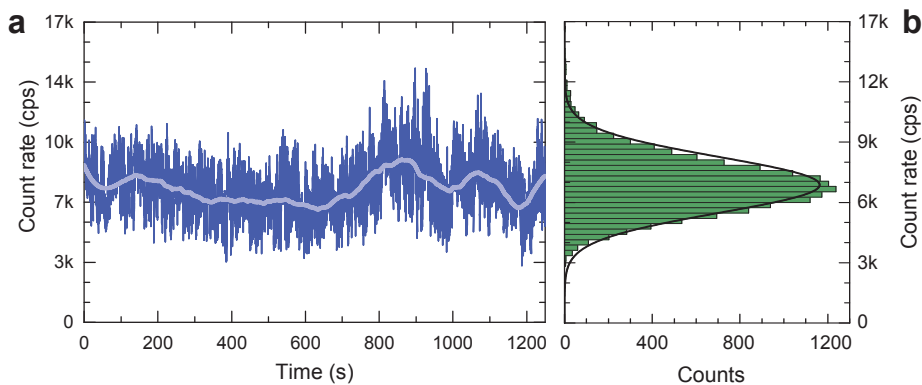
Figure 5.7: (a) Count rate stability over an extended measurement period. (b) Histogram showing
the normal distribution of the count rate. The average count rate is $7.8 \pm 1.6\,\text{kcps}$. The black line is
a fit with Poisson function. *Source: adapted from supplementary to* [57].

5.3 Measurement of non-classical light

In this chapter, the time-resolved spectra of non-classical light emission observed from electroluminescent SWCNT, as well as a possible explanation for its origin are discussed. The most probable reason for the generation of anti-bunched light is recombination of localized excitons (the bound optical states of an electron and a hole), which are trapped by the potential well, as was proposed for antibunching of SWCNTs, excited optically.

Concerning the optically excited non-classical light from sc-SWCNTs its studies are also still in their early stages. A comparison of experiments published so far is given in table 5.1, where the experimental conditions, such as temperature, laser power, the excitation mode (CW or pulsed), as well as utilized SWCNTs are given.

5.3.1 Exciton localization and exciton-exciton annihilation in SWCNTs

In general, in undoped nanotubes at high temperatures, multiple excitons coexist and, due to diffusion along the nanotube's axis with a diffusion length l_D, can encounter quenching sites (for example, the metallic contacts in our devices) and recombine non-radiatively. Naturally-induced localization potential wells are only a few meV deep. The temperature increase leads to increasing kinetic energy of the excitons (26 meV at 300 K), exceeding the potential barrier, so the exciton can easily leave the trap (chapter 2.2.4). At low temperature, the exciton is trapped in environment-induced 0D localization sites [139]. Therefore, antibunching was observed in supported undoped nanotubes [44] or in suspended undoped nanotubes [45] only under cryogenic conditions. Artificial defects, such as oxygen dopants [46], also act as localization centers for the excitons. Due to these induced defects, not only the emission yield was enhanced (up to 28 %) [45], but also single-photon generation in supported SWCNT at room temperature [46] was shown in case of photoluminescence. The localization also effectively suppresses emission blinking (due to non-radiative photoluminescence quenching) [45], a problem which photoluminescence of semiconductors often faces. Additionally, the bunching effects can be suppressed. Due to exciton localization, a stable and ultra-narrow photoluminescence emission with a high yield was established.

In the last decade it was confirmed that EEA plays a crucial role in exciton dynamics in carbon-based low-dimensional systems, like 1D carbon nanotubes or 0D quantum dots, where increased Coulomb interaction is significant. If two excitons are trapped at the same localization site, they are recombined non-radiatively. Therefore, although the emission intensity is reduced, the simultaneous emission of two photons, which is possible otherwise, is effectively suppressed by EEA. Hence, EEA supports single-photon generation in carbon nanotubes and can be controlled by the introduction of artificial defects. The saturation of photoluminescence emission towards higher excitation power, as well as power dependent photoluminescence decay times experimentally provided the evidence for EEA [45,123,140,141]. This is because the emission decay is dominated by a non-radiative EEA process for high power continuous wave excitation, where several excitons are generated simultaneously, and due to an increase of the diffusion rate with the temperature, the probability of annihilation is also increased [82]. The photoluminescence count rate saturation upon increasing the excitation power limits the potential brightness of the emitter. The exciton localization and

Authors	Högele[44,45]				Sarpkaya[137,138]		Doorn[46]	Maki[47]	Voisin	This work
Year	2013				2012	2013	2015	2015	2015	2016
T [K]	3-25				9		4-298	6-300	20	1.6
Excitation	PL				PL		PL	PL	PL	EL
Mode	pulsed	pulsed/ CW			pulsed		n/a	pulsed	pulsed	DC
CNT	CMC	CVD-grown	CMC		CMC	CVD	SDS-wrapped	CVD	CMC	HiPco
Chirality	(6,4)	mixed			n/a		(6,5)	(10,5)	n/a	sorted
Position	supported	suspended	supported		cavity	suspended	supported	suspended	cavity	WG-integrated
Power,P [µW]	0.5	kW/cm^2	50	3	$10-10^4$	n/a	n/a	0.2-2	n/a	0.08-0.3
Count rate	2kcps	kcps/µW	0.02	0.2	$1-500$ kcps	<1 kcps	n/a	n/a	n/a	60 kcps
Saturation			yes	yes	yes	n/a	n/a	yes	n/a	no
Lifetime, τ [ps]	$\tau_{1,2,3}=15,35,250$	3500	n/a	50	<2000	$<10^4$	50-570	$\tau_{1,2}=70,360$		80-160
τ (Power)	$\tau \sim 1/P$	$\tau \sim$ const	n/a		-		$\tau \sim 1/P$	$\tau \sim 1/P$	-	$\tau \sim 1/P$
$g^{(2)}(0)$	0.03	0.3	n/a	n/a	0.15-0.5		0.05-0.32	0.55-0.6	0.05	0.49
Bunching	n/a	no	n/a	yes	yes	no	yes	n/a	n/a	yes
Explanation	loc. excitons	localized excitons			n/a		loc. excitons	amorphous C		loc. excitons

Table 5.1: Comparison of antibunching experiments in photoluminescence of SWCNTs. n/a - information is not available.

EEA suppression leads to significant enhancement of the emission efficiency [45], even if the emission remains saturated.

In our experiment, a SWCNT is supported by metallic contacts at its ends and by a waveguide at its center, so there are two suspended parts in-between the ends. At cryogenic temperature, an exciton, which is most probably generated in the region close to a contact, diffuses towards the SWCNT center and is localized, for example, at the waveguide-air interface. At low power, the probability of generating a second exciton during the lifetime of the first one is small. At higher power at the point, where the probability of generating more excitons increases, a second exciton reaches the trap and non-radiative EEA occurs. This leads to a kink in the electroluminescence intensity, as was shown in Fig. 5.5a, b. Further power increase leads to generation of more excitons at a time, and hence to higher emission intensity, although the efficiency of this process is lower, due to increasing EEA rate. Also, the generation of thermal photons increases with power. This differs from photoluminescence, where the electron temperature increase with optical power is not so high ($T < 1000°$ for a typical power range). Varying the electrical power, the number of excitons and their temperature-depended diffusion length (so the decay time) can be controlled. This assumption has been proven experimentally.

5.3.2 Second-order correlation measurement

Antibunching

The second-order correlation function was measured in a series of devices at various electrical power levels in order to find the optimal biasing conditions for a SWCNT-based single-photon emission generation. A pronounced antibunching dip can be observed around the local maximum value of the conversion efficiency of the SWCNT emission (Fig. 5.5c, d), as discussed in subchapter 5.2.1. The lowest value of $g^{(2)}(0) = 0.49$ corresponds to the lowest power value of $0.08\,\mu W$, which was applied in the experiment. At even lower power the count rate was smaller than value of 10^4 cps, required for measurement. A value of $g^{(2)}(0)$ smaller than 0.5 is evidence for the non-classical nature of the light emitted by sc-SWCNT. This value also means, that the probability of multi-photon emission is halved compared to an attenuated coherent light source. With increasing power, the antibunching becomes weaker, until it vanishes completely at around $1\,\mu W$ power, which is correlated with a saturation in count rate and decrease of electroluminescent emission efficiency of the sc-SWCNT (subchapter 5.2.1). In the high power mode, incandescence contributes to the electroluminescent emission and, like in me-SWCNT, does not lead to antibunching at any high power. Some exemplary antibunching curves are shown in Figs. 5.8 and 5.9. Here the gray circles represent the measured data and the colored lines represent the respective reconvoluted second-order correlation functions obtained from the fit. The observed coincidence histogram data was normalized with the averaged signal at the limits of the time delay axis to obtain the second order correlation function $g^{(2)}(\tau)$, which tends to unity at large $|\tau|$. In the presented histograms the short-living non-classical emission accompanied by long-living bunched light is clearly visible. The horizontal dashed line represent the value of $g^{(2)}(0) = 0.5$ for convenience. The behavior of
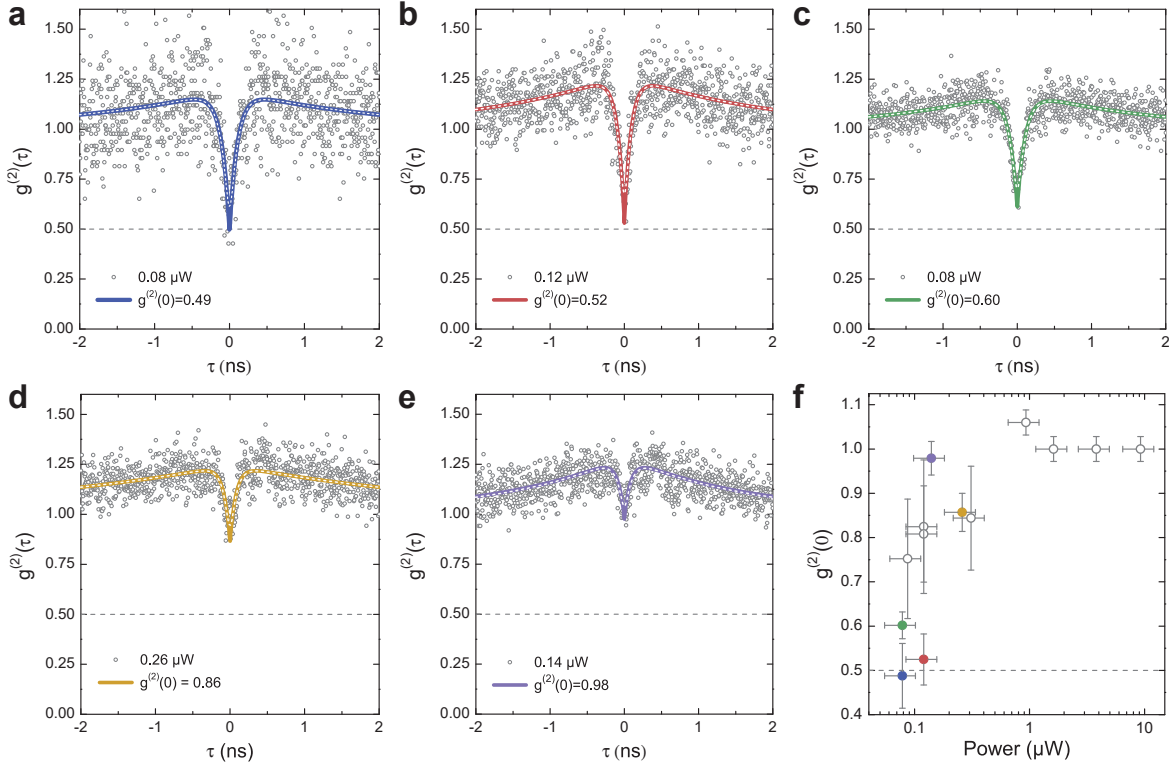
Figure 5.8: (a-e) Second order correlation function $g^{(2)}(\tau)$ observed in the same device at various the power levels (gray circles). Best fit of the convoluted function to the data (white dashed line) along with the reconvoluted function (colored solid lines). (f) Power dependency of the correlation amplitude at zero time delay $g^{(2)}(0)$. The extracted values from (a-e) are highlighted with the respective colors. The value of an antibunching dip equal to 0.5 is plotted with a gray dashed line. A source which shows $g^{(2)}(0) < 0.5$ is considered a single-photon source. *Source: adapted from* [57].

the correlation function can be described with a sum of two exponential decays:

$$g^{(2)}(\tau) = 1 - c_1 \exp(-\gamma_1|\tau - \tau_0|) - c_2 \exp(-\gamma_2|\tau - \tau_0|),$$

where γ_1 and γ_2 are the decay rates of the bunching and antibunching, respectively, and $c_1 < 0$ ($c_2 > 0$) are the amplitudes of these processes. τ_0 is the zero delay time. All plots are presented with $\tau_0 = 0$ for convenience, since the actual value of τ_0 depends only on the setup. The white dashed lines are the best fits of a convoluted function $F(\tau, x)$ (subchapter 5.3.4) to the data and the colored lines are the reconvoluted functions $g^{(2)}(\tau)$.

Bunching

Sub-microsecond bunching has been reported in several SWCNT antibunching experiments [45,46,137]. This bunching effect was associated with spectral wandering of photoluminescence, which also leads to line-broadening [45]. Such bunching on a longer time scale (than the excited state lifetime) is typical for any rapidly emitting source that exhibits blink-
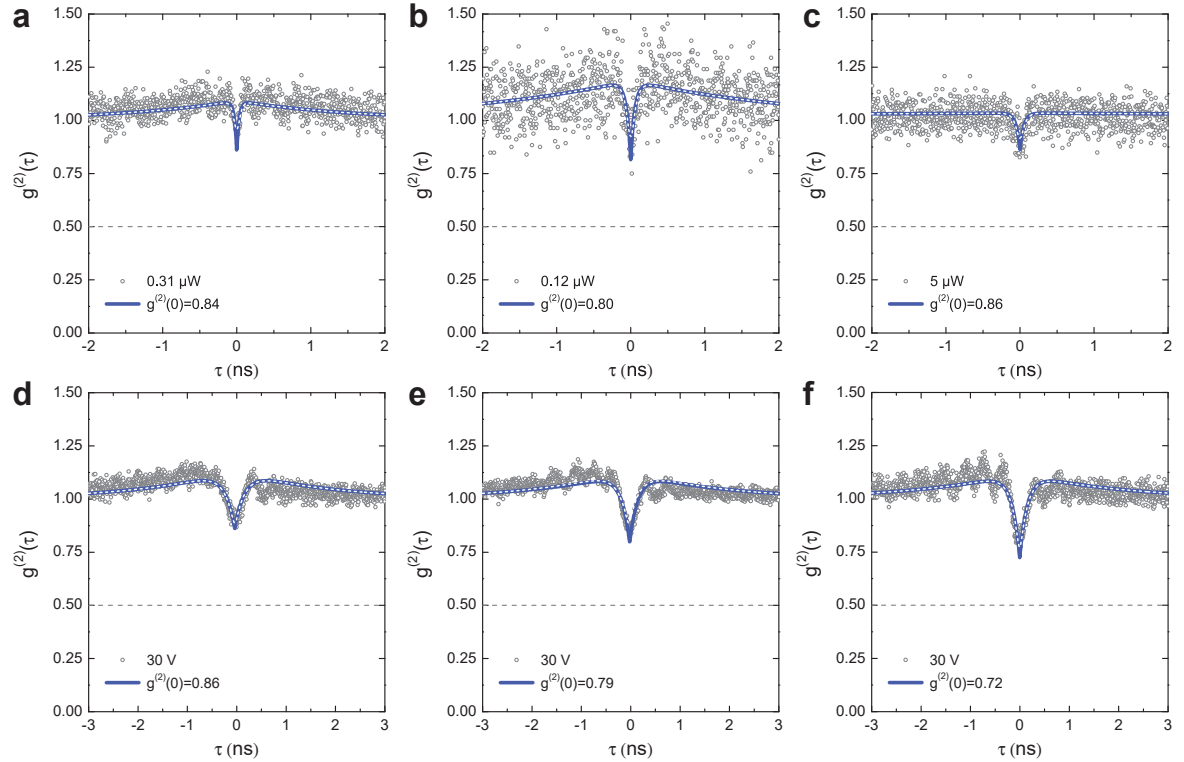
Figure 5.9: (a-b) Additional second order correlation function $g^{(2)}(\tau)$ measured (gray circles) in the same device as in the previous figure (5.8). The convoluted fit function (white dashed line) along with reconvoluted second-order correlation function (blue solid line). (c) $g^{(2)}(\tau)$ recorded on a second device with grating couplers during another cool-down. (d-f) $g^{(2)}(\tau)$ data measured on a third sample during another cool-down. The value of an antibunching dip equal to 0.5 is plotted with a gray dashed line. *Source: adapted from* [57].

ing [4]. The origin of the blinking and, hence, the bunching is the presence of an intermediate "dark" excitonic state in SWCNTs (and, for example, also in molecular single-photon sources). This "dark" state lies energetically lower than the optically active excitonic "bright" state. [133] Because of selection rules, the radiative transition from a dark state into the ground state with photon emission is prohibited in the one-dimensional excitonic picture (at least, in absence of a magnetic field). Thus, excitons transited into the dark state lower the emission rate, although the probability of excitation into the bright state is normally much higher than into the dark state. Therefore, many excitation emission cycles between the bright and the ground state are repeated, until the transition to the dark state occurs. [4] The excitons in a dark state not only lower the emission intensity, but also contribute to bunching. In contrast to one-dimensional excitons, zero-dimensional excitons localized in traps are free from this restrictions). Therefore, the localization leads to increasing of the exciton density and emission intensity. [142] Moreover, the bunching disappears if the excitons are localized in a deep potential well, as was shown by Hofmann et al. for naturally-induced defects in a suspended SWCNT, where non-radiative photoluminescence quenching and spectral

wandering are suppressed [45]. This results in a monoexponential photoluminescence lifetime of ~ 3 ns measured in suspended SWCNTs, as opposed to 100 ps in a supported carbon nanotube [44]. The lifetime in a nanosecond range is in good agreement with the theoretically predicted intrinsic lifetime of several nanoseconds $(1 - 10 \, \text{ns})$ [45].

The correlation function measured in our experiments shows clear bunching with an average extracted lifetime of 2.2 ± 0.8 ns. This bunching appeared in a large number of measurements in different devices without dependency on the applied electrical power and unrelated to the antibunching. The bunching might lead to instability in the spectral characteristics of the electroluminescence emission, like in photoluminescence, exhibiting blinking. Unfortunately, simultaneous measurement of the electroluminescence spectra was not possible with the implemented device layout. Another reason for the bunching might be thermal emission, since the bunching was also observed in metallic SWCNTs, where no antibunching was observed. The main disadvantage of sub-microsecond bunching is the elevation of the antibunching degree $(g^{(2)}(0))$ (Fig. 5.10a, b). The absence of correlation between the bunching and antibunching amplitudes can be seen in figure 5.10c. A pair of suitable amplitudes of bunching and antibunching results in $g^{(2)}(0) < 0.5$. The highlighted area (orange) illustrates a region with amplitudes, suitable for generation of non-classical light. Only one (blue) of the datapoints presented here falls into this range.
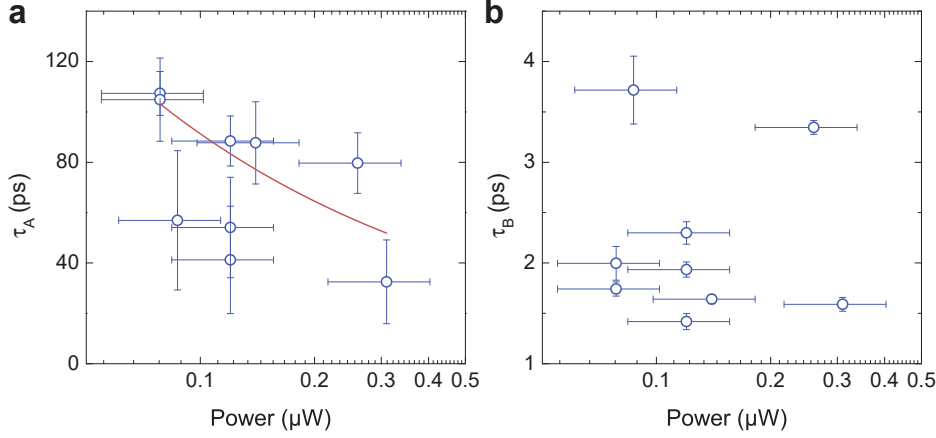
5.3.3 Decay time of SWCNT emission

The decay time (or lifetime) is the average time an exciton remains in the excited state, $\tau = \langle t \rangle$. It can be extracted from time-resolved fluorescence spectra in the approximation of an exponential decay process. The nanotube temperature and supporting environment change the decay rate significantly, therefore its dependence on the temperature and dielectric environment have to be studied, also because the decrease in the decay time has a strong
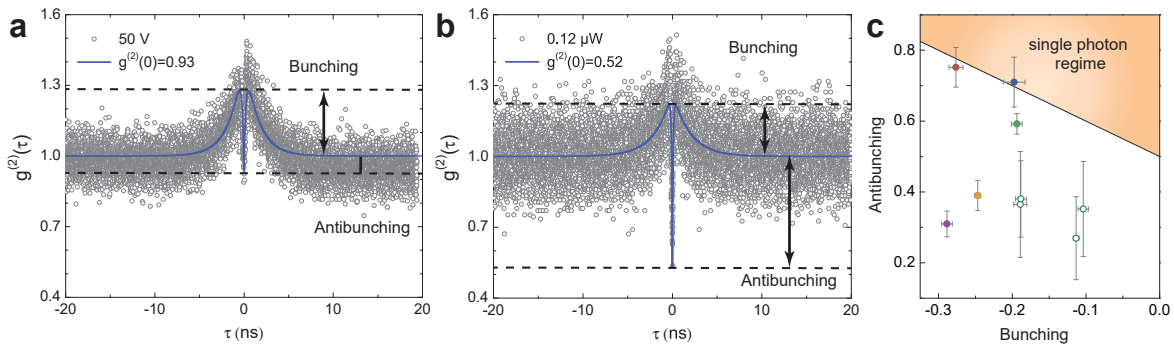
Figure 5.10: Second-order correlation function of two devices with $g^{(2)}(0) = 0.93$ (a) and $g^{(2)}(0) = 0.52$ (b). The presence of bunching significantly reduces the antibunching amplitude. The correlation function is normalized, therefore its value at larger $|\tau|$ is $g^{(2)}(\tau) = 1$. The amplitudes of bunching and antibunching are denoted with an arrows respective to this value. The antibunching dip and bunching peak values are designated with dashed lines for clearance. (c) Correlation between bunching and antibunching amplitudes, extracted from the fit to the second-order correlation function, which was measured in the same device under various bias voltages. *Source: adapted from* [57].

influence on the antibunching dip. If several excitons recombine radiatively along the tube, the decay time is averaged over the exciton ensemble. The decay time τ is defined as the inverse of the decay rate $\gamma = \Gamma + k_{\mathrm{nr}}$ (chapter 2.2.4), which is the sum of radiative (Γ) and non-radiative (k_{nr}) decay rates [123]. The temperature dependency of the radiative decay is predicted by ab-initio calculation [143] as $\tau = 10\,\mathrm{ns}$ at room temperature, increasing with decreasing temperature. A lifetime in the nanosecond range is also theoretically calculated for nanotubes with small diameter ($\sim 1\,\mathrm{nm}$) [144]. The presence of the substrate has a noticeable impact on the PL lifetimes. The decay time of SWCNTs on substrate is reduced by an order of magnitude compared to suspended SWCNTs [45]. This behavior is expected due to the surrounding with higher photonic density of states compared to suspended nanotubes ($n_{\mathrm{Si_3N_4}} = 1.98$, $n_{\mathrm{air}} = 1.0$) and can be attributed to fast non-radiative decay of non-localized excitons on quenching sites [44]. A similar picture was observed in an antibunching experiment with a WSe$_2$ monolayer supported by SiO$_2$/Si or h-BN/SiO$_2$/Si in comparison with a freestanding structure [26]. The exciton size has a direct effect on the exciton oscillator strength and hence the radiative lifetime [145]. In a 1D nanotube, the oscillator strength of a mobile exciton is inversely proportional to the exciton size $f \sim 1/L$, which is approximately $1\,\mathrm{nm}$ at room temperature [81]. Also, the lifetime depends on the coherence length in the 1D nanotube, which is affected by the temperature T and also by the nanotube length, as well as the photon wavelength, if the coherence length is sufficiently large [145]. The inverse dependency of the radiative lifetime on the temperature $\tau \sim 1/\sqrt{T}$ was found even earlier for 1D semiconducting structures [146]. Phonon scattering limits the radiative lifetime due to reduction of the coherence length, making it shorter than the photon wavelength [144], especially for supported nanotubes. A similar inverse behavior was shown in multiple experimental studies. Doorn et al. [46] measured a decrease in the lifetime from $500\,\mathrm{ps}$ to $200\,\mathrm{ps}$ for PL in supported polymer-wrapped nanotubes, along with distinct antibunching. In further experiments of Högele [44] and Maki [34], time-resolved photoluminescence, measured with TCSPC technique could be fitted to the sum of two exponential decays. One of them is a temperature-dependent long-live decay and second one is a short-live decay which does not changed with the temperature. Equivalent results were also shown by Berger et al. [135]. An increase in the excitation power leads to a similar dependency of the lifetime as the temperature rises. This is evidence for an increase in nanotube temperature, which occurs due to optical excitation [47].

While the decay time of photoluminescence gained a lot of attention in the last years, the lifetime upon electrical excitation has not been studied yet, but apparently has to reveal similar behavior as for photoluminescence. The decay time of incandescent emission of single SWCNTs as well as nanotube films under electrical current was shown in chapter 4 with a shortest decay time of $80\,\mathrm{ps}$ (setup-limited). In the antibunching experiment discussed in the current chapter, the electroluminescence lifetime of a single SWCNTs was extracted from the fit to the data, obtained from the second-order correlation measurements. A slight decrease of the radiation lifetime was observed when increasing the electrical power. The data was fitted to the $a/\sqrt{P}$ law (discussed in chapter 5.2.1), concerning the proportionality between the applied power P and temperature T for a one-dimensional system. An approximately halved decay time from $100\,\mathrm{ps}$ to $50\,\mathrm{ps}$ was observed when increasing the power from $0.08\,\mathrm{\mu W}$ to $0.3\,\mathrm{\mu W}$ (Fig. 5.11). The decrease of the lifetime can be explained by an additional non-radiative depopulation rate of the excited state, which increases with the temperature [123].

Figure 5.11: Decay times dependence of sc-SWCNT-emission on the applied electrical power for antibunching (a) and bunching (b). The y-error bars are given as a standard deviation of the fitted parameter τ_A or τ_B, respectively, while the x-error bar is $30\,\%$ of the respective power value. The solid red curve in (a) is the fit to the $a/\sqrt{P}$ law, with $a = 29\,\text{ps} \cdot \sqrt{\mu\text{W}}$. The average values of the antibunching and bunching time decays are $\tau_A = 72\,\text{ps}$ and $\tau_B = 2.1\,\text{ns}$. *Source: adapted from* [57].

5.3.4 Reconvolution of the second-order correlation function

The excited state lifetime which was measured in our second-order correlation experiment is on the same time scale as the timing uncertainty of our system (tens of ps), and hence, is strongly affected by it. Moreover, the second order correlation function at zero time delay (the most important characteristic of photon sources) is significantly elevated compared to the real one, if the lifetime to timing uncertainty ratio is too small. The counter and, moreover, the detectors exhibit a timing uncertainty, corresponding to the variation of the detector signal upon photon absorption. The timing jitter of the detectors, used in this experiment, is about 40 ps. This value is an inherent property of the detector and varies with different nanowire geometry and biasing conditions. That means that each data point has a Gauss-distributed error along the time axis, expressed by a function

$$G(\tau) = \frac{1}{\sqrt{2\pi}\sigma} \cdot \exp\left(-\frac{\tau^2}{2\sigma^2}\right).$$

The FWHM of this distribution defines the timing jitter of the whole system τ_{system}, and $\sigma = \frac{\tau_{\text{system}}}{2.3548}$ is the standard deviation. In case of two SNSPDs with a jitter $\tau_{\text{SNSPD}_{1,2}}$ and a counter with τ_{counter}, the overall timing error (FWHM) can be defined as

$$\tau_{\text{system}} = \sqrt{\tau_{\text{SNSPD}_1}^2 + \tau_{\text{SNSPD}_2}^2 + \tau_{\text{counter}}^2},$$

which in our case has a minimal value of $\sqrt{40^2 + 40^2 + 32^2}\,\text{ps} = 65\,\text{ps}$. To obtain the "real" and not deconvoluted data, a reconvolution procedure has to be performed. The same method is applied in fluorescence spectroscopy in the time domain to obtain the "real" lifetime. In the latter case, the instrument response function can usually be directly measured using the

same setup, instead of approximation with a Gauss function. For example, the detector is illuminated with the reflected light of a femtosecond-pulsed laser, used for excitation. In our case a light source, electrically driven with ultra-short pulses and with a lifetime well below the SWCNT electroluminescence lifetime, has to be used. But, as was explained in chapter 4.3, concerning the SWCNT lifetime of tenths of ps, commercially available sources are still too slow. The deconvoluted function

$$F(\tau,x,\sigma) = 1 - \sum_{(j=1,2)} \frac{c_j}{2} \exp(\frac{\sigma^2 \gamma_j^2}{2} - \gamma_j|\tau - \tau_0|) \cdot [\mathrm{erfc}(z_{j,-}) + \exp(2\gamma_j|\tau - \tau_0|) \cdot \mathrm{erfc}(z_{j,+})],$$

with parameter set $x = [c_1,c_2,\gamma_1,\gamma_2,\tau_0]$ and $z_{j,\pm} = (\sigma^2\gamma_j \pm |\tau - \tau_0|)/\sqrt{2\sigma^2}$ was used for fitting the measured data. Here, an error function (erfc) is used to simplify the expression. The right part of the equation represents the measured data and can be directly fitted to obtain the five parameters in x.

To estimate how the ratio of the lifetime to τ_{system} influences the measured $g^{(2)}(0)$ value, the deconvoluted function $F(\tau,x)$ was calculated at $\tau = 0$ while varying the parameters in x (Fig. 5.12). The value of $F(0,x)$ is the dip, measured in the antibunching experiment. As can be seen from this calculation, for ratios of $\frac{\mathrm{lifetime}}{\tau_{\mathrm{system}}} > 4$ the convoluted value of $g^{(2)}(0)$ approaches the real amplitude of the second order correlation function. For the fitting procedure of the measured data we used the least-squares procedure (MATLAB Optimization and statistic Toolbox) based on the Levenberg-Marquardt algorithm, which allows an error estimation of the fitted parameters shown in table 5.2. All the histogram data in this table was measured on the same device under various electrical power. For the initial guess a parameter range c_1=-0.2, c_2=0.5, $\tau_1 = 1$ ns, $\tau_2 = 100$ ps, and $\tau_0 = 45$ ns was chosen. The iterations were repeated until the fit converged up to the fifth significant digit. The covariance matrix Cov of the fitted parameters was calculated to define the standard deviation σ_x of
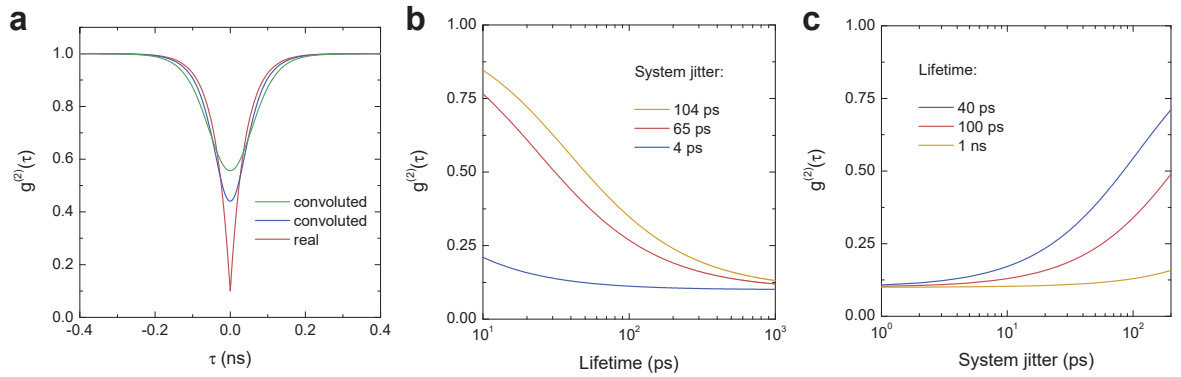
Figure 5.12: (a) Deconvoluted correlation function for a lifetime of 40 ps (red). Convoluted functions with the system jitter (FWHM) 65 ps (blue) and 104 ps (green). (b) The value of the convoluted function $F(0,x)$ for varied system jitter: $\tau_{\mathrm{system}} = 4$ ps (blue), 65 ps (red), and 104 ps (orange) with respect to the lifetime. (c) $F(0,x)$ in dependence on the system jitter and the lifetime: 40 ps (blue), 100 ps (red) and 1 ns (orange).

Power (µW)	c_1	c_2	τ_1 [ns]	τ_2 [ps]	τ_0 [ns]	$g^{(2)}(0)$
0.08	-0.198±0.014	0.710±0.070	1.995±0.167	0.104±0.017	45.033	0.487±0.073
0.08	-0.193±0.007	0.592±0.029	1.742±0.070	0.107±0.009	45.022	0.602±0.030
0.09	-0.104±0.007	0.352±0.134	3.716±0.337	0.057±0.028	45.03	0.752±0.135
0.12	-0.276±0.009	0.752±0.056	1.934±0.075	0.088±0.009	45.027	0.525±0.057
0.12	-0.188±0.007	0.380±0.107	2.298±0.111	0.054±0.020	45.041	0.808±0.108
0.12	-0.189±0.009	0.365±0.149	1.418±0.080	0.041±0.080	45.017	0.824±0.151
0.14	-0.289±0.007	0.310±0.036	1.641±0.045	0.088±0.016	45.044	0.980±0.038
0.26	-0.247±0.004	0.389±0.042	3.345±0.069	0.079±0.012	45.034	0.857±0.043
0.31	-0.113±0.004	0.269±0.117	1.589±0.068	0.033±0.017	45.045	0.844±0.117

Table 5.2: Decay times and amplitudes of antibunching and bunching, obtained from a fit of the measured coincidence histograms.

each parameter.

$$\mathrm{Cov} = \frac{1}{N-5}(J' \cdot J)^{-1}(R \cdot R'),$$

where the Jacobian J and the residual R are $N \times 5$ and $1 \times N$ matrices, respectively. σ_x is obtained from the square root of the diagonal elements $\sqrt{\mathrm{Cov}_{i,i}}$, and the standard deviation of the degree of second order correlation ($g^{(2)}(0)$) is given by $\sqrt{\mathrm{Cov}_{c_1,c_1} + \mathrm{Cov}_{c_2,c_2} + \mathrm{Cov}_{c_1,c_2}}$.

The data, given in this table are used for figures 5.8f, 5.10c, and 5.11. No dependency between bunching and antibunching amplitudes was observed. The antibunching decay time varies in a range of $33 - 107\,\mathrm{ps}$, where the exact values slightly depend on the fitting accuracy.

Conclusion

The non-classical light generation of electrically driven single waveguide-integrated sc-SWCNT was shown for the first time. Scalable integrated single-photon sources and detectors on a common photonic platform exhibit high overall device efficiencies. The degree of second order correlation below 0.5 was observed when performing a Hanbury Brown and Twiss experiment on-chip, which clearly proves the sc-SWCNT as a single-photon source. In the count rate dependency on power, three distinguishable operation modes were observed. The low bias range exhibits the squared root of the temperature dependency of the emission efficiency. The transition to the medium power range can be attributed to the onset of exciton-exciton annihilation (EEA) and the transition to the high biasing mode is attributed to a thermalization effect. Therefore, the role that exciton-exciton annihilation plays in the single-photon emission of electrically driven SWCNT should be further investigated. The localization of excitons in a zero-dimensional trap can help to increase the lifetime of excited states and decrease the non-radiative recombination rate, which limits the source brightness due to end quenching. Furthermore, it will improve the photon statistic by decreasing the probability of simultaneous recombination of spatially separated excitons, which was shown in the photoluminescence experiments. Artificial defects like a SiO_2 strip, which can be

easily realized by an additional lithography step, open the opportunity for the realization of deterministic SWCNT-based single-photon sources, which are highly searched after. The selective placement of these defects on top of the waveguide might further increase the coupling efficiency. Also, electrostatic traps can be used for exciton localization [45]. The mechanism underlying the power dependency of antibunching and emission efficiency in EL should be studied more intensively. The electrical gate provides an additional possibility of exploring this, in contrast to PL.

6 Conclusion and outlook

The results of this thesis are based on successfully merging two well-studied nanoscale platforms - single-walled carbon nanotubes (SWCNTs) and nanophotonic integrated circuits. This allows the combination of various linear optical elements with on-chip carbon-based non-classical sources and integrated singe-photon detectors. In this thesis, we have demonstrated the emission of classical and, for the first time, non-classical light from electrically driven single-walled carbon nanotubes, integrated into nanophotonic circuits. The electrical control of the emission establishes carbon nanotubes for the next device generation of scalable on-chip sources, that can be seamlessly integrated with passive silicon photonic technology for on-chip communication.

Various hybrid SWCNT nanophotonic devices were presented as fundamental building blocks for potential application in carbon-based linear optical quantum computing. For example, power splitting with a ratio of 1:1 was realized on the basis of a directional coupler. Spectral modulation of the emission from a carbon nanotube coupled to the on-chip Mach-Zehnder interferometer was presented. Placement in a nanobeam photonic crystal cavity provides the tuning of the emission for the electrically-driven SWCNT source with a tunable tiny spectral range. Also, adjusting of the broad-band incandescent SWCNT emission spectra was demonstrated.

Exceptionally high thermal conductance, small sizes, and the seamless integration into nanophotonic circuits proves SWCNTs as an ideal candidate for nanoscale electro-optical modulators. Devices with dense films of metallic carbon nanotubes, several metallic nanotubes, and single semiconducting nanotubes were studied for comparison. Time-resolved optical emission spectra upon the pulsed electrical biasing were recorded from each device employing the time correlated single-photon counting technique. The electrical pulse width varies in the range of 150 ps–200 ns, while the period ranges from 0.2 µs to 1 µs. High thermal conductivity along the nanotube axis leads to ultra-short decay times of the electrically-induced emission. With the initially employed single-photon avalanche detector the optical pulse width was limited by its low timing resolution of ~ 350 ps. After implementing a detector with a higher timing resolution of ~ 40 ps a decay time of 80 ps was extracted from the exponential fit to recorded time-resolved incandescence. The maximal frequency of the signal transmitted within the waveguide potentially could be increased up to 12.5 GHz, which follows from the estimated decay time value. However, due to experimental limitations the maximal realized frequency of the electrical signal, and hence, of the optical emission was 2 GHz in supported SWCNTs. Because of the thermal nature of the detected emission (and other limitations), no difference in the decay times of the semiconducting and metallic SWCNTs was observed. The electron temperature was estimated from the wavelength-resolved spectra and lies in the range of 1000–1500 K. Using these values as the boundaries we estimate the decay time for thermal emission to be in the range of 5–70 ps, which corresponds to potential light frequencies in

the 100 GHz range. Nevertheless, the value of 2 GHz demonstrated in our experiment is the highest so far for waveguide-coupled emission from carbon nanotubes.

We observed non-classical light emission from single-walled semiconducting carbon nanotubes (SWCNTs), operating in the electroluminescent mode at cryogenic temperatures. This electrically-driven source was embedded within a photonic circuit along with two single-photon traveling-wave detectors. These detectors are made of superconducting niobium nitride nanowire atop the photonic waveguide. SNSPDs were irreplaceable for our experiment due to their remarkable characteristics such as high efficiency, low dark counts, and high timing resolution. The high detection efficiency of SNSPDs results in high overall device efficiency. The small timing jitter ($< 50\,\mathrm{ps}$) allows for accurate measurement of the lifetime of a single emitter, which is a combination of intrinsic radiation lifetime, dephasing time and the timing resolution of the detector. A recovery time of several nanoseconds allows for detection of bright emission with high count rates. Thus, we realized a fully-integrated hybrid quantum photonic device with SWCNT-based single-photon source and detectors, which can be scaled up easily. Through purely electrical control and self-assembly of the SWCNTs, the essential problem of scalability of the sources is overcome. Hence, external optical excitation and sophisticated optical filtering are not needed. An implementation of SWCNT-based single-photon sources as key active element in a circuit promises intriguing perspectives for on-chip quantum photonic applications.

A maximal count rate for single-photon emission was found to be $\sim 10^4\,\mathrm{cps}$ in a power range of $0.1 - 1\,\mu\mathrm{W}$, corresponding to a device specific voltage range of $30 - 35\,\mathrm{V}$. If the SWCNT source is operated at higher power, the bunched thermal emission starts to play a significant role and can even dominate the single-photon emission. Therefore, although higher count rates are reached, the antibunching is suppressed due to thermal emission.

The electroluminescence intensity can be enhanced by additional application of a gate voltage. A regime can be found in which the electrical power is low and, hence, thermal emission is suppressed, while electroluminescence is still efficient. This is an advantage of an electrically-driven SWCNT-based single-photon source, in comparison to optical excitation. In the latter case only the impact of laser power and ambient temperature on the emission characteristics can be studied, while for electrical pumping the count rate and antibunching depth can be additionally controlled by the gate. As an outlook for this thesis, where only source-drain voltage dependencies of the count rate and antibunching were investigated, the SWCNT single-photon source properties have to be studied also in dependence on the gate voltage.

The indistinguishability of SWCNT-based single-photon sources have to be shown yet. Although, it is expected for an emitter with ultra-narrow spectral line, which is typical for emission from suspended SWCNTs at cryogenic temperature. Single SWCNT-based emitter, hovever, have to possess an identical chirality. In case of relatively broadband electroluminescence of the SWCNT, emitter can be placed in a photonic cavity. The latter can couple and enhance a particular optical mode with a high quality factor, providing an optical filtering of desired wavelength. We have demonstrated such coupling to a nanobeam photonic cavity. In this thesis, it has been employed to cut the broad-band thermal emission spectrum. However, it can also be used in case of electroluminescence. The central wavelength of the resulting narrow-band emission can be tailored with adjustment of the cavity geometry.

It is important, to understand the origin of electrical-induced non-classical emission from SWCNT. A possible origin of the generation of non-classical light in electroluminescent SWCNTs is the recombination of excitons localized in trap sites. The most probable mechanism of electroluminescence is an impact ionization and the devices reveal the properties of a p-type unipolar field-effect transistor. One can imagine that the exciton creation occurs close to one of the electrodes with subsequent diffusion towards the nanotube center and recombination at the air-waveguide interface. Exciton-exciton annihilation in a trap, which supports the single-photon emission while limiting the brightness of the source, plays a crucial role in one-dimensional nanotubes. For the excited state a lifetime of about 80 ps was estimated. It can be concluded, that the excitons recombine in the vicinity of the waveguide, because an intrinsic lifetime of suspended nanotube is on the nanosecond range.

Although the role of exciton-exciton annihilation as an enhancing factor of single-photon emission from SWCNT has to be further investigated, some conclusion can be drawn. It was shown that the single-photon emission is most efficient in the power range, in which more than two excitons are produced and annihilate non-radiatively, which elevates the probability for single photons to be emitted.

To extend our results, a study of near-infrared spectra of SWCNT-induced electroluminescence has to be performed. These spectra have to be recorded at ambients condition, for example, in the free-space setup, as well as in a cryostat to support the results of the correlation experiment. Additionally, instead of the simple but uncontrollable beam splitting, implemented in our current design, a directional beam splitter can be employed. The coupling to this element has already been shown in this thesis.

A Appendix

In this chapter the techniques and recipes which were utilized to prepare samples for performed experiments are described in detail in the first part. In the following part, the measurement setups are presented.

A.1 Fabrication techniques

Chemical cleaning of substrate: All substrates have to be cleaned before resist spin-coating for better adhesion and thickness homogeneity. For this purpose, all samples were ultrasonicated in acetone for 5 minutes at medium power and room temperature. Then the samples were rinsed in isopropanol for one minute and dried with a nitrogen gun.

Spin-coating of PMMA resist: The substrate is baked on a hotplate for 5 minutes at 100 °C for improved adhesion. Directly after that 80 µl of PMMA 4.5 resist is spin-coated on the surface at a speed of 4000 rpm with an acceleration of 1000 rpm/s for 90 s. Then the substrate is baked again on the hotplate for 3 minutes at 100 °C for removing the residual solvent. The layer thickness measured after the baking by means of thin-films interferometry (Filmetrics) is around 250 nm.

Spin-coating of ma-N 2403 resist: The substrate is baked on a hotplate for 5 minutes at 100 °C. TI-Prime is spin-coated on the surface first as an adhesion promoter at a speed of 3000 rpm with an acceleration of 1000 rpm/s for 23 s. Then the substrate is baked for 3 minutes at 100 °C. Ma-N resist is spin-coated next at 3400 rpm, 1000 rpm/s for 60 s. After the baking procedure at 90 °C for 2 minutes, the layer thickness reaches 340 nm.

Spin-coating of HSQ 6% resist: The substrate is baked on a hotplate for 3 minutes at 100 °C. HSQ is spin-coated at a speed of 3000 rpm with an acceleration of 1000 rpm/s for 60 s. Then the substrate is baked for 5 minutes at 90 °C. The layer thickness is approximately 145 nm of HSQ 6%.

Spin-coating of HSQ 15% resist: The substrate is baked on a hotplate for 3 minutes at 100 °C. HSQ is spin-coated at a speed of 6000 rpm with an acceleration of 2000 rpm/s for 60 s. Then the substrate is baked for 1 minute at 80 °C.

Electron-beam lithography (EBL): A 50 kV JEOL-5500 lithography system at the Center for Functional Nanostructures (CFN) was used for all patterning steps. The sample with resist on it is exposed to a focused beam of electrons shaped by a sophisticated lens system and cut by the final aperture to the size of tenth of µm. The final beam diameter at the sample is less than 10 nm, which allows for high-resolution patterning.

Depending on the resist and dose, the mask can be positive (used for subsequently metal evaporation) or negative (used for patterning of photonic circuits). Typical parameters for the different resists used in this thesis are collected in table A.1. For PMMA, for example, an area dose of $400\,\mu C/cm^2$, 4 nm step size, and a current of 1 nA was utilized. PEC was applied with a minimum value of $80\,\%$ of the chosen base dose. The mask for the metal electrodes was written in two steps within one run. Different currents and step sizes were used for big and small structures, thus a manual alignment procedure was required in-between to optimize the writing time, during which the sample remained in vacuum.

Development of PMMA resist: The resist is developed by immersing the sample in a solution of MIBK:IPA (1:3) for 2 minutes. Thereafter, the sample is carefully rinsed in IPA and dried with a nitrogen gun.

Development of HSQ and ma-N: The development is performed in MF-319 ($6.25\,\%$ TMAH in water-based solution) for 10 minutes in case of HSQ and ma-N, respectively. Water is used as a stopper, subsequently the sample is dried with a nitrogen gun.

Development of ZEP: This resist is developed in xylene with isopropanol to stop the developing and rinse the sample. A nitrogen gun is used for drying.

Metal deposition: Directly after the development, 5 nm Cr and $80-120$ nm Au were deposited on the chip by means of physical vapor deposition (PVD) (Fig. A.1). The PVD setup contains a loading chamber and an ultra-high vacuum main chamber. For accelerating the pumping process and keeping the clean environment in the main chamber, the load chamber is used for translating the sample into and out of the setup. Multiple samples can be installed on a holder, which is connected to a horizontal one-axis manipulator. After pumping of the loading chamber to a sufficient low pressure, shutter 1 can be opened and the sample holder is moved into the main chamber. The evaporation process occurs at a pressure of $10^{-7}-10^{-5}$ mbar. There are two crucible liners with ten crucibles containing different metals, which can be easily switched without breaking the vacuum. This allows for rapid and clean deposition of different metals. The target crucible is heated by an electron beam, emitted from a filament and deflected onto the crucible by a magnetic field. This enables fast (up to $0.3\,\text{Å/s}$) covering of many samples with high purity metals, while accurate monitoring of the layer thicknesses using a quartz crystal microbalance.

resist	purpose	area dose /$\mu C/cm^2$	current /nA	step size /nm	PEC	developer
PMMA	metal contacts	$380-420$	6 / 1	12 / 4	yes	MIBK:ISO
ZEP	waveguides	$160-180$	0.1	4	yes	xylene
ma-N		$180-200$	0.1	4	yes	MF-319
HSQ, $6\,\%$	SSPD	$1300/500$	0.1	4	no	MF-319
HSQ, $15\,\%$	cover layer	$475-525$	0.5	4	no	MF-319

Table A.1: EBL parameters for utilized patterning procedures.
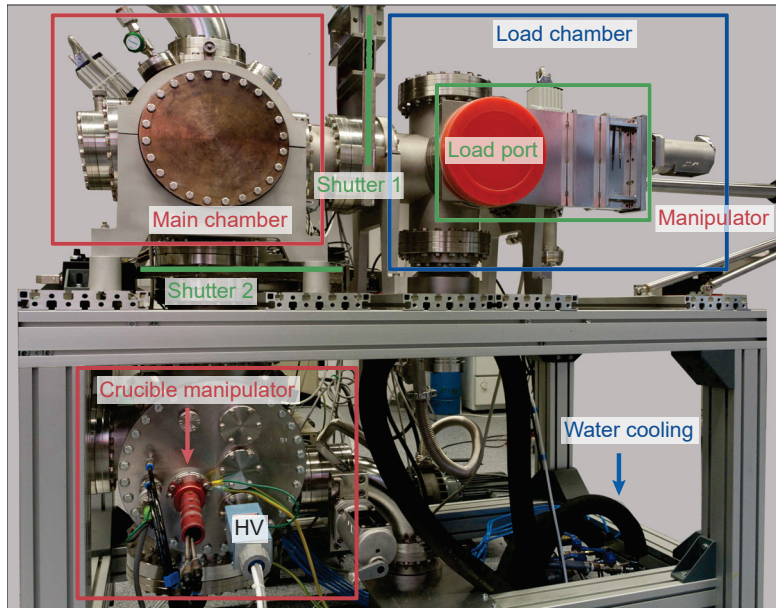
Figure A.1: Physical vapor deposition (PVD) setup.

Lift-off: Immediately after the metal deposition, the sample is soaked in acetone in a closed beaker for more than 30 minutes. A syringe filled with acetone is used to remove the excess metal. For samples with a minimal feature size of several µm, weak sonication at low power is also applied for several minutes, without any detectable damage to the structures.

RIE: Reactive ion etching is used for removing the adhesion layer of SiO_2, but also for transferring the designed pattern from the resist mask into the NbN and Si_3N_4 layers. 25 sccm of Ar was used at 200 W power and a pressure of 5 mTorr for 90 s to etch the SiO_2. 30 sccm of CF_4 at 100 W power and 1.3 Pa pressure was utilized for etching theNbN for approximately 32 s. If the adhesion layer was not removed in the previous step, the etching time is increased to 42 s. Si_3N_4 was etched in a mixture of 50 sccm CHF_3 and 2 sccm of oxygen at 175 W power and 55 mTorr chamber pressure with an etch rate of 1.1 nm/s. To achieve homogeneous etching, a SiO_2 carrier wafer was used. Before and after all RIE processes the chamber was carefully cleaned by means of etching in oxygen plasma with or without the adding of SF_6. Next the RIE is used to remove the resist residuals in 20 sccm oxygen plasma, at 70 W RF power and 50 mTorr chamber pressure for 5 minutes.

Laser cutting: If many samples were written onto one chip, the latter can be cut precisely by means of laser cutting (alternatively with a wafer saw). To protect the sample, a cover resist (S1805) is spin-coated at 4500 rpm for 60 s.

CNT suspension: In order to prepare SWCNT suspensions with chosen chirality, as-synthesized suspensions were sorted as described in the following. 10 mg of raw single-walled carbon

nanotube material from NanoIntegris was suspended in 15 ml of H_2O with 1 wt % sodium dodecyl sulfate (SDS) using a tip sonicator (Bandelin, 200 W maximum power, 20 kHz, in pulsed mode with 100 ms pulses) applied for 2 h at ~20 % power. The resulting dispersion was then centrifuged at 100,000 g for 1.5 h and carefully decanted from the pellet that was formed during centrifugation. The centrifuged SWNT material was then used for gel filtration fractionation. Gel filtration was performed using a Sephacryl S-200 gel filtration medium in a glass column of 20 cm length and 2 cm diameter with a final bed height of ~14 cm. After separation of the metallic SWNTs from the semiconducting SWCNTs (stuck on the gel) the pH of the 1 wt % SDS in H_2O eluent was changed from 4 to 1 upon addition of the appropriate concentration of HCl. The pH was reduced in 12 steps with the (8,7) material collected as an early fraction. The collected fraction was then dialyzed for 24 h to readjust the pH to 7 in 1 ml Float-A-Lyzer G2 dialysis devices by using 500 ml of a 1 wt % sodium cholate solution in H_2O. *Source:*[35].

A.2 Fabrication recipes

A.2.1 Si_3N_4 waveguides with integrated NbN detectors

Metal contacts and alignment marks
1. *Chemical cleaning of the substrate.*
2. *Spin-coating of PMMA resist.*
3. *EBL of PMMA.*
4. *Development of PMMA resist.*
5. *Metal deposition with PVD.*
6. *Lift-off.*
7. *Deposition of 5 nm SiO_2 with PVD.*

NbN detectors
1. *Chemical cleaning of the substrate with ultrasonication at the lowest power.*
2. *Spin-coating of HSQ 6%.*
3. *EBL of HSQ 6%.*
4. *Development of HSQ 6%.*
5. Removing of SiO_2.
6. *RIE of NbN.*

Waveguides
1. *Chemical cleaning of the chip with rinsing in acetone instead of ultrasonication.*
2. *Spin-coating of ma-N 2403.*
3. *EBL of ma-N.*
4. *Development of ma-N.*
5. *RIE of Si_3N_4.*
6. *Removing the ma-N residual in RIE.*

Glass cover layer for SSPD

1. *Chemical cleaning of the chip by rinsing in acetone instead of ultrasonication.*

2. *Spin-coating of HSQ 15%.*

3. *EBL of HSQ 15%.*

4. *Development of HSQ 15%.*

A.3 Measurement setups

A.3.1 Fiber-coupled vacuum setup

Source: adapted from the method section of [35]. The fiber-coupled setup, shown in Fig. A.2 (left), was used for characterization of the device transmission before and after the deposition of SWNTs, as well as for TCSPC measurements. The supercontinuum light from a white light source (Leukos-SM-30-UV) is coupled into an optical fiber array (2). This array consists of eight fibers with a core size of $8\,\mu m$. The distance between two adjacent fibers is $250\,\mu m$. All our photonic devices were designed according to this distance. The end faces of the fibers and the surrounding glass cover which they are attached to are polished at an angle of $8°$ to reduce back reflections (like in angle polished fiber connectors). The incident light from the input fiber is coupled into the chip plane through Bragg diffraction on a grating coupler. After propagation through the device it is coupled out on a second coupler and measured with a spectrometer (JAZ, Ocean Optics). The spectral range is $340 - 1014\,nm$ with a spectral resolution of $1.3\,nm$ and sensibility of $41\,photons/count$ at a wavelength of $600\,nm$. The integration time of the spectrometer varies in the range of $1\,ms - 1\,min$. To reduce the coupling losses, the fiber array has to be in close proximity to the sample surface. Therefore,
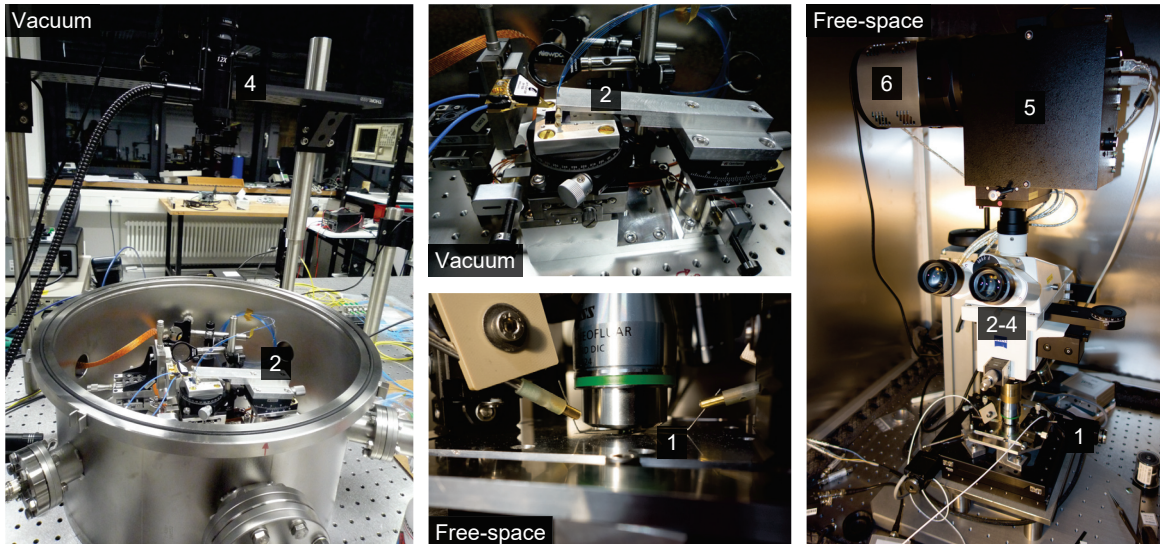
Figure A.2: Optical pictures of a vacuum fiber-coupling and free-space measurement setups. The numbers are in accordance to Fig. 4.1.

it was mounted on a piezo-stage (Picomotor, New Focus), which was controlled very precisely by a PC using LabVIEW. For coarse alignment of the sample to the fiber array, a microscope (4) with sufficient magnification and focal length was used. An image was acquired with a CCD camera and transmitted to a computer. For fine alignment, a transmitted signal, acquired with a spectrometer, was optimized. In an optical fiber line standard FC-FCA connectors were used. The losses on each connection are typically $0.3\,$dB, which can be neglected since an alignment error of the piezo actuators of $1\,\mu$m or rotation misalignment of $2°$ corresponds to coupling losses of ca. $0.5\,$dB. Additionally, these misalignments shift the Gauss shaped transmission spectrum by ca. $10\,$nm.

Coupling and guiding losses
The coupling losses can be characterized as $\mathcal{L}(\frac{\mathrm{dB}}{\mathrm{cm}}) = 10\log($total power in optical beam prior to coupling / power coupled into (out of) the m-th order coupler). Generally, the coupling losses for input and output are unknown. They are ideally taken as equal. There are three main loss mechanisms: scattering, absorption and radiation. The first one can be distinguished into volume and surface scattering. Volume scattering depends on the number of impurities (crystalline defects) inside the waveguide and on the size of these impurities compared to the wavelength of the propagated light. Surface scattering originates from the interaction between the propagated mode and the surface. In terms of geometrical optic, propagation losses are proportional to the number of reflections on the surface with lower refractive index $N_r = \frac{L}{2h\cdot\coth\theta_{inc}}$. This number is greater for higher-order modes. Surface scattering is the dominant loss mechanism for dielectrics and glasses. It is in the range of $0.5 - 5\,\frac{\mathrm{dB}}{\mathrm{cm}}$, which corresponds to $0.1\,\mu$m roughness. Optical energy can be lost by radiation into the surrounding media. It generally happens in curved waveguides. Radiation losses are exponentially proportional to the curve radius of the waveguide, which is $40\,\mu$m in all of our devices, and is in the order of $0.1\,\frac{\mathrm{dB}}{\mathrm{cm}}$ which can be neglected compared to scattering and absorption losses. If no contaminative atoms are present, absorption losses in an amorphous thin film and crystalline ferroelectric materials are negligibly small. *Source:* [87].

A.3.2 Free-space setup

A free-space measurement setup (Fig. A.2, right) is used for space- or spectral-resolved imaging of the electroluminescent / incandescent light emitted by electrically driven SWCNT reflected either by mirror or diffracted by grating structures. Samples were mounted underneath a microscope (Zeiss AxioTech Vario), directly attached to a spectrometer (Acton Research SpectraPro 2150i) with a CCD camera (Princeton Instruments PIXIS 256E Silicon, 1024x256 pixels, $-60\,°$C), all within a light-tight box. The spectrometer can operate in imaging mode, with a mirror to take real space images, or in the spectroscopy mode, with a diffraction grating (300 grooves/mm, $750\,$nm blaze wavelength). The samples were mounted on a motorized stage, electrically contacted with probe needles and biased with a source meter (Keithley 6430, equipped with current amplifier). Electroluminescence/incandescence images and images under external illumination were recorded with Zeiss 20x and Motic 20x objectives. Higher resolution images were recorded with Zeiss 100x and Mitutoyo 100x objectives (numerical aperture, focal distance and spatial resolution of the objectives are given in table A.2). The

Objective	M	WD (nm)	NA	Aperture angle ($2 \cdot \Theta$)	Resolution (µm)
Zeiss EC Epiplan-Neofluar 20x/0,50	20	2.2	0.5	30°	2.1
Motic Plan Apo 20x/0.42	20	20	0.42	24.84°	0.7
Zeiss LD EC Epiplan-Neofluar 100x/0,75	100	4	0.75	48.59°	0.4
Mitutoyo M Plan Apo 100x/0.70	100	6	0.7	44.43°	0.4

Table A.2: Parameters of optical microscope objectives for the free-space setup. The magnification, working distance, numerical aperture and spacial resolution are given.

dark current of the CCD detector yields about 2 counts per pixel per hour, and allows integrating the signal over extended periods. We estimate the sensitivity of the setup on the basis of the quantum efficiency and amplifier gain of the CCD, the efficiency of the grating, the geometrical constraints of the microscope optics (optical path), and by assuming an isotropic emitter, to about 100 emitted photons per count, in reflection and diffraction mode, respectively, and the bandwidth per pixel $\Delta\lambda$ is 0.5 nm. The wavelength axis was calibrated with a mercury lamp. The spectral response of the system has been measured with a calibrated tungsten halogen lamp. The spectral resolution of the setup is 1.5 nm. The spatial resolution is objective dependent.

Intensity calibration
Because the CCD-array has wavelength dependent quantum efficiency and different parts of the setup (as for example the diffraction gratings) are also wavelength sensitive, detailed intensity calibration was carried out. For this purpose a broadband source with a known continuous spectrum for the wavelength range of the typical measurement (490-1240 nm) was used (tungsten halogen lamp with a known spectral power dispersion per surface unit). The light of the calibration source was isotropically dispersed by a reflector (installed at the position of the sample), spectral resolved and recorded using optical objectives employed in an experiment. The curve in the Fig. A.3a represents the source spectral power dispersion and corresponds to the following fitting equation provided in the manual:

$$
\begin{aligned}
I_{\text{Lamp}} \;=\; & \lambda^{-5} \cdot \exp\left(41.715 - 4948.19/\lambda\right) \cdot \\
& \left(0.706309 + 716.075/\lambda - 593809/\lambda^2 + 262086/\lambda^3 - 62024/\lambda^4 + 588589/\lambda^5\right).
\end{aligned}
$$

The objective calibration functions F_{calibr} are calculated through division of the recorded spectra (of respective objectives) by I_{Lamp}. The resulting calibration functions are depicted in Fig. A.3b. The integration time of each calibration spectrum was 30 s. All spectra presented in this thesis that were recorded with the free-space setup are calibrated as follows: $I_{\text{real}} = I_{\text{meas}}/F_{\text{calibr}} \cdot \frac{30\,\text{s}}{T\,\text{s}}$, where F_{calibr} is a respective objective calibration function and T is an integration time of a measured spectrum [I_{meas}]. Nevertheless, this calibration can not be considered as an absolute correction.

Transport measurements
All samples were characterized after deposition of SWCNTs in order to measure device transport characteristics. The sample is mounted on a positioning table of Agilent System
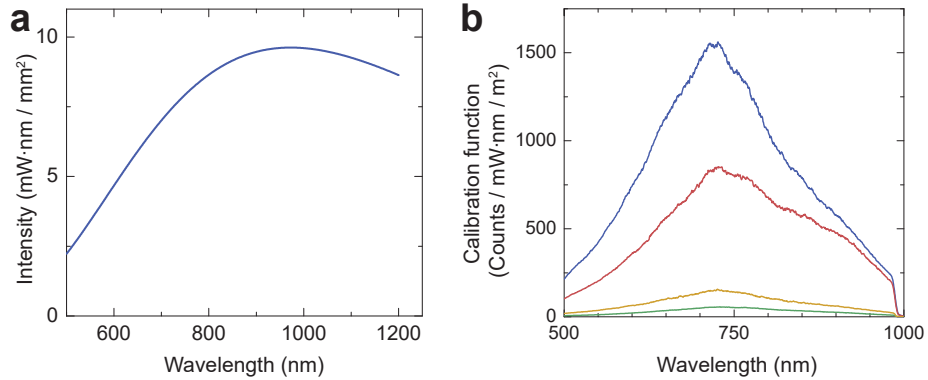
Figure A.3: (a) Spectral power dispersion on surface unit of the reference source. (b) Calibration curves for applied objectives.

(4155C semiconductor parameter analyzer). An optical microscope is used for alignment, then a device under test is connected with three probe needles. The Si bottom gate is connected through the scratch on top of the sample. The V_G is varied in a wide range from negative to positive voltages and back for defining the gate dependence and on-off ration of SWCNT-FET (Fig. A.4). The V_{SD} voltage is varied typically in a range $1 - 3\,V$. On the basis of a nanotube current and on-off ration devices with metallic and sc-SWCNTs can be obtained.

A.3.3 Cryogenic setup

The inner chamber of the cryogenic setup is shown in Fig. A.5. The sample containing SWCNT-sources and SNSPDs is mounted on a tower of piezo-stages (attocube). The RF-ports of the electrical multi-contact probe (Cascade Microtech, |Z| Probe) used to contact the source and detectors are connected to RF-feedthrough lines. The probe and fiber assembly
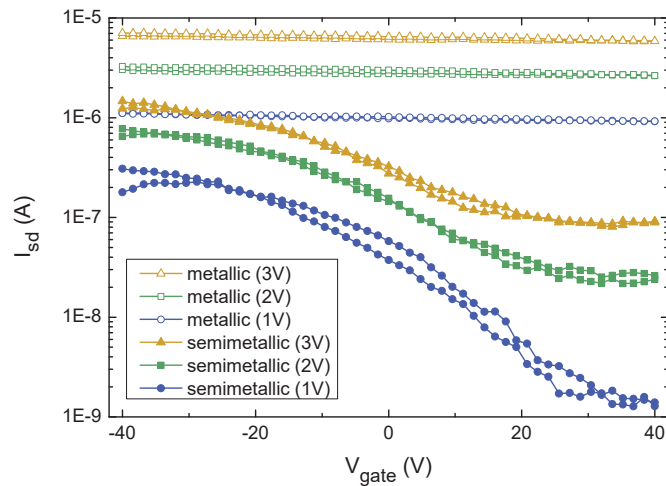
Figure A.4: Transport characteristics of metallic and semi-metallic SWNTs.
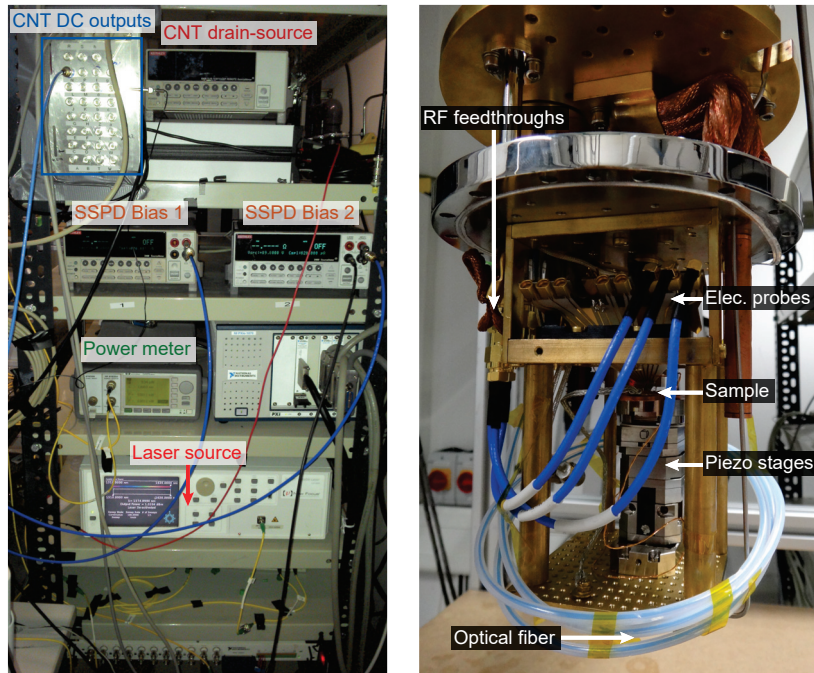
Figure A.5: Optical picture of cryogenic setup hardware (left) and inset (right).

are aligned to the sample using an optical microscope prior to installation of the piezo-tower on the inset. The relative position of each device on a chip is recorded at ambient conditions in order to align the sample in a cryostat with no optical access.

Acknowledgements

Bibliography

[1] J. L. O'Brien. Optical Quantum Computing. *Science* **318**, 1567 (2007). (quoted on page 3)

[2] A. Peruzzo, J. McClean, P. Shadbolt, M.-H. Yung, X.-Q. Zhou, P. J. Love, A. Aspuru-Guzik, and J. L. O'Brien. A variational eigenvalue solver on a photonic quantum processor. *Nat. Commun.* **5**, 4213 (2014). (quoted on page 3)

[3] Y. Wang, F. Dolde, J. Biamonte, R. Babbush, V. Bergholm, S. Yang, I. Jakobi, P. Neumann, A. Aspuru-Guzik, J. D. Whitfield, and J. Wrachtrup. Quantum Simulation of Helium Hydride Cation in a Solid-State Spin Register. *ACS Nano* **9**, 7769 (2015). (quoted on page 3)

[4] M. D. Eisaman, J. Fan, A. Migdall, and S. V. Polyakov. Invited Review Article: Single-photon sources and detectors. *Rev. Sci. Instrum.* **82**, 071101 (2011). (quoted on pages 3, 9, 10, 12, 13, 15, 16, 17, and 94)

[5] E. Knill, R. Laflamme, and G. J. Milburn. A scheme for efficient quantum computation with linear optics. *Nature* **409**, 46 (2001). (quoted on pages 3 and 9)

[6] P. J. Shadbolt, M. R. Verde, a. Peruzzo, a. Politi, a. Laing, M. Lobino, J. C. F. Matthews, and J. L. O'Brien. Generating, manipulating and measuring entanglement and mixture with a reconfigurable photonic circuit. *Nat. Photonics* **6**, 6 (2011). (quoted on page 3)

[7] M. Tillmann, B. Dakic, R. Heilmann, S. Nolte, A. Szameit, and P. Walther. Experimental boson sampling. *Nat. Photonics* **7**, 540 (2013). (quoted on page 3)

[8] A. Ahlrichs and O. Benson. Bright source of indistinguishable photons based on cavity-enhanced parametric down-conversion utilizing the cluster effect. *Appl. Phys. Lett.* **108**, 021111 (2016). (quoted on page 4)

[9] R. Kirchain and L. Kimerling. A roadmap for nanophotonics. *Nat. Photonics* **1**, 303 (2007). (quoted on page 4)

[10] W. H. P. Pernice, C. Schuck, O. Minaeva, M. Li, G. N. Goltsman, a. V. Sergienko, and H. X. Tang. High-speed and high-efficiency travelling wave single-photon detectors embedded in nanophotonic circuits. *Nat. Commun.* **3**, 1325 (2012). (quoted on page 4)

[11] A. Lohrmann, N. Iwamoto, Z. Bodrog, S. Castelletto, T. Ohshima, T. Karle, A. Gali, S. Prawer, J. McCallum, and B. Johnson. Single-photon emitting diode in silicon carbide. *Nat. Commun.* **6**, 7783 (2015). (quoted on pages 4 and 5)

[12] A. Kiraz, M. Ehrl, T. Hellerer, Ö. E. Müstecaplioglu, C. Bräuchle, and A. Zumbusch. Indistinguishable Photons from a Single Molecule. *Phys. Rev. Lett.* **94**, 223602 (2005). (quoted on pages 4 and 9)

[13] M. Steiner, A. Hartschuh, R. Korlacki, and A. J. Meixner. Highly efficient, tunable single photon source based on single molecules. *Appl. Phys. Lett.* **90**, 2005 (2007). (quoted on pages 4, 9, 15, and 16)

[14] M. Nothaft, S. Höhla, F. Jelezko, N. Frühauf, J. Pflaum, and J. Wrachtrup. Electrically driven photon antibunching from a single molecule at room temperature. *Nat. Commun.* **3**, 628 (2012). (quoted on pages 4, 5, 9, and 16)

[15] F. Jelezko and J. Wrachtrup. Single defect centres in diamond: A review. *Phys. status solidi* **203**, 3207 (2006). (quoted on pages 4, 9, and 18)

[16] J. Wrachtrup and F. Jelezko. Processing quantum information in diamond. *J. Phys. Condens. Matter* **18**, S807 (2006). (quoted on pages 4, 9, 14, and 17)

[17] C. Wang, C. Kurtsiefer, H. Weinfurter, and B. Burchard. Single photon emission from SiV centres in diamond produced by ion implantation. *J. Phys. B At. Mol. Opt. Phys.* **39**, 37 (2006). (quoted on pages 4, 9, 15, and 19)

[18] N. Mizuochi, T. Makino, H. Kato, D. Takeuchi, M. Ogura, H. Okushi, M. Nothaft, P. Neumann, A. Gali, F. Jelezko, J. Wrachtrup, and S. Yamasaki. Electrically driven single-photon source at room temperature in diamond. *Nat. Photonics* **6**, 299 (2012). (quoted on pages 4, 5, 9, and 19)

[19] C. Santori, M. Pelton, G. Solomon, Y. Dale, and Y. Yamamoto. Triggered single photons from a quantum dot. *Phys. Rev. Lett.* **86**, 1502 (2001). (quoted on pages 4, 9, and 13)

[20] V. Zwiller, P. Jonsson, H. Blom, S. Jeppesen, M.-E. Pistol, L. Samuelson, A. Katznelson, E. Kotelnikov, V. Evtikhiev, and G. Björk. Correlation spectroscopy of excitons and biexcitons on a single quantum dot. *Phys. Rev. A* **66**, 1 (2002). (quoted on pages 4 and 9)

[21] A. Schwagmann, S. Kalliakos, I. Farrer, J. P. Griffiths, G. A. C. Jones, D. A. Ritchie, and A. J. Shields. On-chip single photon emission from an integrated semiconductor quantum dot into a photonic crystal waveguide. *Appl. Phys. Lett.* **99**, 2014 (2011). (quoted on pages 4, 5, 9, and 17)

[22] A. Laucht, S. Pütz, T. Günthner, N. Hauke, R. Saive, S. Frédérick, M. Bichler, M.-C. Amann, A. W. Holleitner, M. Kaniber, and J. J. Finley. A Waveguide-Coupled On-Chip Single-Photon Source. *Phys. Rev. X* **2**, 011014 (2012). (quoted on pages 4, 5, and 9)

[23] A. Sipahigil, K. D. Jahnke, L. J. Rogers, T. Teraji, J. Isoya, A. S. Zibrov, F. Jelezko, and M. D. Lukin. Indistinguishable photons from separated silicon-vacancy centers in diamond. *Phys. Rev. Lett.* **113**, 1 (2014). (quoted on pages 5 and 15)

[24] C. Brunel, B. Lounis, P. Tamarat, and M. Orrit. Triggered Source of Single Photons based on Controlled Single Molecule Fluorescence. *Phys. Rev. Lett.* **83**, 2722 (1999). (quoted on pages 5, 13, and 16)

[25] N. Livneh, M. G. Harats, D. Istrati, H. S. Eisenberg, and R. Rapaport. Highly Directional Room-Temperature Single Photon Device. *Nano Lett.* **16**, 2527 (2016). (quoted on page 5)

[26] P. Tonndorf, R. Schmidt, R. Schneider, J. Kern, M. Buscema, G. a. Steele, A. Castellanos-Gomez, H. S. J. van der Zant, S. Michaelis de Vasconcellos, and R. Bratschitsch. Single-photon emission from localized excitons in an atomically thin semiconductor. *Optica* **2**, 347 (2015). (quoted on pages 5, 14, and 96)

[27] S. Deshpande, J. Heo, A. Das, and P. Bhattacharya. Electrically driven polarized single-photon emission from an InGaN quantum dot in a GaN nanowire. *Nat. Commun.* **4**, 1675 (2013). (quoted on pages 5 and 17)

[28] I. E. Zadeh, A. W. Elshaari, K. D. Jöns, A. Fognini, D. Dalacu, P. J. Poole, M. E. Reimer, and V. Zwiller. Deterministic Integration of Single Photon Sources in Silicon Based Photonic Circuits. *Nano Lett.* **16**, 2289 (2016). (quoted on page 6)

[29] H.-G. Park, C. J. Barrelet, Y. Wu, B. Tian, F. Qian, and C. M. Lieber. A wavelength-selective photonic-crystal waveguide coupled to a nanowire light source. *Nat. Photonics* **2**, 622 (2008). (quoted on pages 6 and 64)

[30] C. L. Salter, R. M. Stevenson, I. Farrer, C. A. Nicoll, D. A. Ritchie, and A. J. Shields. An entangled-light-emitting diode. *Nature* **465**, 594 (2010). (quoted on page 6)

[31] P. Avouris and J. Chen. Nanotube electronics and optoelectronics. *Mater. Today* **9**, 46 (2006). (quoted on pages 6 and 21)

[32] F. Xia, M. Steiner, Y.-M. Lin, and P. Avouris. A microcavity-controlled, current-driven, on-chip nanotube emitter at infrared wavelengths. *Nat. Nanotechnol.* **3**, 609 (2008). (quoted on page 6)

[33] R. Miura, S. Imamura, R. Ohta, A. Ishii, X. Liu, T. Shimada, S. Iwamoto, Y. Arakawa, and Y. K. Kato. Ultralow mode-volume photonic crystal nanobeam cavities for high-efficiency coupling to individual carbon nanotube emitters. *Nat. Commun.* **5**, 5580 (2014). (quoted on pages 6, 19, 47, and 64)

[34] T. Mori, Y. Yamauchi, S. Honda, and H. Maki. An electrically driven, ultrahigh-speed, on-chip light emitter based on carbon nanotubes. *Nano Lett.* **14**, 3277 (2014). (quoted on pages 6, 69, and 96)

[35] S. Khasminskaya, F. Pyatkov, B. S. Flavel, W. H. Pernice, and R. Krupke. Waveguide-integrated light-emitting carbon nanotubes. *Adv. Mater.* **26**, 3465 (2014). (quoted on pages 6, 29, 30, 34, 46, 47, 49, 50, 51, 52, 53, 54, 55, 56, 57, 58, 59, 61, 108, and 109)

[36] J. a. Misewich, R. Martel, P. Avouris, J. C. Tsang, S. Heinze, and J. Tersoff. Electrically induced optical emission from a carbon nanotube FET. *Science* **300**, 783 (2003). (quoted on pages 6, 19, 47, 49, and 54)

[37] P. Avouris, M. Freitag, and V. Perebeinos. Carbon-nanotube photonics and optoelectronics. *Nat. Photonics* **2**, 341 (2008). (quoted on pages 6, 19, and 28)

[38] A. Jorio, G. Dresselhaus, and M. S. Dresselhaus. Carbon Nanotubes, volume 111 of *Topics in Applied Physics*, (Springer Berlin Heidelberg2008). ISBN 978-3-540-72864-1. (quoted on pages 6, 19, 20, 21, 22, 23, 24, 25, and 26)

[39] H. Kataura, Y. Kumazawa, Y. Maniwa, I. Umezu, S. Suzuki, Y. Ohtsuka, and Y. Achiba. Optical properties of single-wall carbon nanotubes. *Synth. Met.* **103**, 2555 (1999). (quoted on pages 6, 22, and 23)

[40] S. M. Bachilo. Structure-Assigned Optical Spectra of Single-Walled Carbon Nanotubes. *Science* **298**, 2361 (2002). (quoted on pages 6, 19, 20, 23, 24, and 26)

[41] H. Liu, D. Nishide, T. Tanaka, and H. Kataura. Large-scale single-chirality separation of single-wall carbon nanotubes by simple gel chromatography. *Nat. Commun.* **2**, 309 (2011). (quoted on pages 7, 19, 40, and 41)

[42] F. Hennrich, W. Li, R. Fischer, S. Lebedkin, R. Krupke, and M. M. Kappes. Length-Sorted, Large-Diameter, Polyfluorene-Wrapped Semiconducting Single-Walled Carbon Nanotubes for High-Density, Short-Channel Transistors. *ACS Nano* **10**, 1888 (2016). (quoted on pages 7, 35, 40, and 41)

[43] A. Vijayaraghavan, S. Blatt, D. Weissenberger, M. Oron-Carl, F. Hennrich, D. Gerthsen, H. Hahn, and R. Krupke. Ultra-Large-Scale Directed Assembly of Single-Walled Carbon Nanotube Devices. *Nano Lett.* **7**, 1556 (2007). (quoted on pages 7 and 41)

[44] A. Högele, C. Galland, M. Winger, and A. Imamoglu. Photon Antibunching in the Photoluminescence Spectra of a Single Carbon Nanotube. *Phys. Rev. Lett.* **100**, 217401 (2008). (quoted on pages 7, 14, 19, 26, 28, 90, 91, 95, and 96)

[45] M. S. Hofmann, J. T. Glückert, J. Noé, C. Bourjau, R. Dehmel, and A. Högele. Bright, long-lived and coherent excitons in carbon nanotube quantum dots. *Nat. Nanotechnol.* **8**, 502 (2013). (quoted on pages 7, 15, 19, 84, 90, 91, 92, 93, 95, 96, and 100)

[46] X. Ma, N. F. Hartmann, J. K. S. Baldwin, S. K. Doorn, and H. Htoon. Room-temperature single-photon generation from solitary dopants of carbon nanotubes. *Nat. Nanotechnol.* **10**, 671 (2015). (quoted on pages 7, 12, 15, 19, 25, 26, 27, 77, 84, 90, 91, 93, and 96)

[47] T. Endo, J. Ishi-Hayase, and H. Maki. Photon antibunching in single-walled carbon nanotubes at telecommunication wavelengths and room temperature. *Appl. Phys. Lett.* **106**, 113106 (2015). (quoted on pages 7, 91, and 96)

[48] B. Lounis and M. Orrit. Single-photon sources. *Reports Prog. Phys.* **68**, 1129 (2005). (quoted on pages 9, 10, 13, 14, 15, 16, 17, 18, and 19)

[49] J. L. O'Brien, A. Furusawa, and J. Vučković. Photonic quantum technologies. *Nat. Photonics* **3**, 687 (2009). (quoted on page 9)

[50] C. J. Chunnilall, I. P. Degiovanni, S. Kück, I. Müller, A. G. Sinclair, C. J. C. Ivo, P. Degiovanni, S. Kück, I. Müller, A. G. Sinclair, C. J. Chunnilall, and I. P. Degiovanni. Metrology of single-photon sources and detectors: a review. *Opt. Eng.* **53**, 081910 (2014). (quoted on pages 9 and 10)

[51] M. Fox. Quantum optics, (Oxford University Press Inc., New York2006). ISBN 9780198566724. (quoted on pages 10, 11, 13, and 25)

[52] R. Hanbury Brown and R. Twiss. Correlation between photons in two coherent beams of light. *Nature* **177**, 27 (1956). (quoted on pages 12 and 77)

[53] H. J. Kimble, M. Dagenais, and L. Mandel. Photon Antibunching in Resonance Fluorescence. *Phys. Rev. Lett.* **39**, 691 (1977). (quoted on page 13)

[54] Z. Yuan, B. E. Kardynal, R. M. Stevenson, A. J. Shields, C. J. Lobo, K. Cooper, N. S. Beattie, D. a. Ritchie, and M. Pepper. Electrically driven single-photon source. *Science* **295**, 102 (2002). (quoted on page 13)

[55] P. Kapusta, M. Wahl, and R. Erdmann. Advanced Photon Counting, volume 15 of *Springer Series on Fluorescence*, (Springer International Publishing2015). ISBN 978-3-319-15635-4. (quoted on pages 14, 31, 68, and 81)

[56] M. W. Doherty, N. B. Manson, P. Delaney, F. Jelezko, J. Wrachtrup, and L. C. L. Hollenberg. The nitrogen-vacancy colour centre in diamond. *Phys. Rep.* **528**, 1 (2013). (quoted on pages 15, 17, and 18)

[57] S. Khasminskaya, F. Pyatkov, K. Słowik, S. Ferrari, O. Kahl, V. Kovalyuk, P. Rath, A. Vetter, F. Hennrich, M. M. Kappes, G. Gol'tsman, A. Korneev, C. Rockstuhl, R. Krupke, and W. H. Pernice. Fully integrated quantum photonic circuit with an electrically driven light source. *under Rev. Nat. Photonics* (2016). (quoted on pages 15, 38, 50, 77, 78, 79, 80, 82, 85, 88, 89, 93, 94, 95, and 97)

[58] G. D. Fuchs, G. Burkard, P. V. Klimov, and D. D. Awschalom. A quantum memory intrinsic to single nitrogen vacancy centres in diamond. *Nat. Phys.* **7**, 789 (2011). (quoted on page 17)

[59] S. Iijima. Helical microtubules of graphitic carbon. *Nature* **354**, 56 (1991). (quoted on page 19)

[60] T. W. Odom, J. H. Hafner, and C. M. Lieber. Scanning Probe Microscopy Studies of Carbon Nanotubes. In Carbon Nanotub., volume 80, pages 173–211, (Springer Berlin Heidelberg2001). (quoted on page 20)

[61] M. O'connell, S. Bachilo, and C. Huffman. Band gap fluorescence from individual single-walled carbon nanotubes. *Science* **297**, 593 (2002). (quoted on pages 19, 23, and 25)

[62] J. Lefebvre, J. Fraser, P. Finnie, and Y. Homma. Photoluminescence from an individual single-walled carbon nanotube. *Phys. Rev. B* **69**, 1 (2004). (quoted on pages 19, 24, 25, and 26)

[63] J. Lefebvre, D. G. Austing, J. Bond, and P. Finnie. Photoluminescence imaging of suspended single-walled carbon nanotubes. *Nano Lett.* **6**, 1603 (2006). (quoted on pages 19 and 26)

[64] M. Freitag, M. Steiner, A. Naumov, J. P. Small, A. A. Bol, V. Perebeinos, and P. Avouris. Carbon Nanotube Photo- and Electroluminescence in Longitudinal Electric Fields. *ACS Nano* **3**, 3744 (2009). (quoted on page 19)

[65] J. Chen, V. Perebeinos, M. Freitag, J. Tsang, Q. Fu, J. Liu, and P. Avouris. Bright Infrared Emission from Electrically Induced Excitons in Carbon Nanotubes. *Science* **310**, 1171 (2005). (quoted on pages 19 and 84)

[66] M. H. Pfeiffer, N. Stürzl, C. W. Marquardt, M. Engel, S. Dehm, F. Hennrich, M. M. Kappes, U. Lemmer, and R. Krupke. Electroluminescence from chirality-sorted (9,7)-semiconducting carbon nanotube devices. *Opt. Express* **19**, A1184 (2011). (quoted on page 19)

[67] E. Gaufrès, N. Izard, A. Noury, X. Le Roux, G. Rasigade, A. Beck, and L. Vivien. Light emission in silicon from carbon nanotubes. *ACS Nano* **6**, 3813 (2012). (quoted on page 19)

[68] M. L. Geier, J. J. Mcmorrow, W. Xu, J. Zhu, C. H. Kim, T. J. Marks, and M. C. Hersam. Solution-processed carbon nanotube thin film complementary static random access memory. *Nat. Nanotechnol.* **10**, 1 (2015). (quoted on page 19)

[69] J. W. G. Wilder, L. C. Venema, A. G. Rinzler, R. E. Smalley, and C. Dekker. Electronic structure of atomically resolved carbon nanotubes. *Nature* **391**, 59 (1998). (quoted on page 20)

[70] T. Odom, J.-L. Huang, P. Kim, and C. Lieber. Structure and Electronic Properties of Carbon Nanotubes. *J. Phys. Chem. B* **104**, 2794 (2000). (quoted on page 20)

[71] M. J. Biercuk, S. Ilani, C. M. Marcus, and P. L. Mceuen. Electrical Transport in Single-Wall Carbon Nanotubes. *Appl. Phys.* **493**, 455 (2008). (quoted on pages 21 and 43)

[72] M. S. Dresselhaus, G. Dresselhaus, and P. Avouris. Carbon Nanotubes: Synthesis, Structure, Properties, And Applications, volume 80, (Springer2000). ISBN 3540410864. (quoted on page 21)

[73] R. Saito, M. Fujita, G. Dresselhaus, and M. S. Dresselhaus. Electronic structure of chiral graphene tubules. *Appl. Phys. Lett.* **60**, 2204 (1992). (quoted on page 22)

[74] P. R. Wallace. The band theory of graphite. *Phys. Rev.* **71**, 622 (1947). (quoted on page 22)

[75] R. Saito, G. Dresselhaus, and M. S. Dresselhaus. Physical Properties of Carbon Nanotubes, (Imperial College Press1998). ISBN 1860940935. (quoted on page 23)

[76] R. B. Weisman and S. M. Bachilo. Dependence of optical transition energies on structure for single-walled carbon nanotubes in acqueous suspension: an empirical kataura plot. *Nano Lett.* **3**, 1235 (2003). (quoted on pages 23 and 24)

[77] G. G. Samsonidze, R. Saito, N. Kobayashi, A. Grüneis, J. Jiang, A. Jorio, S. G. Chou, G. Dresselhaus, and M. S. Dresselhaus. Family behavior of the optical transition energies in single-wall carbon nanotubes of smaller diameters. *Appl. Phys. Lett.* **85**, 5703 (2004). (quoted on page 24)

[78] T. Ando. Excitons in Carbon Nanotubes. *J. Phys. Soc. Japan* **66**, 1066 (1997). (quoted on pages 25 and 26)

[79] A. Hagen and T. Hertel. Quantitative analysis of optical spectra from individual single-wall carbon nanotubes. *Nano Lett.* **3**, 383 (2003). (quoted on page 25)

[80] S. Ghosh, S. M. Bachilo, R. A. Simonette, K. M. Beckingham, and R. B. Weisman. Oxygen doping modifies near-infrared band gaps in fluorescent single-walled carbon nanotubes. *Science* **330**, 1656 (2010). (quoted on page 25)

[81] F. Wang, G. Dukovic, L. E. Brus, and T. F. Heinz. The optical resonances in carbon nanotubes arise from excitons. *Science* **308**, 838 (2005). (quoted on pages 26, 27, and 96)

[82] A. Ishii, M. Yoshida, and Y. K. Kato. Exciton diffusion, end quenching, and exciton-exciton annihilation in individual air-suspended carbon nanotubes. *Phys. Rev. B* **91**, 125427 (2015). (quoted on pages 26, 84, 85, 87, and 90)

[83] D. M. Harrah and A. K. Swan. The role of length and defects on optical quantum efficiency and exciton decay dynamics in single-walled carbon nanotubes. *ACS Nano* **5**, 647 (2011). (quoted on page 27)

[84] T. Bååk. Silicon oxynitride; a material for GRIN optics. *Appl. Opt.* **21**, 1069 (1982). (quoted on page 29)

[85] D. Taillaert, F. Van Laere, M. Ayre, W. Bogaerts, D. Van Thourhout, P. Bienstman, and R. Baets. Grating Couplers for Coupling between Optical Fibers and Nanophotonic Waveguides. *Jpn. J. Appl. Phys.* **45**, 6071 (2006). (quoted on pages 29 and 34)

[86] R. Waldhäusl, B. Schnabel, P. Dannberg, E. B. Kley, a. Bräuer, and W. Karthe. Efficient coupling into polymer waveguides by gratings. *Appl. Opt.* **36**, 9383 (1997). (quoted on page 29)

[87] R. G. Hunsperger. Integrated Optics: Theory and Technology, (Springer New York2009). ISBN 978-0-387-89774-5. (quoted on pages 30, 34, 48, and 110)

[88] G. N. Gol'tsman, O. Okunev, G. Chulkova, A. Lipatov, A. Semenov, K. Smirnov, B. Voronov, A. Dzardanov, C. Williams, and R. Sobolewski. Picosecond superconducting single-photon optical detector. *Appl. Phys. Lett.* **79**, 705 (2001). (quoted on pages 31 and 81)

[89] G. Gol'tsman, K. Smirnov, P. Kouminov, B. Voronov, N. Kaurova, V. Drakinsky, J. Zhang, A. Verevkin, and R. Sobolewski. Fabrication of nanostructured superconducting single-photon detectors. *IEEE Trans. Appiled Supercond.* **13**, 192 (2003). (quoted on page 38)

[90] B. S. Flavel, M. M. Kappes, R. Krupke, and F. Hennrich. Separation of single-walled carbon nanotubes by 1-dodecanol-mediated size-exclusion chromatography. *ACS Nano* **7**, 3557 (2013). (quoted on pages 39 and 78)

[91] S. Ghosh, S. M. Bachilo, and R. B. Weisman. Advanced sorting of single-walled carbon nanotubes by nonlinear density-gradient ultracentrifugation. *Nat. Nanotechnol.* **5**, 443 (2010). (quoted on page 39)

[92] K. Moshammer, F. Hennrich, and M. M. Kappes. Selective suspension in aqueous sodium dodecyl sulfate according to electronic structure type allows simple separation of metallic from semiconducting single-walled carbon nanotubes. *Nano Res.* **2**, 599 (2009). (quoted on page 40)

[93] N. Sturzl, F. Hennrich, S. Lebedkin, and M. M. Kappes. Near monochiral single-walled carbon nanotube dispersions in organic solvents. *J. Phys. Chem. C* **113**, 14628 (2009). (quoted on page 40)

[94] A. Vijayaraghavan, F. Hennrich, N. Stürzl, M. Engel, M. Ganzhorn, M. Oron-Carl, C. W. Marquardt, S. Dehm, S. Lebedkin, M. M. Kappes, and R. Krupke. Toward single-chirality carbon nanotube device arrays. *ACS Nano* **4**, 2748 (2010). (quoted on page 41)

[95] F. Pyatkov, S. Khasminskaya, V. Kovalyuk, F. Hennrich, M. M. Kappes, W. H. P. Pernice, and R. Krupke. Sub nanosecond light pulse generation with waveguide-coupled carbon nanotube transducers. *To be Publ.* (2016). (quoted on pages 42, 67, 69, 70, 71, 72, 73, and 74)

[96] H.-W. Seo, C.-S. Han, D.-G. Choi, K.-S. Kim, and Y.-H. Lee. Controlled assembly of single SWNTs bundle using dielectrophoresis. *Microelectron. Eng.* **81**, 83 (2005). (quoted on page 41)

[97] R. Murali, Y. Yang, K. Brenner, T. Beck, and J. D. Meindl. Breakdown current density of graphene nanoribbons. *Appl. Phys. Lett.* **94**, 2007 (2009). (quoted on page 43)

[98] M. Radosavljevic, M. Freitag, K. V. Thadani, and A. T. Johnson. Nonvolatile Molecular Memory Elements Based on Ambipolar Nanotube Field Effect Transistors. *Nano Lett.* **2**, 761 (2002). (quoted on page 43)

[99] M. S. Fuhrer, B. M. Kim, T. Dürkop, and T. Brintlinger. High-Mobility Nanotube Transistor Memory. *Nano Lett.* **2**, 755 (2002). (quoted on page 43)

[100] A. Javey, J. Guo, Q. Wang, M. Lundstrom, and H. Dai. Ballistic carbon nanotube field-effect transistors. *Nature* **424**, 654 (2003). (quoted on page 43)

[101] E. Gaufrè, N. Izard, a. Noury, X. L. Roux, G. Rasigade, a. Beck, and L. Vivien. Light emission in silicon from carbon nanotubes. *ACS Nano* **6**, 3813 (2012). (quoted on page 47)

[102] S. Imamura, R. Watahiki, R. Miura, T. Shimada, and Y. K. Kato. Optical control of individual carbon nanotube light emitters by spectral double resonance in silicon microdisk resonators. *Appl. Phys. Lett.* **102** (2013). (quoted on page 47)

[103] Y. Vlasov and S. McNab. Losses in single-mode silicon-on-insulator strip waveguides and bends. *Opt. Express* **12**, 1622 (2004). (quoted on page 48)

[104] F. Jakubka, S. B. Grimm, Y. Zakharko, F. Gannott, and J. Zaumseil. Trion Electroluminescence from Semiconducting Carbon Nanotubes -Supporting. *ACS Nano* **8**, 8477 (2014). (quoted on page 49)

[105] https://www.photond.com/products/omnisim.htm (2016). (quoted on page 49)

[106] M. Fujiwara, K. Toubaru, T. Noda, H.-Q. Zhao, and S. Takeuchi. Highly efficient coupling of photons from nanoemitters into single-mode optical fibers. *Nano Lett.* **11**, 4362 (2011). (quoted on page 50)

[107] M. S. Eggleston and M. C. Wu. Efficient coupling of an antenna-enhanced nanoLED into an integrated InP waveguide. *Nano Lett.* **15**, 3329 (2015). (quoted on page 50)

[108] F. Pyatkov, V. Fütterling, S. Khasminskaya, B. S. Flavel, R. Krupke, and W. H. Pernice. Cavity enhanced light emission from electrically driven carbon nanotubes. *Nat. Photonics* (2016). (quoted on pages 51, 55, 64, 65, 66, and 69)

[109] M. Born and E. Wolf. Principles of optics: electromagnetic theory of propagation, interference and diffraction of light, (Pergamon Press, Oxford1964). ISBN 0-08-026482-4. (quoted on page 52)

[110] C. L. Mehta. Coherence-time and effective bandwidth of blackbody radiation. *Nuovo Cim.* **28**, 401 (1963). (quoted on page 53)

[111] S. J. Byrnes. Multilayer optical calculations pages 1–21 (2016). (quoted on page 53)

[112] J.-J. Greffet, R. Carminati, K. Joulain, J.-P. Mulet, S. Mainguy, and Y. Chen. Coherent emission of light by thermal sources. *Nature* **416**, 61 (2002). (quoted on page 53)

[113] J.-J. Greffet and C. Henkel. Coherent thermal radiation. *Contemp. Phys.* **48**, 183 (2007). (quoted on page 53)

[114] N. Gruhler, C. Benz, H. Jang, J.-H. Ahn, R. Danneau, and W. H. P. Pernice. High-quality Si3N4 circuits as a platform for graphene-based nanophotonic devices. *Opt. Express* **21**, 31678 (2013). (quoted on page 58)

[115] F. Horst, W. M. Green, S. Assefa, S. M. Shank, Y. a. Vlasov, and B. J. Offrein. Cascaded Mach-Zehnder wavelength filters in silicon photonics for low loss and flat pass-band WDM (de-) multiplexing. *Opt. Express* **21**, 11652 (2013). (quoted on page 59)

[116] J.-M. Liu. Photonic devices, (Cambridge University Press2009). ISBN 978-0-521-13578-8. (quoted on page 60)

[117] R. G. Fechner, F. Pyatkov, S. Khasminskaya, B. S. Flavel, R. Krupke, and W. H. P. Pernice. Directional couplers with integrated carbon nanotube incandescent light emitters. *Opt. Express* **24**, 966 (2016). (quoted on pages 62 and 63)

[118] A. Yariv. Optical electronics in modern communications, (Oxford University Press Inc., New York2007), 6 edition. ISBN 0195179463. (quoted on page 60)

[119] E. Pop, D. a. Mann, K. E. Goodson, and H. Dai. Electrical and thermal transport in metallic single-wall carbon nanotubes on insulating substrates. *J. Appl. Phys.* **101**, 1 (2007). (quoted on pages 69, 70, and 74)

[120] J. Hone, M. Whitney, C. Piskoti, and A. Zettl. Thermal conductivity of single-walled carbon nanotubes **59**, 2514 (1999). (quoted on page 70)

[121] S. P. Hepplestone, a. M. Ciavarella, C. Janke, and G. P. Srivastava. Size and temperature dependence of the specific heat capacity of carbon nanotubes. *Surf. Sci.* **600**, 3633 (2006). (quoted on page 70)

[122] http://www.scontel.ru/products/sspd (2016). (quoted on page 71)

[123] J. R. Lakowicz. Principles of Fluorescence Spectroscopy (2006). ISBN 978-0-387-31278-1 (Print) 978-0-387-46312-4 (Online). (quoted on pages 73, 90, and 96)

[124] Z. Yao, C. Kane, and C. Dekker. High-field electrical transport in single-wall carbon nanotubes. *Phys. Rev. Lett.* **84**, 2941 (2000). (quoted on page 74)

[125] C. W. Marquardt, S. Dehm, A. Vijayaraghavan, S. Blatt, F. Hennrich, and R. Krupke. Reversible metal-insulator transitions in metallic single-walled carbon nanotubes. *Nano Lett.* **8**, 2767 (2008). (quoted on page 74)

[126] D. Mann, Y. K. Kato, A. Kinkhabwala, E. Pop, J. Cao, X. Wang, L. Zhang, Q. Wang, J. Guo, and H. Dai. Electrically driven thermal light emission from individual single-walled carbon nanotubes. *Nat. Nanotechnol.* **2**, 33 (2007). (quoted on pages 74 and 87)

[127] O. Kahl, S. Ferrari, V. Kovalyuk, G. N. Goltsman, A. Korneev, and W. H. P. Pernice. Waveguide integrated superconducting single-photon detectors with high internal quantum efficiency at telecom wavelengths. *Sci. Rep.* **5**, 10941 (2015). (quoted on pages 78, 81, 82, and 83)

[128] S. Ferrari, O. Kahl, V. Kovalyuk, G. N. Goltsman, A. Korneev, and W. H. P. Pernice. Waveguide-integrated single- and multi-photon detection at telecom wavelengths using superconducting nanowires. *Appl. Phys. Lett.* **106**, 151101 (2015). (quoted on page 78)

[129] V. Kovalyuk, W. Hartmann, O. Kahl, N. Kaurova, A. Korneev, G. Goltsman, and W. H. P. Pernice. Absorption engineering of NbN nanowires deposited on silicon nitride nanophotonic circuits. *Opt. Express* **21**, 22683 (2013). (quoted on page 78)

[130] P. Rath, O. Kahl, S. Ferrari, F. Sproll, G. Lewes-Malandrakis, D. Brink, K. Ilin, M. Siegel, C. Nebel, and W. Pernice. Superconducting single-photon detectors integrated with diamond nanophotonic circuits. *Light Sci. Appl.* **4**, 1 (2015). (quoted on page 81)

[131] F. Marsili, F. Najafi, E. Dauler, F. Bellei, X. Hu, M. C. Csete, and R. Molnar. Single-photon detectors based on superconducting nanowires. *Nano Lett.* **11**, 2048 (2011). (quoted on page 82)

[132] O. Kahl, S. Ferrari, P. Rath, A. Vetter, C. Nebel, and W. H. Pernice. High efficiency, on-chip single-photon detection for diamond nanophotonic circuits. *J. Light. Technol.* **8724**, 1 (2015). (quoted on page 83)

[133] A. Srivastava and J. Kono. Diffusion-limited exciton-exciton annihilation in single-walled carbon nanotubes: A time-dependent analysis. *Phys. Rev. B - Condens. Matter Mater. Phys.* **79**, 1 (2009). (quoted on pages 84, 87, and 94)

[134] T. Mueller, M. Kinoshita, M. Steiner, V. Perebeinos, A. a. Bol, D. B. Farmer, and P. Avouris. Efficient narrow-band light emission from a single carbon nanotube p-n diode. *Nat. Nanotechnol.* **5**, 27 (2010). (quoted on page 86)

[135] S. Berger, G. Cassabois, C. Delalande, P. Roussignol, L. P. Aigrain, and X. Marie. Temperature dependence of exciton recombination in semiconducting single-wall carbon nanotubes arXiv : cond-mat / 0701137v1 8 Jan 2007 (2007). (quoted on pages 87 and 96)

[136] Y.-m. Lin, J. Appenzeller, and P. Avouris. Ambipolar-to-Unipolar Conversion of Carbon Ambipolar-to-Unipolar Conversion of Carbon Nanotube Transistors by Gate. *Nano* pages 1–4 (2004). (quoted on page 88)

[137] W. Walden-Newman, I. Sarpkaya, and S. Strauf. Quantum light signatures and nanosecond spectral diffusion from cavity-embedded carbon nanotubes. *Nano Lett.* **12**, 1934 (2012). (quoted on pages 91 and 93)

[138] I. Sarpkaya, Z. Zhang, W. Walden-Newman, X. Wang, J. Hone, C. W. Wong, and S. Strauf. Prolonged spontaneous emission and dephasing of localized excitons in air-bridged carbon nanotubes. *Nat. Commun.* **4**, 2152 (2013). (quoted on page 91)

[139] M. S. Hofmann, J. Noé, A. Kneer, J. J. Crochet, and A. Högele. Ubiquity of Exciton Localization in Cryogenic Carbon Nanotubes. *Nano Lett.* page acs.nanolett.5b04901 (2016). (quoted on page 90)

[140] S. Moritsubo, T. Murai, T. Shimada, Y. Murakami, S. Chiashi, S. Maruyama, and Y. K. Kato. Exciton diffusion in air-suspended single-walled carbon nanotubes. *Phys. Rev. Lett.* **104** (2010). (quoted on page 90)

[141] X. Ma, O. Roslyak, J. G. Duque, X. Pang, S. K. Doorn, A. Piryatinski, D. H. Dunlap, and H. Htoon. Influences of Exciton Diffusion and Exciton-Exciton Annihilation on Photon Emission Statistics of Carbon Nanotubes. *Phys. Rev. Lett.* **115**, 017401 (2015). (quoted on page 90)

[142] Y. Miyauchi, M. Iwamura, S. Mouri, T. Kawazoe, M. Ohtsu, and K. Matsuda. SI-Brightening of excitons in carbon nanotubes on dimensionality modification. *Nat. Photonics* **7**, 715 (2013). (quoted on page 94)

[143] C. D. Spataru, S. Ismail-Beigi, R. B. Capaz, and S. G. Louie. Theory and Ab initio calculation of radiative lifetime of excitons in semiconducting carbon nanotubes. *Phys. Rev. Lett.* **95**, 1 (2005). (quoted on page 96)

[144] V. Perebeinos, J. Tersoff, and P. Avouris. Radiative lifetime of excitons in carbon nanotubes. *Nano Lett.* **5**, 2495 (2005). (quoted on page 96)

[145] V. Perebeinos, J. Tersoff, and P. Avouris. Scaling of excitons in carbon nanotubes. *Phys. Rev. Lett.* **92**, 257402 (2004). (quoted on page 96)

[146] L. Claudio Andreani. Optical Transitions, Excitons, and Polaritons in Bulk and Low-Dimensional Semiconductor Structures, volume 0, chapter Optical Tr, pages 57–112, (Springer US, Boston, MA1995). ISBN 978-1-4615-1963-8. (quoted on page 96)

Erklärung der Selbstständigkeit

Ich erkläre hiermit, dass ich die vorliegende Arbeit selbständig und ohne unerlaubte Hilfsmittel angefertigt, andere als die angegebenen Quellen und Hilfsmittel nicht benutzt und die den benutzten Quellen wörtlich oder inhaltlich entnommenen Stellen als solche kenntlich gemacht habe.

Karlsruhe, den 08.06.2016